Alma Mater Studiorum – Università di Bologna

DOTTORATO DI RICERCA IN

FISICA

Ciclo 32°

Settore Concorsuale: 02/B1

Settore Scientifico Disciplinare: FIS/03

GAS-PHASE CONDENSATION OF NANOPARTICLES AND NANOCOMPOSITES FOR ENERGY APPLICATIONS

Presentata da: Nicola Patelli

Coordinatore Dottorato Prof. Silvia Arcelli

Supervisore Prof. Luca Pasquini

Esame finale anno 2020

Abstract

Nanomaterials are not simply miniaturized materials. In this world halfway between the atomic and the bulk scale, high density of interfaces and surfaces, elemental composition, unique geometries and interactions constitute a virtually infinite set of parameters that allows to tailor material properties at the nanoscale. The aim of this Thesis is to contribute to the development of strategies for the growth of nanomaterials featuring complex morphologies and tailorable structures by careful design of Gas Phases Condensation (GPC) experiment. The proposed strategies are demonstrated for the growth of nanomaterials with applications in the energy storage field.

The co-evaporation of Mg and Ti in a H enriched atmosphere is the key to grow small $\mathrm{Mg-Ti-H}$ nanoparticles (NPs), in which $\mathrm{TiH_2}$ and $\mathrm{Mg/MgH_2}$ coexist at the single NP level, despite the bulk immiscibility of Mg and Ti. The high density of $\mathrm{MgH_2/TiH_2}$ interfaces gives rise to outstanding H-absorption and desorption kinetics in the $373-423\ \mathrm{K}$ temperature range. Moreover, a theoretical model is proposed to explain the altered thermodynamics induced by interface energetics.

Thermal GPC and Pulsed Laser GPC were employed to grow $\mathrm{Fe-Co}$ alloy nanoparticles. The influence of the two techniques over the morphology of the nanoparticles is discussed and an application in the catalysis of $\mathrm{CO_2}$ reduction is presented. Finally, a novel strategy for the one-step synthesis of $\mathrm{Fe-Co}$ alloy nanoparticles supported on Ti oxide nanoparticles via Thermal GPC is presented. This new approach relies on the independent evaporation of two metallic precursors with strongly different oxidation enthalpies in an $\mathrm{O_2}$ enriched atmosphere. TEM and XRD morphological and structural characterizations clearly show that less negative enthalpy gives birth to metallic NPs, while the other to oxide NPs.

Table of Contents

Chapter 1.

General Introduction

Undoubtedly, philosophers are in the right when they tell us that nothing is great or little otherwise than by comparison.

(J. Swift, *Gulliver's Travels*)

Anno Domini 2019. Today, human activity has the power to change the world we live, not unlikely any other force of the nature. The impressively fast technological and industrial progress has in fact left indelible footprints of the human action, sometimes determining permanent changes at the planetary scale, as we daily see for climate change, pollution, intensive material extraction. These effects are even more aggravated in the poorest countries, where sometimes scarce or no regulation is applied, and open wastelands and oil bunkering are additional severe threats both to health and environment. Concerning climate change, most of the CO_2 emissions comes from the energy production based on hydrocarbons. In the *Anthropocene*[1], the future and the quality of life on our planet is, more than ever, determined by our actions and energy-lust in the present time.

Quite paradoxically, humankind has also the chance to positively intervene in this global scenario by going to the nanoscale. Nanotechnology provides us with the tools and the means to manipulate a virtually infinite set of materials, geometries and interactions to develop devices with tailorable and tunable properties, *e.g.* by applying external electric fields.

Nanomaterials are not simply “miniaturized” materials, but they are halfway between the atomic world and the bulk world. Material’s properties change significantly when system size becomes comparable to a characteristic length scale such as the mean free path of particles or excitations that carry charges, energy and momentum. Entire new branches of science came to the existence in nanoconfined systems. Plasmonics[2] is a remarkable example that exploits the change of optical properties in nanoparticles and the intense electromagnetic field generated due to coupling between light and free-electron excitations at the surface or in the core of the nanoparticles. Plasmon resonances, which can be engineered by acting on the shape and size of the nanoparticles, find applications in energy harvesting in solar cells, development of

spectroscopy technique, like the tip-enhanced Raman spectroscopy[3], and in the switching and modulation of optical transmitted signals.

The high density of interfaces and surfaces confers to nano-systems unique physical and chemical properties and promotes their chemical reactivity. The thermodynamics of nano-scaled systems is strongly altered with respect to bulk material and size-dependent effects[4,5] become more and more complicated when dealing with compound, alloys[6] and heterogeneous systems[7]. Far from putting a limit to the exploitation of nanoparticles, this fascinating behavior allows to tailor material properties at the nanoscale.

The growing interest in the nanomaterials and nanotechnology is testified by the increasing number of publications per year in the last decade (Figure 1.1), especially concerning the development of novel materials with application in the renewable energy field, that is one of the most urgent challenges for the next future.

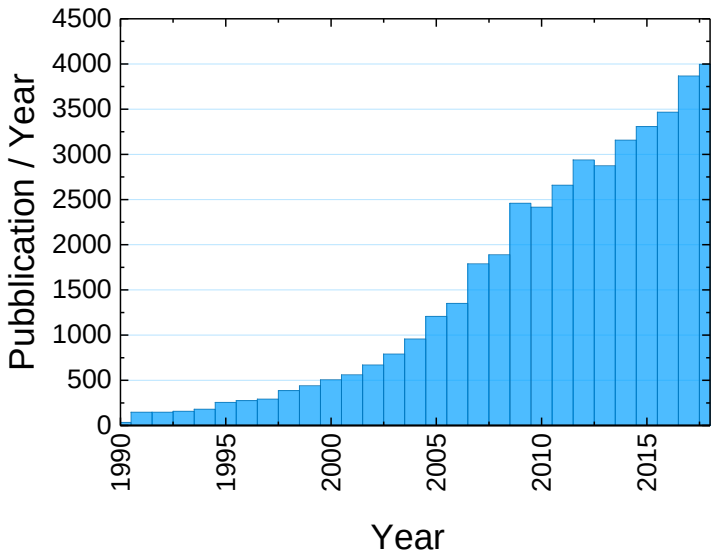

Figure 1.1. Publications per year since 1990 according to Web of Knowledge, as returned for the search keyword “Nanotechnology”.

Moving to an economy based on renewable energy sources is not straightforward, since they are intermittent and location-dependent. It is of paramount importance to identify methods to store and safely transport energy, ideally also for long times, and return it when needed. A viable energy vector candidate is hydrogen, that has the highest gravimetric energy density among the known substances ($\sim 120\ \mathrm{MJ/kg}$). Hydrogen can be produced within a clean energy system based on employing renewable energy for water splitting processes. However, the issue of the development of efficient and safe methods for hydrogen storage is yet to be addressed.

Nanomaterials can contribute to this relevant topic in multiple ways such as the hydrogen storage in metal hydrides[8–10] and complex hydrides[11,12] and the catalysis of the reduction of CO_2 to hydrocarbons using hydrogen[13].

1.1. Goal and overview of this Thesis

The goal of this Thesis is to contribute to the development of strategies for the growth of nanoparticles featuring complex morphologies and tailorable structures by careful design of Gas Phases Condensation experiments.

In Chapter 2, the principles underlying the Gas Phase Condensation technique, as well as a brief summary of some of the variations of the technique, are presented. Then a detailed description of the Thermal Gas Phase Condensation setup used to grow most of the samples in this Thesis is given.

In Chapter 3, the $Mg-Ti$ system with application in the solid-state H_2 storage is selected as a case of study. More in detail, a novel type of nanostructure is realized where MgH_2 and TiH_2 phases coexist within the same nanoparticle and over a wide compositional range, despite the bulk immiscibility of Mg and Ti. The uniqueness of this nanoscaled system resides in the high interface density that determines its performance as hydrogen storage material.

In Chapter 4, the morphology of $Fe-Co$ alloy nanoparticles grown either by Thermal or Pulsed Laser Gas Phase Condensation is discussed. As a possible field of application, the role in the catalysis of CO_2 reduction using hydrogen is selected and preliminary catalytic tests results are shown.

Finally, in Chapter 5 a novel strategy via Thermal Gas Phase Condensation for the one-step synthesis of a nanocomposite 3D material where $Fe-Co$ alloy nanoparticles are dispersed among TiO_2 nanoparticles is presented. This approach relies on the independent evaporation of two metallic precursors with strongly different oxidation enthalpies in a O_2 enriched atmosphere.

Each chapter ends with a “Major result” section, where a brief summary of the most relevant findings is presented.

Chapter 2.

Gas Phase Condensation

2.1. History of the technique

All the samples discussed in this Thesis are prepared by Gas Phase Condensation (GPC), a bottom-up physical technique for the growth of nanoparticles pioneered in the 1930s by Pfund[14], Burger and van Cittert[15], and later by Harris et al.(1948)[16] and Gleiter et al[17–19] (1988). Initially it was only possible to evaporate few metallic elements but today, due to the introduction of in-situ post processing[20], temperature-controlled heating elements[21] and alternative vapor sources (magnetron-sputtering and laser ablation based systems), it is also possible to grow compounds, alloys and oxides with more complex morphologies, such as the core-shell[22,23] and the Janus-type structures[24,25].

2.2. Theory of nucleation

In a first approximation, the nucleation process can be described by the classical homogeneous nucleation theory. When the hot precursor atoms and the surrounding inert gas (typically, He or Ar) collide, the temperature of the precursor vapor decreases exponentially fast[26] until it becomes supersaturate. In these thermodynamical conditions, the free energy change due to the nucleation of N atoms to nucleate a solid cluster is

$$\Delta G(N) = \Delta G(N)_{bulk} + \Delta G(N)_{int} = N\left(\mu_{solid} - \mu_{vapor}\right) + \eta N^{2/3}\gamma$$

where μ is the chemical potential, η is a shape factor and the γ interface free energy. The bulk contribution is negative and represents the gain in free energy when an atom passes from the supersaturated vapor to the solid phase. The second term is positive and represents the contribution of surfaces. The overall free energy $\Delta G(N)$ features a maximum at the so-called critical cluster size, indicating growing instability of the smaller pre-critical clusters. After reaching the critical cluster size, the free energy decreases and the cluster formation is thermodynamically favored. The nucleation is therefore a dynamical process requiring an energy barrier to be overcome and the meaningful parameter to describe it is the nucleation rate, which depends on the competition between the formation and evaporation of clusters.

The cluster evolution proceeds with the gradual addition and loss of atoms from the vapor phase and via collision of already formed clusters. This simple model is very intuitive and capable to predict the experimental results in many single component systems. However, it fails when dealing with multicomponent and composite materials. Much efforts have been dedicated in the last decade to improve the theory with Monte Carlo and Molecular Dynamics simulations to better understand multicomponent systems and to understand the specific role of experimental condition in determining the different complex shapes obtained from experiments. Zhao et al.[26], were able to explain the cubic or spherical shape of Fe NPs obtained by Sputtering Gas Phase Condensation technique as a combination of the condensation temperature and the rate of atomic deposition onto the growing nanocluster.

The predictive potentialities of these new computational methods coupled with the advances in experimental techniques will provide, in the next future, with all the tools to tailor properties and design functional nanomaterials with the optimal morphology and structure for targeted applications.

2.3. Variations of the technique

2.3.1. Thermal GPC

Among the variation of the Gas Phase Condensation technique, the more straightforward method is the thermal evaporation of a precursor material by joule heating refractory metal crucibles (typically W, Mo or Ta filaments or boats).This method is particularly suited for the evaporation metals elements, that features good thermal conductivity and evaporate at good rate at attainable temperatures[27]. It is also possible to evaporate alloys, when the constituent elements have similar vapor pressure and melting point[28]. Moreover, including a reactive gas, such as oxygen or nitrogen, to the atmosphere during the NPs growth stage allows to grow core-shell [29], oxide[19,30] or other compounds.

2.3.2. Sputtering GPC

An alternative method to vaporize materials is to sputter from a target precursor[19]. If compared to the standard thermal technique, sputtering has the advantage to vaporize also oxides, alloys and refractory materials avoiding the complication related with the heating of the precursor target. Furthermore, alloys with

different vapor pressures of the individual constituent elements can be grown with little compositional deviation from the precursor[31]. Typically Sputtering GPC requires pressures as high as $\sim 100\ \mathrm{Pa}$ in order for the nanoparticles to form. In this pressure regime, redeposition of sputtered atoms is more likely to occur and the yield of the process is very limited. To improve the efficiency of the process an inert gas flux can be fed the system in the proximity of the precursor target to favor the sputtered atoms migration[27]. Most noticeably, cluster deposition systems and cluster sources based on the principles of sputtering GPC technique have also been developed, additionally featuring a finely tunable cluster size selection[25,32].

2.3.3. Pulsed Laser GPC

Another alternative to sputtering and thermal sources is to interact a solid target with a focused pulsed laser beam to vaporize it and form a plasma plume. After the vaporization, the plume emitted rapidly expands colliding with the surrounding gas. The plume rapidly quenches leading to the formation of nanoparticles. This technique can generate a high-density vapor of many materials, including refractory, in a short time interval and in a well-localized volume. Pulsed Laser GPC was used to grow materials in reactive atmosphere. It was reported that high purity and stoichiometric $\gamma - \mathrm{Al_2O_3}$ nanoparticles starting from Al target in a $\mathrm{O_2}$ containin g atmosphere[33]. In the same experiment, a higher expansion rate of the plume corresponded quite intuitively to smaller average nanoparticle size. The mechanisms undergoing this technique are not yet well ascertained. A variant of this method is the pulsed laser ablation in liquid, that consists in irradiating a target while immersed in a suitable solution to obtain a colloidal suspension of nanoparticles.

2.4. Thermal GPC experimental setup

A 3D scaled model of the experimental apparatus is offered in Figure 2.1. The system is composed by two stainless steel *Thermionics* ultra high vacuum (UHV) chambers (base vacuum $2 \times 10^{-5}\ \mathrm{Pa}$) interconnected by a gate valve. Each of the chambers is provided with an independent evacuation system, constituted by a *Varian TURBO* Turbomolecular pump and an *Edwards* rotary pump. They both are equipped with a *Varian ConvecTorr p-type Pirani* gauge and a *Varian* inverted magnetron gauge as pressure sensors. A Varian ceramic capacitance diaphragm pressure sensor is selected to monitor the pressure in the nanoparticles' growth stage because of the negligible dependence of its response on gas composition and temperature.

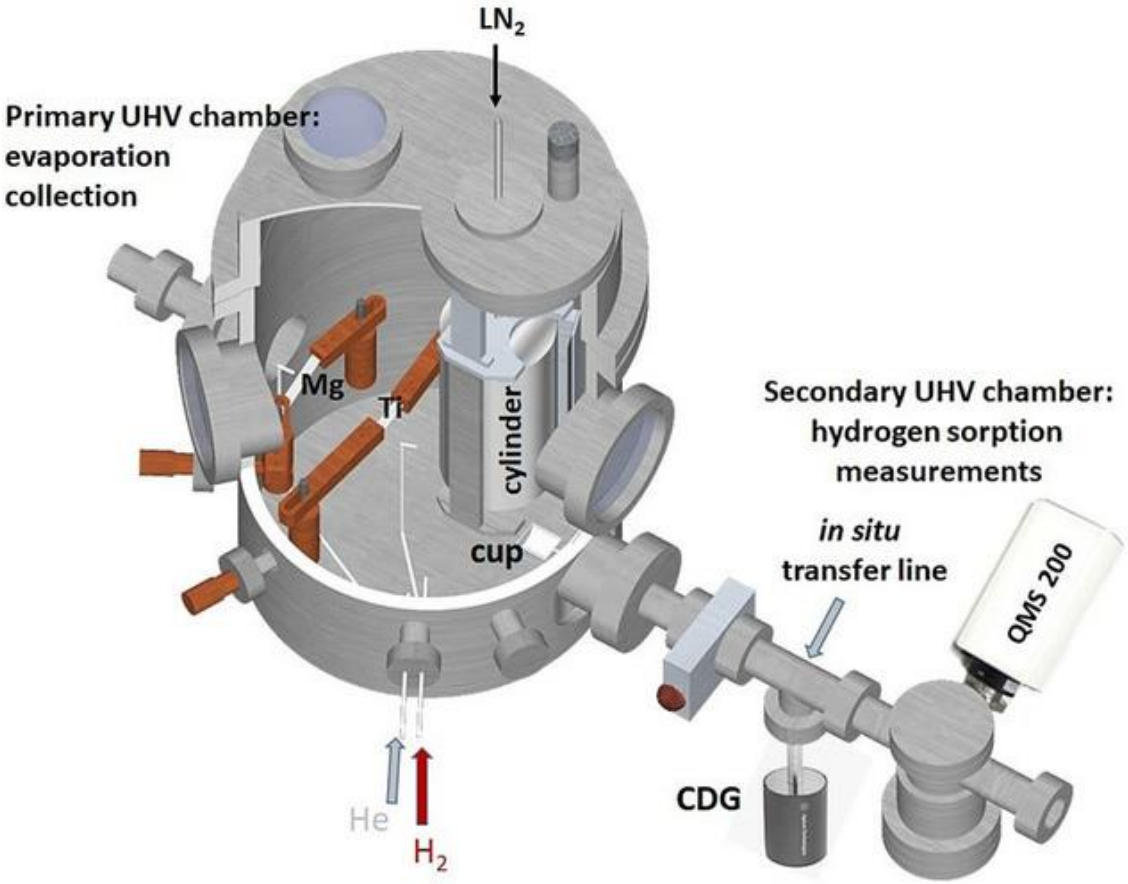

Figure 2.1. 3-D view of the experimental apparatus for the synthesis of NPs and in situ characterization of hydrogen sorption kinetics

The NPs preparation takes place in the main chamber, hereby referred as growth chamber, which has a cylindrical shape (70 cm height and 45 cm internal diameter) and a total ~110 dm^3 volume. The growth chamber hosts two pairs of copper electrodes, each one holding a Joule heated tungsten boats for the thermal evaporation of the metallic precursors. The electrodes are connected each to a high amperage *Thermionics* alternate current generator which can provide up to $I_{eff} \approx 500\ A$.

The individual evaporation rates of the metallic precursors are separately evaluated with an *Edwards Film Thickness Monitor FTM7* quartz microbalance and adjusted tuning the current flowing through each couple of electrodes, allowing also to tailor the final composition of the sample.

During the growth stage, inert He is fed into the chamber at a constant flow rate, spanning in the $4 - 120\ nml/min$ range, controlled by a *Bronkhorst* Mass Flow Controllers. A second Mass Flow Controller was installed as part of the work of this Thesis, allowing to add a reactive gas flux, either H_2 or O_2 $(0.1 - 5\ nml/min)$, during

the formation of nanoparticles. The purity of the gases is 99.9996% for He, 99.995% for $\mathrm{H_2}$ and 99.995% for $\mathrm{O_2}$. The overall $\sim 260\ \mathrm{Pa}$ pressure in the chamber is dynamically maintained for the whole process by means of the rotary pump.

The NPs aerosol is collected by a rotating cylinder internally cooled by liquid nitrogen. After the evaporation the UHV conditions are restored and the NPs are scraped off the surface of the cylinder using a blade and collected onto a stainless-steel cup before being transferred into the secondary chamber.

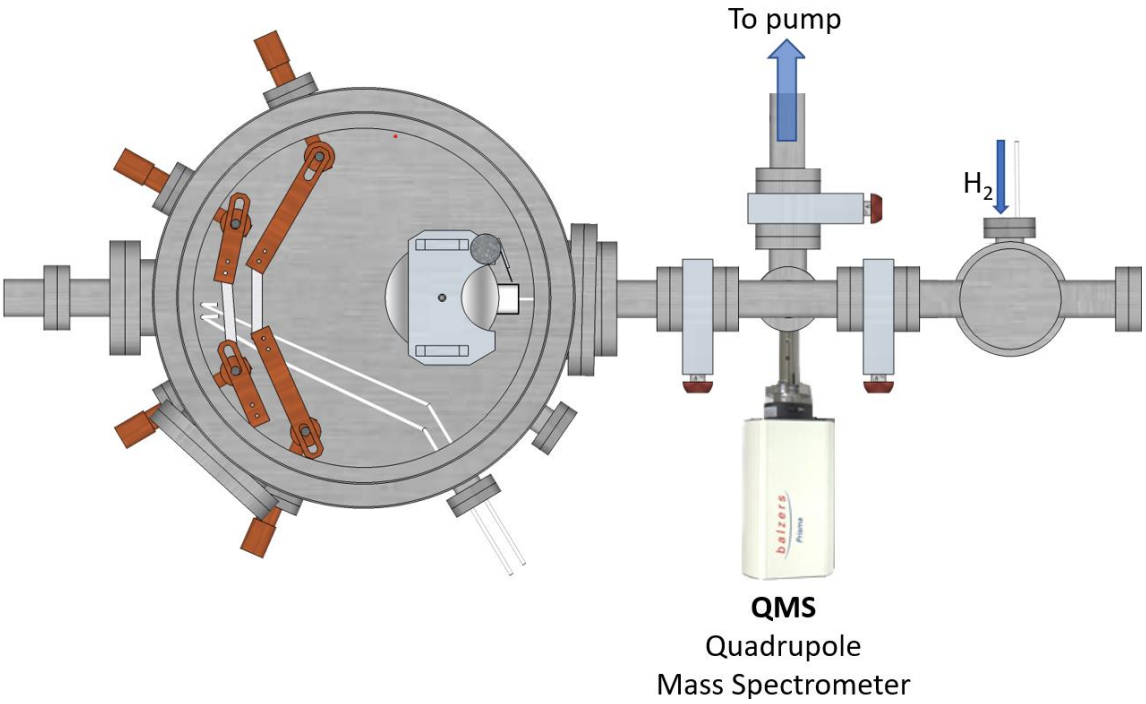

Figure 2.2. Top view: a detail of the secondary chamber.

Here, the NPs are stored inside a glass vial that can be heated by means of an external winding connected to a power supply and to a thermocouple for further thermal treatments (up to $T \sim 473\ \mathrm{K}$) in a controlled atmosphere. The secondary chamber (total volume ~5 dm^3) can also be employed as a Sievert volumetric apparatus for H-sorption characterization in the $10^0 - 10^5\ \mathrm{Pa}$ pressure range. For this purpose, during this Thesis, the chamber was also equipped with a *Preiffer* Quadrupole Mass Spectrometer (QMS) 200 for the reconstruction of isothermal H-desorption kinetics under high vacuum ($p \sim 10^{-2}\ \mathrm{Pa}$). The measurement procedure is described in Chapter 3.6.2.

Chapter 3.

Mg-Ti-H nanoparticles for H-storage

In the last century, hydrides were extensively studied because of their appealing hydrogen (H) sorption properties, which could be exploited for the realization of safe and efficient hydrogen storage systems[8,34–36]. The electronic and structure hydrogen-exchanging systems is also altered upon hydride formation, *i.e.* by changing the outer temperature or the surrounding $\mathrm{H_2}$ pressure, sometimes yielding switchable optical, electrical or thermal properties[10]. These remarkable features allowed to develop many fascinating devices such as smart windows and sensors[37], heat storage systems[38] and cryogenic coolers[39] based on hydrides, which inspired someone to refer to the present decade as the *Renaissance of hydrides* as energy materials[39]. The versatility and the performances of hydride systems depends on the thermodynamics and kinetics of the sorption process, which can be to some extent tuned by a carefully designed morphology, composition and structure.

In this Chapter we will explore the role of the nanostructure in tuning the hydrogen sorption properties of the Mg hydride system. The state of the art of hydrogen storage in Mg is presented, together with a description of the thermodynamics and kinetics of hydrides. A review of relevant strategies to improve $\mathrm{H_2}$ sorption properties is given. Following this introductory section, the synthesis of a novel concept of Mg based nanoparticle system is presented, and the thermodynamics and kinetics are critically evaluated in relation to the morphology and the nanostructure. In conclusion, the experimental results are discussed in relation to a simple thermodynamical model.

3.1. The Mg-H system

The discovery of magnesium hydride dates to XIX century, but a method for the synthesis[40] was not reported before 1951. Since then, and more intensively in the last two decades, this material was one of the most intensively studied hydride systems.

Mg, which has a hexagonal close-packed structure (HCP, S.G. $P6_3/mmc$), is a lightweight metal abundant in nature, lightweight, non-toxic and cheap. Upon the metal to hydride transition, Mg forms a stochiometric $\mathrm{MgH_2}$ hydride that exists in several crystalline structures[41,42] and its volume expands expands[43] by $\sim 30\%$. The $\alpha - \mathrm{MgH_2}$

polymorph is stable under standard condition and has a tetragonal rutile-like structure (S.G. $P4_2/mnm$). The orthorhombic $\gamma - \mathrm{MgH_2}$ phase (S.G. $Pbcn$) forms at higher pressures[42,44] and is metastable at ambient conditions. Noticeably, the coexistence of the $\alpha -$ and $\gamma - \mathrm{MgH_2}$ has been observed in samples produced via ball-milling in $\mathrm{H_2}$ atmosphere[45,46] and thermal gas phase condensation[47]. Under several GPa compression, $\beta - \mathrm{MgH_2}$ cubic phase (S.G. $Pa\bar{3}$) forms, as observed in high-pressure synchrotron experiments[48], but the required pressure range is not investigated in this Thesis. The crystallographic parameters for Mg and $\mathrm{MgH_2}$ are reported for reference in Table 3.1

Upon the metal to hydride phase transition, the volume of the Mg hexagonal close-packed (HCP, S.G. $P6_3/mmc$) structure expands[43] by $\sim 30\%$.

Table 3.1. Crystallographic parameters for the $\mathrm{Mg - H}$ system. References are reported in the bracket in the phase name column.

Phase	Space Group	Cell parameters(Å)
Mg ([49])	$P6_3/mmc$	$a = 3.2094$
		$c = 5.2108$
$\alpha - \mathrm{MgH_2}$ ([50])	$P4_2/mnm$	$a = 3.5180$
		$c = 3.0211$
$\gamma - \mathrm{MgH_2}$ ([42])	$Pbcn$	$a = 4.5051$
		$c = 5.4197$
		$a = 4.9168$

The H-sorption properties of Mg nanoparticles have been widely studied in the last decades [29,51–54]. In its metal hydride form, Mg shows moderately high gravimetric ($\rho_m = 7.6\ \mathrm{wt.\%H_2}$) and volumetric ($\rho_m = 109\ \mathrm{kg\,H_2/m^3}$) hydrogen densities. The hydride formation proceeds according to

$$\mathrm{Mg + H_2} \quad \leftrightarrow \quad \mathrm{MgH_2} \tag{3.1}$$

that is an exothermic reaction with associated enthalpy $\Delta H^0_{\mathrm{MgH_2}} \approx -74\ \mathrm{kJ/mol\ H_2}$ and entropy $\Delta S^0_{\mathrm{MgH_2}} \approx -133\ \mathrm{J/K \cdot mol\ H_2}$. The too negative formation enthalpy reflects the high stability of $\mathrm{MgH_2}$ which usually requires temperatures higher than $553\ \mathrm{K}$ in order to be dissociated at ambient pressure. This temperature is obviously too high for many practical applications, especially if compared to the $\sim 373\ \mathrm{K}$ temperature required to feed membrane fuel cells[8]. Bringing significant changes to this aspect is challenging, since the stability of the hydrides reflects the intrinsic nature of the metal-hydrogen bonds[5,10,35].

Beside the high stability, Mg hydride has also issues related with poor kinetics due to the combined effects of several factors[55,56]. Theoretical calculations performed for Mg surfaces show a low $\mathrm{H_2}$ dissociation and recombination rates[57], that are required steps for the hydrogen absorption and desorption[58,59]. Furthermore, the formation of MgO passivation layers at the surface of NPs that takes place even under clean atmosphere, aggravates the situation[23,60]. As for bulk related factors, the progressive formation of an outer $\mathrm{MgH_2}$ layer upon hydriding, coupled with the slower diffusion coefficient of H atoms through the $\mathrm{MgH_2}$ phase ($D = 10^{-20}\,\mathrm{cm^2/s}$) if compared to metallic Mg ($D = 10^{-7}\,\mathrm{cm^2/s}$), strongly slows down, or blocks, the kinetics[61].

The affordability and the potentiality of $\mathrm{MgH_2}$ as a hydrogen storage material crucially relies on the possibility to change its H-sorption properties. It is important to notice that the thermodynamics and kinetics do not exhibit a straightforward relation. For instance, $\mathrm{TiH_2}$ is an even more stable hydride ($\Delta H^0_{\mathrm{TiH_2}} \approx -130\mathrm{kJ/mol\,H_2}$)[62]. However, H-sorption kinetics are faster due to the favoured $\mathrm{H_2}$ dissociation and recombination at the surface because of the availability of s-type orbitals around the Fermi level[63] and to the rapid diffusion of atomic hydrogen in $\mathrm{TiH_2}$, (*e.g.* the characteristic time for a diffusion length of $13\,\mathrm{nm}$ is only $22\,\mathrm{s}$)[45]. Therefore, it is not obvious to obtain a novel material performing improved kinetics and thermodynamics.

3.2. Mg-H system – sorption

The thermodynamics of the hydrogen-metal system is conveniently described by the van't Hoff equation, that relates the equilibrium pressure p^{eq} for hydrogen exchange and the temperature T of the system to the molar free energy associated with the phase change ΔG^0 at standard conditions:

$$\ln\left(\frac{p^{\mathrm{eq}}}{p^0}\right) = \frac{\Delta G^0}{RT} = \frac{\Delta H^0}{RT} - \frac{\Delta S^0}{R} \tag{3.2}$$

where ΔH^0 and ΔS^0 are the enthalpy and entropy changes at standard conditions and $p^0 = 101325\,\mathrm{Pa}$ is the standard pressure.

The thermodynamics of the system at the equilibrium is more conveniently represented in terms of the Pressure-Composition-Isotherm (PCI) represented in Figure 3.1. Hydrogen forms a solid solution with the metal M up to a concentration that

we can indicate as $x_\alpha(T)$, which is temperature dependent. Above this value, the metal phase and the hydride phase, typically labeled as $\alpha-$ and $\beta-$ phases respectively, coexist until the concentration $x_\beta(T)$ is reached and the $\alpha-$phase ceases to exist.

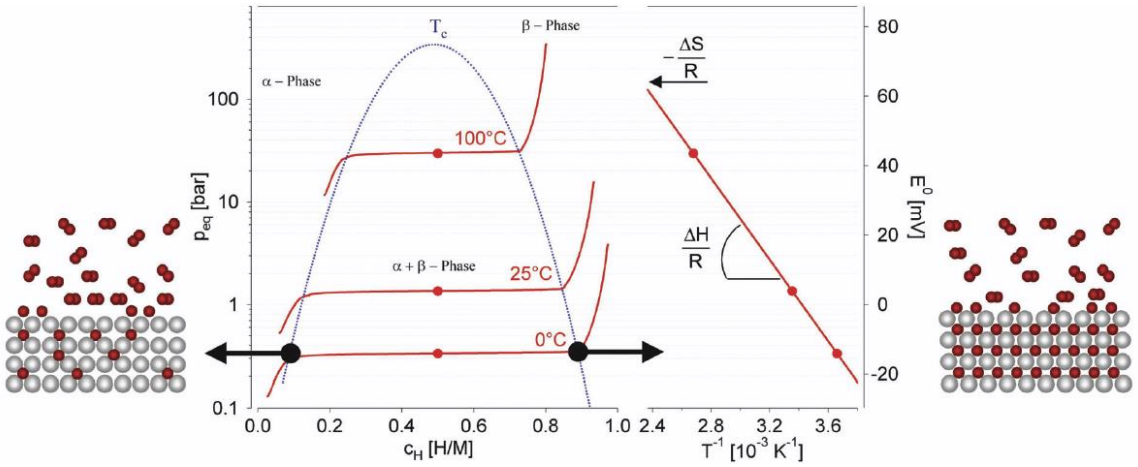

Figure 3.1. Pressure-composition-isotherm of a prototipal metal ↔ hydride transformation and the corresponding Van't Hoff plot, adapted from A. Züttel[8].

3.3. Nano-Strategies for Thermodynamic and Kinetics

A way to significantly intervene in the previously described figure to push the system to the nanoscale where the high density of interfaces and surfaces can destabilize the hydride, lowering the desorption temperature, and promote its reactivity[64]. Before considering in more detail the effect of the nanostructure, we recall some general concepts about the thermochemical equilibrium of hydride formation.

All the real systems manifest an intrinsic hysteretic behaviour that reflects into a shift in the equilibrium pressure between the absorption and desorption branches of the PCI (Figure 3.2a). Intrinsic hysteresis is due to coherency strains [65,66] and can be quantified as

$$\Delta G_{\text{its}}^{\text{hyst}} = RT \ln\left(\frac{p_{\text{abs}}}{p_{\text{des}}}\right)_{\text{bulk}} \tag{3.3}$$

In presence of hysteresis, the equilibrium pressure is typically calculated as the geometric average between the absorption and desorption plateau pressures

$$p^{\text{eq}} = (p_{\text{abs}} \cdot p_{\text{des}})^{1/2} \tag{3.4}$$

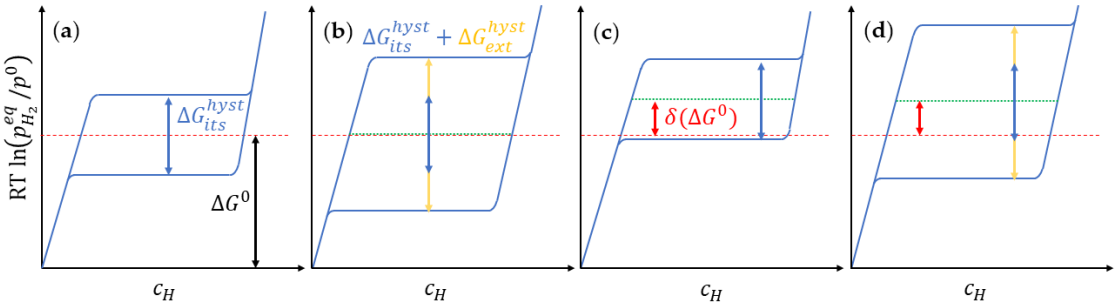

Figure 3.2. A sketch[64] to represent hysteresis and thermodynamical bias effects on hydrogen sorption isotherms. From the left to the right: (a) Reference bulk material showing an intrinsic hysteresis; (b) The effect of additional extrinsic hysteresis that increases the separation between absorption and desorption curves with no bias induction; (c) a real thermodynamical bias induced, e.g., by interface effects; (d) a more realistic case where both extrinsic hysteresis and thermodynamical bias are present.

Additional sources of strain, such as the presence of defects or interfaces in the material, can lead to a wider extrinsic hysteresis, as shown in Figure 3.2b, where the equilibrium pressure is not altered because of the symmetrical shift of both the absorption and desorption plateau. A simple relation between $\Delta G_{\text{ext}}^{\text{hyst}}$ and plateau pressure holds:

$$\Delta G_{\text{ext}}^{\text{hyst}} = RT \ln\left(\frac{p_{\text{abs}}}{p_{\text{des}}}\right) - \Delta G_{\text{its}}^{\text{hyst}} \tag{3.5}$$

A true thermodynamical bias, which corresponds to a change $\delta(\Delta G^0)$ in the free energy associated to the hydride formation, corresponds to a rigid upward shift of the PCI branches, as indicated in Figure 3.2c. According to the van't Hoff Equation (3.2) A free energy bias $\delta(\Delta G^0)$ reflects in a change of the equilibrium pressure of the system with respect to the bulk material, as in

$$\ln\left(\frac{p^{\text{eq}}}{p_{\text{bulk}}^{\text{eq}}}\right) = \frac{\delta(\Delta G^0)}{RT} \tag{3.6}$$

Many efforts have been made to design and grow nano-sized materials with more favorable hydrogen sorption thermodynamics than their bulk counterparts by inducing a thermodynamical bias in the proper direction. For instance, if the material is too stable, as it is the case for the Mg/MgH_2 system, an upward shift of the PCI branches, i.e. a positive thermodynamical bias, is desired.

3.3.1. Alloying

Perhaps, the most known method to tailor properties of materials is combining them into alloys. Ball milling was vastly employed to alloy Mg with transition metals[67–69], oxides[70] and noble metals[71–73]. The kinetics of the obtained nanomaterials proved to be drastically improved due to the to the combination of nanostructuring, alteration of Mg crystal structure and diffusion of a second element into Mg[74]. Furthermore, calculations predict that the presence of transition metals impurities could also play a role in weakening of the $\mathrm{Mg-H}$ bonds and destabilizing the hydride phase [72,75,76].

Quite recently a special class of alloys has been investigated, where the mixing of more than five principal element in almost equiatomic amount led to the formation of entropy stabilized[77,78] single structure atomic structures. This concept has also been exploited to grow $\mathrm{TiZrNbHfTa}$ high entropy alloy[79,80] capable of storing hydrogen in the interstitial sites of the resulting cubic structure. Noticeably, this material shows desorption behavior depending not only on the chemical composition but also on the microstructural parameters and, in particular, on the large lattice strain.

3.3.2. Nanoconfinement

A second possible contribution to the thermodynamics can originate when the free expansion of the material upon H −uptake is prevented because of an elastic confinement effect[29,81]. The clamping provided by the surrounding phases, which do not expand upon hydrogen absorption, results in a compressive strain that makes the hydride slightly less stable. This effect was clearly observed in Mg thin films covered with Mg-alloy-forming elements, such as Pd and Ni, showing a sorption plateau dependent on Mg thickness[81] that was interpreted in the framework of an elastic model and disentangling any alloying effect[71].

In core-shell NPs subjected to elastic constraints, the formation enthalpy of the constrained system $\Delta H^0_{\mathrm{constr}}$ was predicted to be less negative with respect to $\Delta H^0_{\mathrm{free}}$ of the corresponding free NPs[65]. In this case the free energy shift is proportional to the volume strain ϵ_V in the confined hydride NPs:

$$\delta(\Delta G^0)_{\mathrm{el}} = \delta(\Delta H^0)_{\mathrm{el}} = \Delta H^0_{\mathrm{constr}} - \Delta H^0_{\mathrm{free}} = -B\bar{V}_H\epsilon_V \tag{3.7}$$

where B is the bulk modulus and $\bar{V}_{\mathrm{H}}$ is the hydrogen partial volume. In Equation (3.7) it is assumed that the entropic contribute is unchanged between the free and constrained system, i.e. $\Delta S^0_{\mathrm{constr}} = \Delta S^0_{\mathrm{free}}$.

Elastic strain engineering has the potential to induce a significant bias up to length scales of a few tens of nanometers. The main problem is that the onset of plastic deformation strongly suppresses the effect and induces an unwanted extrinsic hysteresis, as it was observed in the case if Mg nanodots covered with a $\mathrm{TiH_2/Pd}$ bilayer[82]. It can be argued that the hysteresis could be reduced, and a true destabilization achieved if it were possible to avoid the onset of plastic deformation. However, the volume changes induced by hydrogen sorption in Mg are so high (~30%) that the resulting stresses exceed by far the yield stress of almost all involved phases[64].

3.3.3. Interface free energy – Surface area Effect

A nanostructure-dependent contribution to the thermodynamic bias can also originate due to the interface free energy[5,83,84], that scales with the volume fraction occupied by interfaces and surfaces. The effect of the interfaces is short ranged, *i.e.* it vanishes rapidly as the spatial separation between interfaces increases above a few nanometers. Interfaces can induce an upward or downward shift and on the plateau pressure depending on the sign of the free energy per unit area difference between the metal and hydride phases, according to

$$\delta(\Delta G^0)_{\mathrm{int}} = \Delta G^0_{\mathrm{nano}} - \Delta G^0_{\mathrm{bulk}} = \frac{\bar{V}_M}{V_M}\left(\sum_i A_{MH|i}\gamma_{MH|i} \; - \sum_j A_{M|j}\gamma_{M|j}\right) \tag{3.8}$$

where $\gamma^{int}_{MH|i}$ and $\gamma^{int}_{M|j}$ are the interface free energy for unit area for metal hydride and metal, respectively, while $A^{int}_{MH|i}$ and $A^{int}_{M|j}$ are the corresponding interface areas.

In the beautifully designed and fundamental experiment reported in Figure 3.3, Mooij et al.[66] recently demonstrated the possibility of achieve the destabilization of a wedge-shaped $\mathrm{MgH_2}$ enclosed between two $\mathrm{TiH_2}$ thin films. In this case, both branches shift upward with the decreasing thickness d of the $\mathrm{MgH_2}$ film. Data analysis also allows to calculate the interface free energy difference according to a simple model obtained starting from Equation (3.7). The increase in plateau pressure is not that high, about a

factor of 5 at $90\,°C$, but it clearly proves the possibility to destabilize the thermodynamics by careful interface engineering.

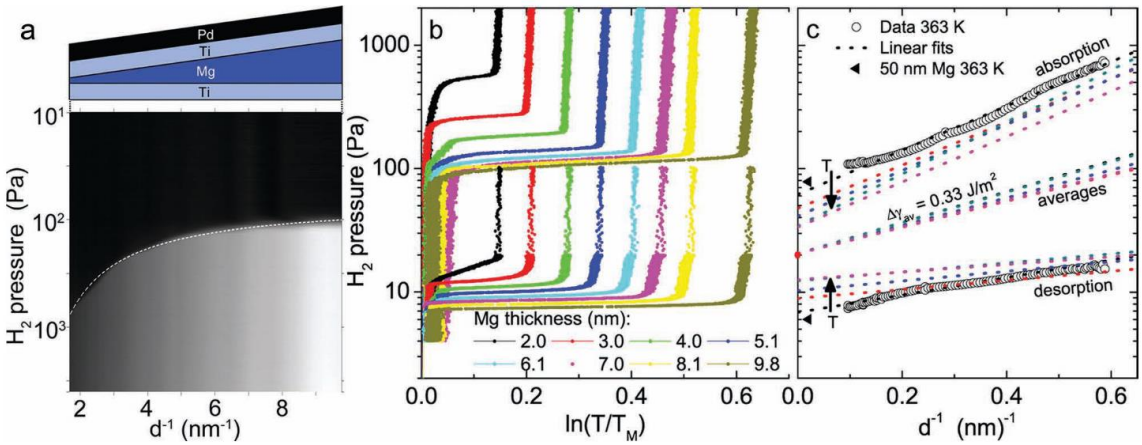

Figure 3.3. (a) A cross section a the wedge shaped Mg film sandwiched between $\mathrm{TiH_2}$ layers. The corresponding optical hydrogenography H-sorption results are shown. (b) PCIs at 363 K as a function of the Mg thickness d (c) Plateau pressures for absorption and desorption at different temperatures in the range 363–473 K. The interface free energy calculated from the slope of the gemetric averages is given. This Figure is taken from the remarkable work by Mooij et al[66].

In this Thesis, a novel strategy[85,86] that permits the growth of small $\mathrm{Mg-Ti-H}$ nanoparticles (NPs), in which $\mathrm{TiH_2}$ and $\mathrm{Mg/MgH_2}$ coexist at the single NP level, despite the bulk immiscibility of Mg and Ti, is presented. Hydride biphasic NPs were directly obtained by gas phase condensation in an equimolar $\mathrm{H_2/He}$ atmosphere. In this way, a unique nanostructure was realized featuring a high $\mathrm{MgH_2/TiH_2}$ interface area and small domain sizes, that promote outstanding kinetic properties. Most remarkably, the fast kinetics allowed to enter a previously inaccessible temperature range down to $373\,\mathrm{K}$, without the addition of expensive Pd catalysts[87]. Both the desorption and absorption thermodynamics and kinetics are investigated, and the role of the microstructure is evaluated in the following.

3.4. Experimental Setup

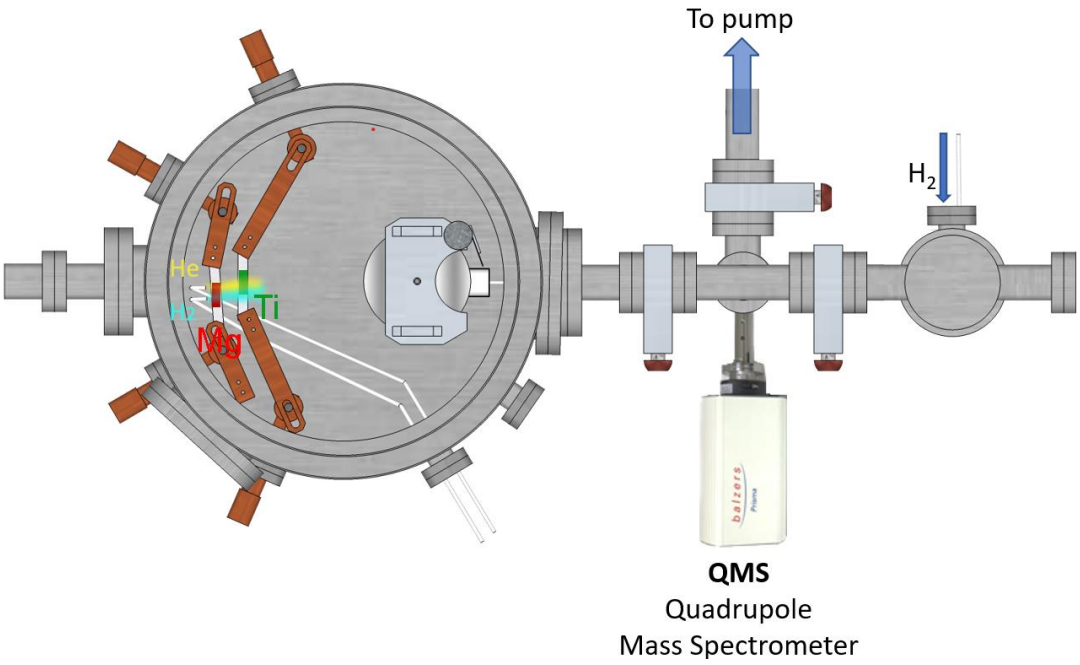

Figure 3.4. Top view of the experimental apparatus for the synthesis of NPs and in situ characterization of hydrogen sorption kinetics.The position of Mg and Ti evaporation boat is shown.

$\mathrm{Mg\text{-}Ti\text{-}H}$ NPs were grown by Reactive Gas Phase Condensation, feeding an equimolar $\mathrm{He/H_2}$ gas mixture up to a $260\ \mathrm{Pa}$ pressure. We used Mg ingots (*Alpha Aesar* 99.95% purity) and Ti powder (*Alpha Aesar* 99.9%, 150 mesh) as metal precursors. The evaporation sources were positioned few centimeters apart in order to favour the metal vapor mixing. The heating current flowing through the individual crucibles were preliminarily and individually tuned to achieve the desired $\mathrm{Mg/Ti}$ content ratio. In the following sections, the grown samples are labeled in the following accordingly with the Ti atomic% content X_{Ti} as $\mathrm{Mg} - X_{\mathrm{Ti}}\mathrm{Ti} - \mathrm{H}$.

After the synthesis stage, the NPs were transferred under high vacuum into the secondary chamber equipped with a sample heating system. For the structure and morphology characterization outside the synthesis system, the NPs were extracted from the secondary UHV chamber inside a sealed glass container under a slight Ar overpressure.

Before extraction, some of the as-prepared samples were exposed only to a single hydrogen absorption for 2 hours at $T = 400\mathrm{K}$ and $p(\mathrm{H_2}) = 13\ \mathrm{kPa}$. A second set of samples was fully characterized in the $373 - 423\ \mathrm{K}$ temperature range and exposed to several $\mathrm{H_2}$ loading/unloading cycles before extraction. In the following section, the structure and morphology analysis both of the *as-prepared* and of the *cycled* samples

is presented. The issue of thermal stability of the $\mathrm{Mg-Ti-H}$ nanoparticles is also discussed.

3.5. Structure and morphology characterization

The crystalline structure of the $\mathrm{Mg-Ti-H}$ nanoparticles has been investigated with a Bragg-Brentano *PANalytical X'celerator* diffractometer employing a $\mathrm{Cu\ K_\alpha}$ radiation ($\lambda_{K_a} = 1.54050\ \text{Å}$). The X-ray Diffraction (XRD) patterns have been analyzed using the MAUD Rietveld refinement software[88].

As prepared samples

Figure 3.5 displays the XRD patterns of four different composition samples in the as-prepared conditions.

From the Rietveld refinement results (Table 3.2), $\mathrm{MgH_2}$ is found in two phases: the rutile-type tetragonal $\alpha - \mathrm{MgH_2}$ and the orthorhombic $\gamma - \mathrm{MgH_2}$. The $\alpha - \mathrm{MgH_2}$ crystallite size $d_{\mathrm{MgH_2}}$ decreases with increasing X_{Ti} as already reported for $\mathrm{Mg-Ti}$ NPs synthesized under inert He atmosphere[89]. The lattice parameters show no relevant trend with the Ti content, and their values are within 0.1% from bulk values reported in Chapter 3.1. If Ti solubility in $\mathrm{MgH_2}$ occurred, one would expect a shrinkage of the unit cell by about 0.3% per $\mathrm{at.\%Ti}$ [90]. Figure 3.6 shows a very small volume expansion in the $0.05 - 0.2\ \%$ range, demonstrating that, if any solubility of Ti in $\alpha - \mathrm{MgH_2}$ occurs within the NPs, it is below $0.2\ \mathrm{at.\%}$ for sample $\mathrm{Mg-6Ti-H}$ and remains below 1 at.% even at the higher Ti content ($X_{\mathrm{Ti}} = 30, 60\ \mathrm{at.\%}$).

The $\alpha - \mathrm{MgH_2}$ to $\gamma - \mathrm{MgH_2}$ weight ratio slightly diminishes from ~ 5.4 to ~ 4.3 with increasing X_{Ti} from 6 to $30\ \mathrm{at.\%}$. The $\gamma - \mathrm{MgH_2}$ reflections are not observable in the XRD pattern of sample $\mathrm{Mg-60Ti-H}$, but this does not rule out its presence. In fact, the detection and the quantitative analysis of minority phases in these NPs are rather difficult and prone to large relative errors, if not impossible, because of the severe line broadening due to the small size of coherently diffracting domains.

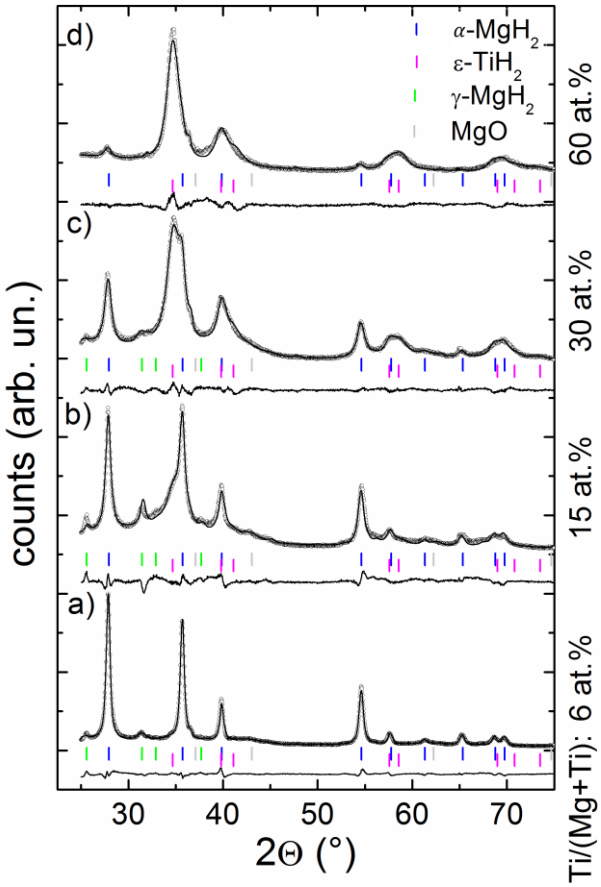

Figure 3.5. XRD patterns of as prepared NPs with different Ti content X_{Ti} . Open circles are experimental data, while the calculated Rietveld best fit is represented by the solid line. The fit residual is shown below each pattern, and the colored vertical bars mark the Bragg reflections of the main crystalline phases. For $\gamma - \mathrm{MgH_2}$, only the first four peaks are marked because the other ones are too weak. The Bragg peaks of metallic Mg, the fraction of which is always below 3 wt %, are not indicated.

The determination of the crystal structure of $\mathrm{TiH_2}$ is less straightforward. $\mathrm{TiH_2}$ is known to exhibit a transition from a fluorite cubic structure ($\delta - \mathrm{TiH_2}$, S.G. *Fm*-3*m*) to a tetragonal structure ($\varepsilon - \mathrm{TiH_2}$, S.G. *I*4/*mmm*) at about $17°\mathrm{C}$ on cooling[91]. The same transition is observed with increasing pressure above $2.2\ \mathrm{GPa}$. Upon the cubic to tetragonal phase transition, the (200), (220) and (and 311) peaks splits in two tetragonal reflections, that are not easily distinguishable in the XRD patterns in Figure 3.5 because of peak broadening. However, for the samples with the higher Ti content, it was possible to identify the fluorite $\varepsilon - \mathrm{TiH_2}$ as the dominant polimorph. Figure 3.7 displays, the better quality of the fit obtained introducing the $\varepsilon - \mathrm{TiH_2}$ phase with respect to the $\delta - \mathrm{TiH_2}$. The $\varepsilon - \mathrm{TiH_2}$ was also detected as majority $\mathrm{TiH_2}$ phase in $\mathrm{MgH_2} - \mathrm{TiH_2}$ ball-milled nanocomposites on a wide composition range[92]. In the samples $\mathrm{Mg} - 6\mathrm{Ti} - \mathrm{H}$ and $\mathrm{Mg} - 15\mathrm{Ti} - \mathrm{H}$, the low Ti content does not allow to identify unambiguously the $\mathrm{TiH_2}$ phase because the fit quality does not change significantly and the reflections at high angles are very weak.

Table 3.2. Weight fraction of the crystalline phases in as-prepared NPs as a function of X_{Ti}, determined by SEM-EDX. determined by Rietveld refinement of XRD profiles. For the phases *α*-MgH_2 and *ε*-TiH_2, the crystallite size d and lattice parameters are also reported. Rietveld agreement factors R_{wp} and R_{exp} are given. The numbers in parentheses represent the standard deviations referred to the last digit. Where (*) is reported, the parameter was fixed to ensure fit stability due to the low phase amount and/or very small crystallite size.

X_{Ti}	α-MgH_2				ε-TiH_2				MgO	γ-MgH_2	Mg	R_{wp}	R_{exp}
at.%	wt%	d_{MgH_2} (nm)	*a* (Å)	*c* (Å)	wt%	d_{TiH_2} (nm)	*a* (Å)	*c* (Å)	wt%	wt%	wt%	(%)	(%)
as-prepared NPs													
6(1)	65(5)	20(2)	4.5190(2)	3.0229(3)	16(3)	2.5(5)	3.1871(*)	4.381(*)	6(2)	12(1)	1(*)	5.1	1.3
15(2)	53(5)	18(2)	4.5200(6)	3.0224(7)	26(3)	6(1)	3.1871(*)	4.381(*)	10(1)	10(1)	1(*)	6.7	2.0
30(3)	34(3)	15(1)	4.5224(4)	3.0227(5)	49(5)	7(1)	3.1871(6)	4.381(2)	9(1)	8 (1)	2(1)	4.0	1.9
60(5)	8(1)	13(1)	4.5205(*)	3.0267(*)	86(7)	9(1)	3.196(1)	4.360(2)	3(1)	--	3(1)	5.7	2.2

The results in Table 3.2 are obtained assuming the presence of the tetragonal phase for all X_{Ti}. The TiH_2 crystallite size d_{TiH_2} decreases with increasing Mg content, reaching an extremely low value of about 2.5 nm in sample $Mg-6Ti-H$. The lattice parameters could be determined reliably only for samples $Mg-30Ti-H$ and $Mg-60Ti-H$: the relative variation of the unit cell volume with respect to ball-milled $\varepsilon-TiH_2$ powders[92] is displayed in Figure 3.6, showing a volume expansion of about 1.4 %. Using Vegard's law and literature data for MgH_2 and TiH_2 cell volumes[90,92], we can attribute this result to a Mg solubility in TiH_2 of about 5 at.%, since Mg atomic radius is larger than Ti.

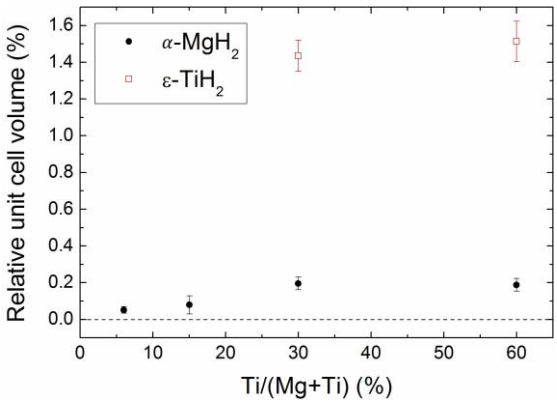

Figure 3.6. Variation of the unit cell volume in the as-prepared $Mg-Ti-H$ NPs as a function of the average Ti content. The dashed line represents no volume variation with respect to ball milled pure hydride powders[45].

The third relevant phase is MgO, which weight content never exceed 10%. This result is noticeable if compared to other reported Mg-based nanoparticles of comparable size[93]. This can be attributed to the H-rich growth atmosphere. The 130 Pa H_2 partial pressure is above the equilibrium pressure required for the hydrogenation of Mg at room temperature. The XRD patterns of the $Mg-22Ti$ sample in Figure 3.8 collected before any further thermal treatment in H_2 atmosphere clearly demonstrates

that right after the synthesis both Mg and $\mathrm{MgH_2}$ coexist within the NPs. The XRD pattern is collected in air and the low oxidation degree suggests that $\mathrm{MgH_2}$ develops mostly at the surface for the nanoparticles, forming a protective layer against oxidation. The MgO peaks are rather large, corresponding to an average $\sim 3\mathrm{nm}$ crystal size compatible with the formation of an oxide shell around NPs exposing metallic Mg [29,94]. The oxide content shows a slightly positive trend with Ti content.

The samples with lower X_{Ti} display small metallic Mg residuals, while neither Ti nor $\mathrm{TiO_2}$ is observed, corroborating the hypothesis that the hydride formation is nearly completed in the as prepared samples.

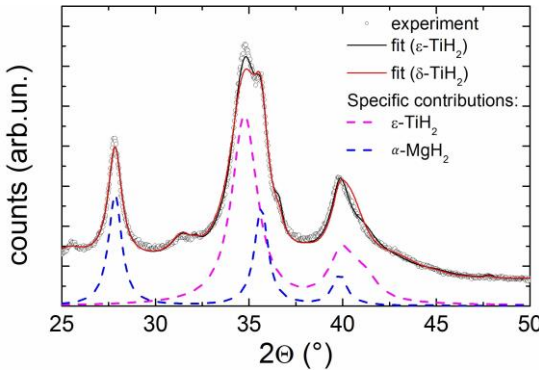

Figure 3.7. Comparison between the Rietveld fit obtained with tetragonal *ε*-TiH_2 (black solid line, R_{wp}=4.0) and cubic *δ*-TiH_2 (red solid line, R_{wp}=5.1) for the as-prepared $\mathrm{Mg-30Ti-H}$. The *ε* -TiH_2 phase accounts better for the diffracted intensity at about 34.7°, as well as for the shape of the profile around 40.5°, which stems from two *ε*-TiH_2 (110) and (002) reflections overlapped with the *α*-MgH_2 (200). The individual contributions from *ε*-TiH_2 and *α*-MgH_2 are represented by dashed lines.

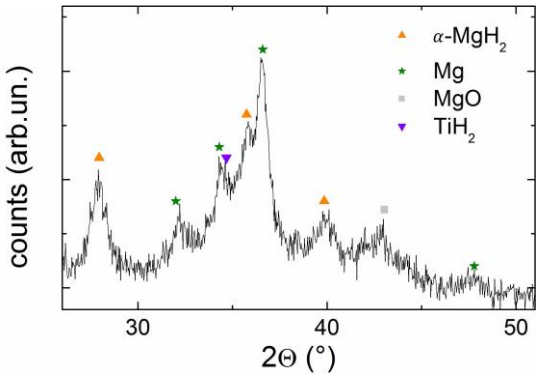

Figure 3.8. XRD pattern of $\mathrm{Mg-6Ti-H}$ NPs extracted before the in situ hydrogen absorption treatment in the secondary chamber, showing that partial MgH_2 formation takes place already as a consequence of the H_2-enriched synthesis atmosphere. The pattern is noisy because the sample quantity for this experiment was rather low.

*Cycled samples (***373-423 K** *temperature range)*

The structure of the $\mathrm{Mg-Ti-H}$ samples after several H −sorption cycles in the $373-423\ \mathrm{K}$ temperature range is reported in the XRD patterns Figure 3.9, where the separate contribution of each phase is shown. For each sample, the ending cycle was an absorption isotherm at $423\ \mathrm{K}$ and $p(\mathrm{H_2}) \approx 10\ \mathrm{kPa}$.

The main crystalline phases detected are the tetragonal $\alpha - \mathrm{MgH_2}$, $\varepsilon - \mathrm{TiH_2}$ and MgO, similarly to the as-prepared samples. The metastable $\gamma - \mathrm{MgH_2}$ phase is no longer observed after cycling, as reported also in previous experiments[93,95].

The overall picture is not significantly altered if compared with the as-prepared samples. With increasing Mg content, the Bragg reflections of $\varepsilon - \mathrm{TiH_2}$ shift toward lower angles indicating an expansion of the unit cell volume that can be attributed to the solubility of Mg in the $\mathrm{TiH_2}$ lattice. Conversely, for $\mathrm{MgH_2}$ the Bragg peaks angular positions and the derived lattice parameters are not affected by $\mathrm{X_{Ti}}$, suggesting that the solubility of Ti in $\mathrm{MgH_2}$ is below 1%. The crystallite size strongly correlates with the relative amount of the hydride phases, as clearly visible in their separate contribution to the XRD patterns. This demonstrated that each hydride acts as a refiner for the other phase inhibiting coarsening of the nanostructure both in the NPs growth stage and, more importantly, during the H-sorption.

Table 3.3. Results of the Rietveld refinement of XRD profiles of the crystalline phases in $\mathrm{Mg-Ti-H}$ samples cycled in the 373-420K temperature range. For the phases ***α***-MgH_2 and ***ε***-TiH_2, the crystallite size *d* and lattice parameters are also reported. Rietveld agreement factors R_{wp} and R_{exp} are given. The numbers in parentheses represent the standard deviations referred to the last digit. Where the (*) is reported, the parameter was fixed to ensure fit stability due to the low phase amount and/or very small crystallite size.

X_{Ti}	α-$\mathrm{MgH_2}$					ε-$\mathrm{TiH_2}$					MgO	Mg	R_{wp}	R_{exp}
at%	wt%	$d_{\mathrm{MgH_2}}$ (nm)	ε_{rms} (10^{-3})	a (Å)	c (Å)	wt%	$d_{\mathrm{TiH_2}}$ (nm)	ε_{rms} (10^{-3})	a (Å)	c (Å)	wt%	wt%	(%)	(%)
Samples cycled in the 373-423 K temperature range														
7(1)	51	40(4)	<1	4.5205 (6)	3.0224(3)	20	3.6(5)	<1	3.200(5)	4.350(*)	22	7	4.4	1.9
14(2)	60	45(4)	<1	4.5192(2)	3.0227(1)	22	3.5 (5)	5.7	3.230(3)	4.346(6)	12	6	6.6	4.1
22(2)	41	27(3)	<1	4.5240(3)	3.0241(5)	53	4.6 (5)	<1	3.214(2)	4.412(4)	6	0	6.5	5.0
35(3)	25	17(2)	<1	4.5175(8)	3.0238(8)	53	3.0 (5)	<1	3.197(2)	4.311(6)	22	0	4.5	4.4
46(2)	14	11(1)	<1	4.513(2)	3.015(4)	72	6.5 (5)	<1	3.1937(7)	4.425(2)	14	0	4.7	3.7
63(5)	4	20(*)	<1	4.522(4)	3.022(*)	74	8(1)	2.0 (7)	3.1655(6)	4.3793(15)	22	0	5.5	3.2
100	--	--	--	--	--	52	9(1)	<1	3.186(2)	4.395(5)	--	--	6.6	2.8

Mg extra peaks are detected only for the samples with lower Ti content, namely $\mathrm{Mg-7Ti-H}$ and $\mathrm{Mg-14Ti-H}$. These samples also feature markedly larger $\mathrm{MgH_2}$ crystallites ($\sim 40\ \mathrm{nm}$), pointing out to the coarsening of the nanostructure which could prevent the completion of the absorption process. Another possible cause for the deterioration of the absorption kinetics is the MgO formation due to the reaction with the residual $\mathrm{H_2O}$ vapor in the $\mathrm{H_2}$ atmosphere.

The last sample in the set was obtained by evaporating only Ti under the same experimental conditions, proving that $\mathrm{TiH_2}$ NPs can be directly synthetized via Thermal

Gas Phase Condensation. The better quality of XRD pattern fit suggest that the δ – and ε –phase are intermixed in the pure TiH_2 sample, that displays the largest ε – TiH_2 average crystal size in the set ($d_{TiH_2} \approx 9$ nm).

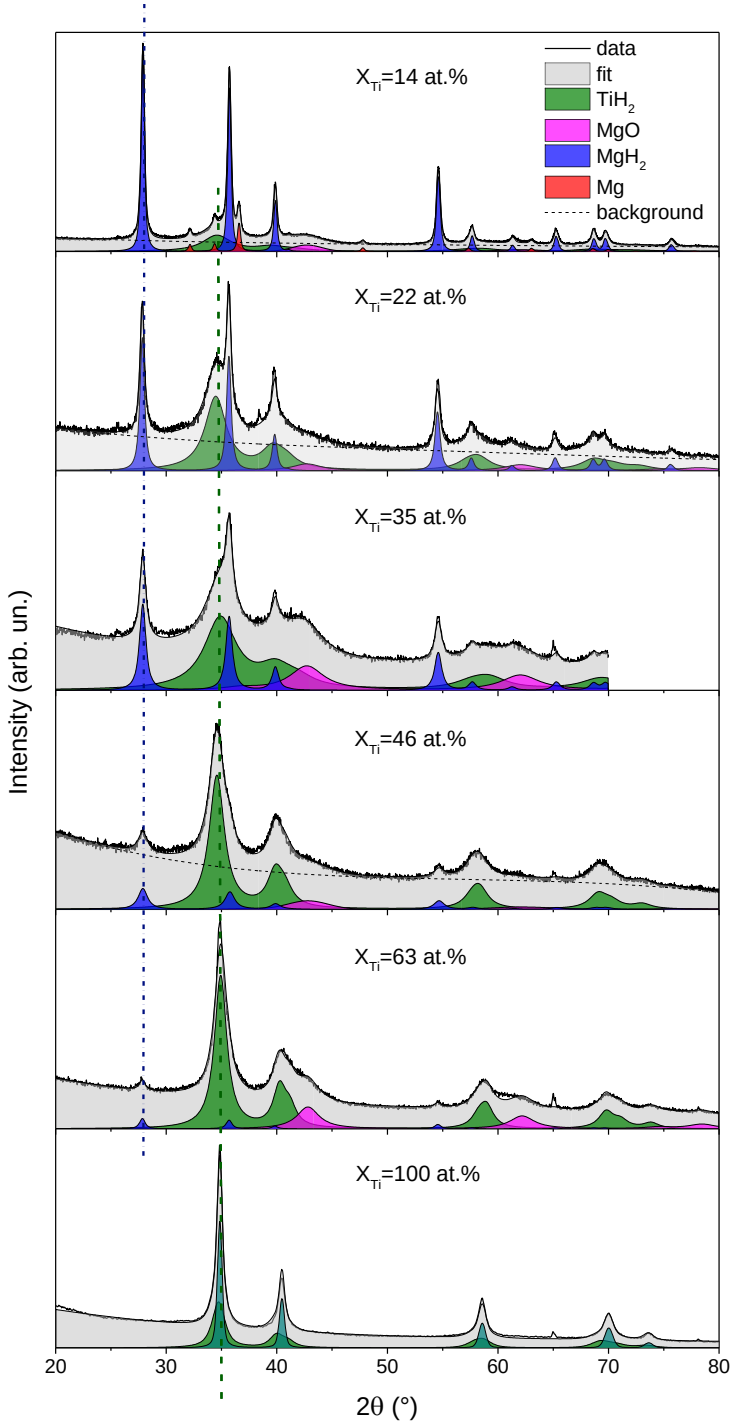

Figure 3.9. XRD patterns the $Mg - Ti - H$ samples after being cycled in the $373 - 423$ K temperature range. The Rietveld best fit is represented by the grey area and the individual phases contribution are reported. The (110) *α*-MgH_2 Bragg reflection does not shift with increasing Ti content (blue dashed line), while (111) $\varepsilon - TiH_2$ reflection shift towards higher angles (green dashed line).

TEM analysis

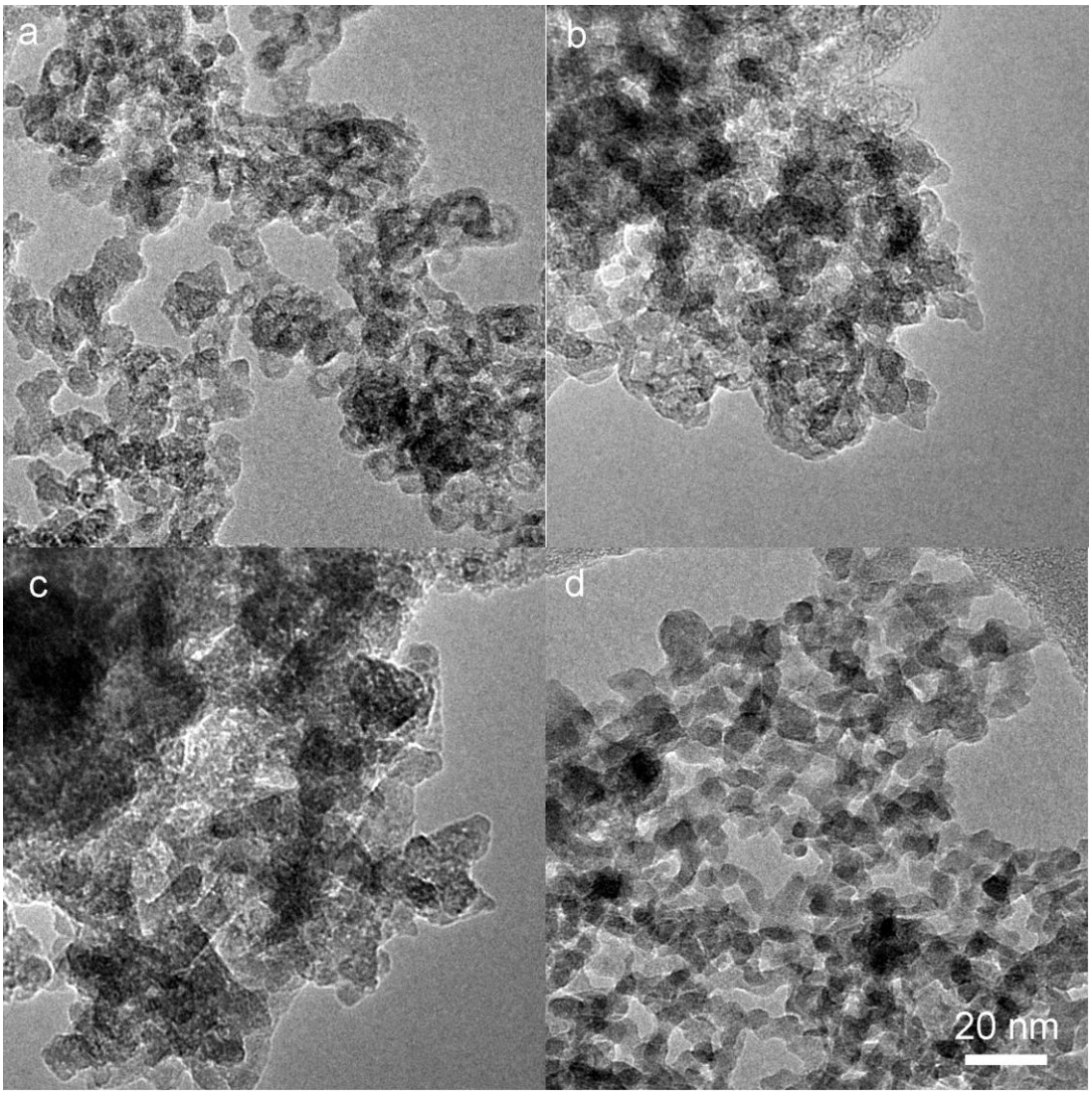

Figure 3.10. Bright-field TEM images of Mg-Ti-H NPs with increasing X_{Ti} content ratio from a) to d). a) 14 at.%; b) 22 at.%; c) 46 at.%; d) 63 at.%.

To gain insight about the morphology and elemental composition at the single NP level, we employed a *FEI Tecnai F20 ST* transmission electron microscope (TEM). The instrument was operated at 200 kV in scanning mode (STEM) coupled with an EDS detector for the profiling of the elemental distribution within the NPs with a 2 nm spatial resolution.

Figure 3.10 portraits the the bright-field TEM images of the as prepared $\mathrm{Mg} - X_{\mathrm{Ti}}\mathrm{Ti} - \mathrm{H}$ NPs samples with $X_{\mathrm{Ti}} = 14, 22, 46, 63\ \mathrm{at\%}$.. A certain degree of agglomeration is typical of the IGC synthesis technique[30], but the co-evaporation with Ti prevents the coarsening of the Mg NPs into larger ($> 100\ \mathrm{nm}$) hexagonal particles[94]. The analysis on the TEM images reveals that the proposed growth method yields nanoparticles of initial diameter d_{NP} that diminishes with the Ti content: d_{NP}~$14\ \mathrm{nm}$ for

the ($X_{\mathrm{Ti}} = 14,22\ at\%\ \mathrm{Ti}$), d_{NP}~10 nm ($X_{\mathrm{Ti}} = 45\ at\%\ \mathrm{Ti}$) and d_{NP}~7 nm ($X_{\mathrm{Ti}} = 63\ at\%\ \mathrm{Ti}$) [47,85]. The NPs exhibit significant aggregation, as commonly observed in GPC due to partial sintering in proximity of the hot vapor source[21,96].

The peculiarity of these samples is that each NP contains both Mg and Ti, the two elements being finely distributed at the nanoscale despite their mutual immiscibility in the bulk. This feature is highlighted in the High-Angle Annular Dark Field (HAADF) STEM images of Figure 3.11, which were recorded after after H-sorption cycling. The correspondent EDS elemental line profiles are reported alongside for each composition. The fluctuations of the $\mathrm{Mg/Ti}$ ratio along the scans sometimes exceed the statistical uncertainty, indicating that the two elements do not form a homogeneous solid solution and that segregation into Mg-rich and Ti-rich domains takes place. This view is consistent with the picture provided by XRD, as discussed before.

In samples $\mathrm{Mg-14Ti-H}$, the average NPs diameter observed by TEM after cycling is $d_{NP} \approx 40$ nm. This value is consistent with the $\mathrm{MgH_2}$ crystallite size given by XRD and the observation that the NPs are mostly single-crystalline. For the other samples with higher Ti contents, we did not detect a significant evolution of the NPs size upon cycling.

The contrast in the incoherent HAADF images is proportional to $tZ^{1.7}$, where t is the thickness of the specimen and Z represents the atomic number. Therefore, contrast changes in the nm scale, for which the thickness of the specimen can be considered the same, can possibly be ascribed to the presence of distributed Ti-rich phase within the NPs, i.e., to $\mathrm{TiH_2}$ based on XRD analysis. A better view of the granularity due to local changes in contrast is given in the STEM images Figure 3.12c,d for $\mathrm{Mg-6Ti-H}$ and $\mathrm{Mg-30Ti-H}$ as prepared samples.

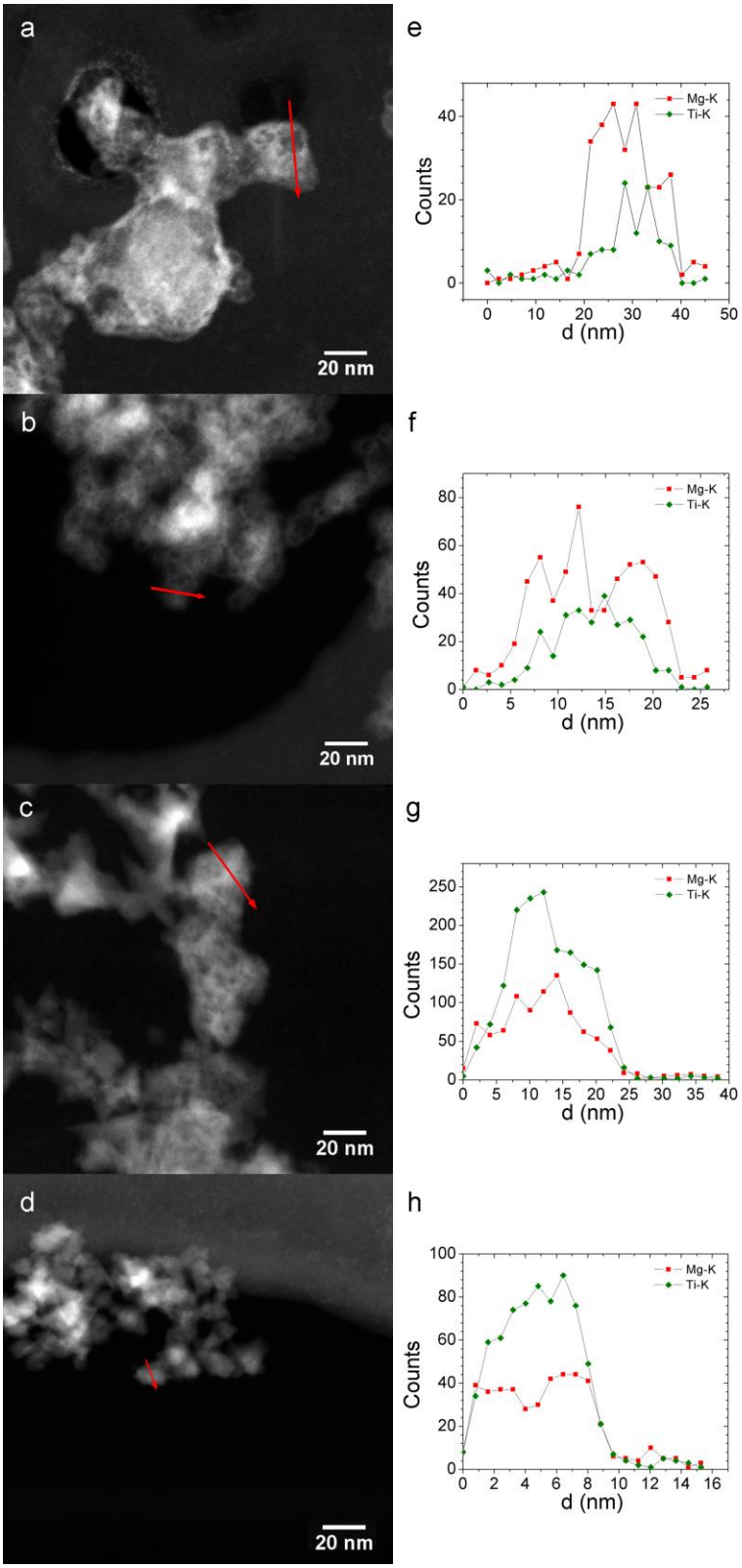

Figure 3.11. HAADF-STEM images (a-d) the corresponding STEM-EDS elemental Mg and Ti line profiles (e-h) recorded for samples with different X_{Ti} content ratio: 14 at.% Ti (a,e); 22 at.% Ti (b,f); 46 at.% Ti (c,g); 63 at.% Ti (d,h).

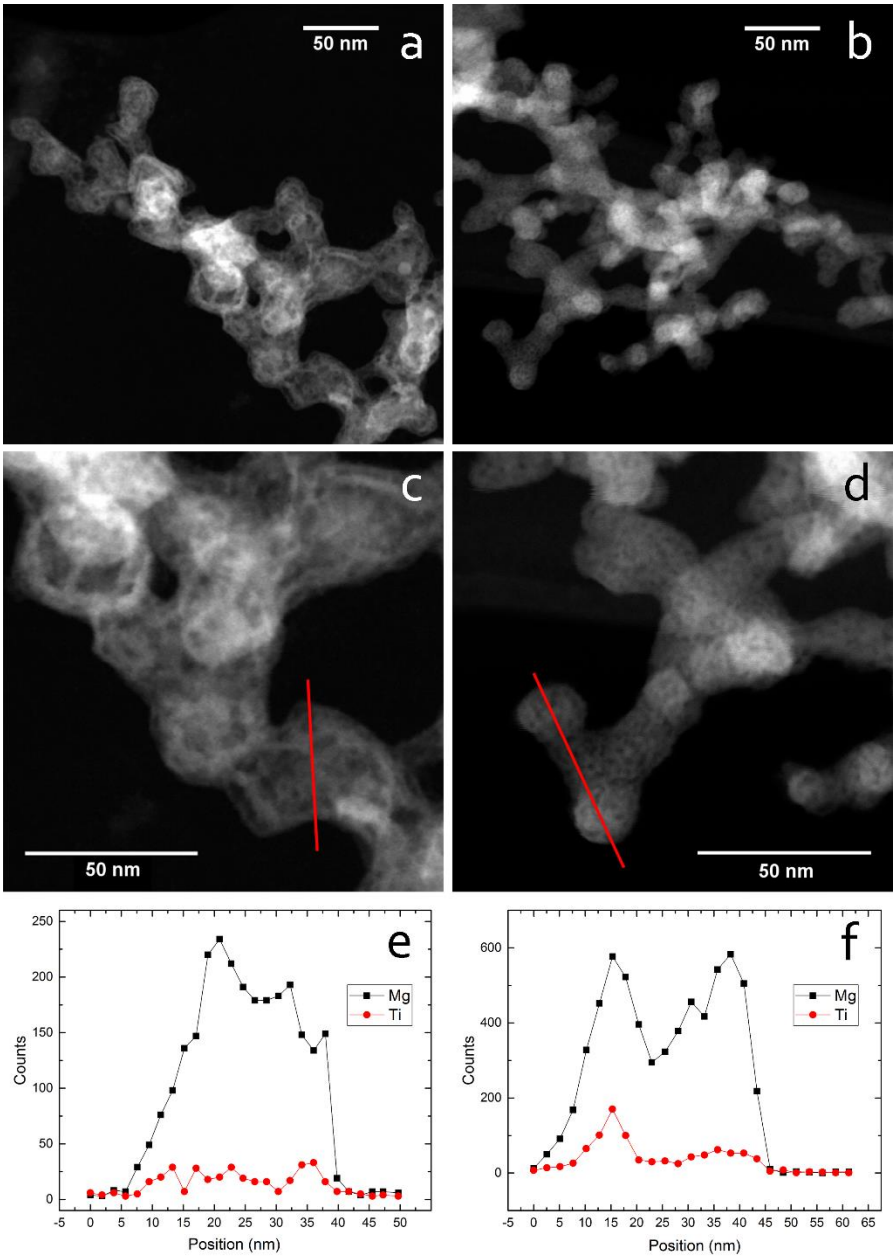

Figure 3.12. HAADF-STEM images at different magnifications of as prepared $\mathrm{Mg-6Ti-H}$ (a, c) and Mg-30Ti (b, d) as-prepared NPs; frames e, f display the corresponding STEM-EDX line scans taken along the red lines in c, d.

A deeper TEM analysis was performed in order to get a better understanding about phase arrangement within the samples. The selected area diffraction (SAD) patterns for $\mathrm{Mg-15Ti-H}$ sample is displayed in Figure 3.13, together with a plot representing the azimuthal integration of the intensity of the pattern. The x-axis represents the reciprocal vector k. The acquired pattern is different from the XRD results in Figure 3.8 and Figure 3.23, being crystalline Mg and MgO the main phases detected. This is explained by the well known high instability of $\mathrm{MgH_2}$ under the electron beam that determines the dehydrogenation[97] and partial or complete oxidation of the smaller Mg particles [61,98] exposed to the atmosphere inside the TEM column.

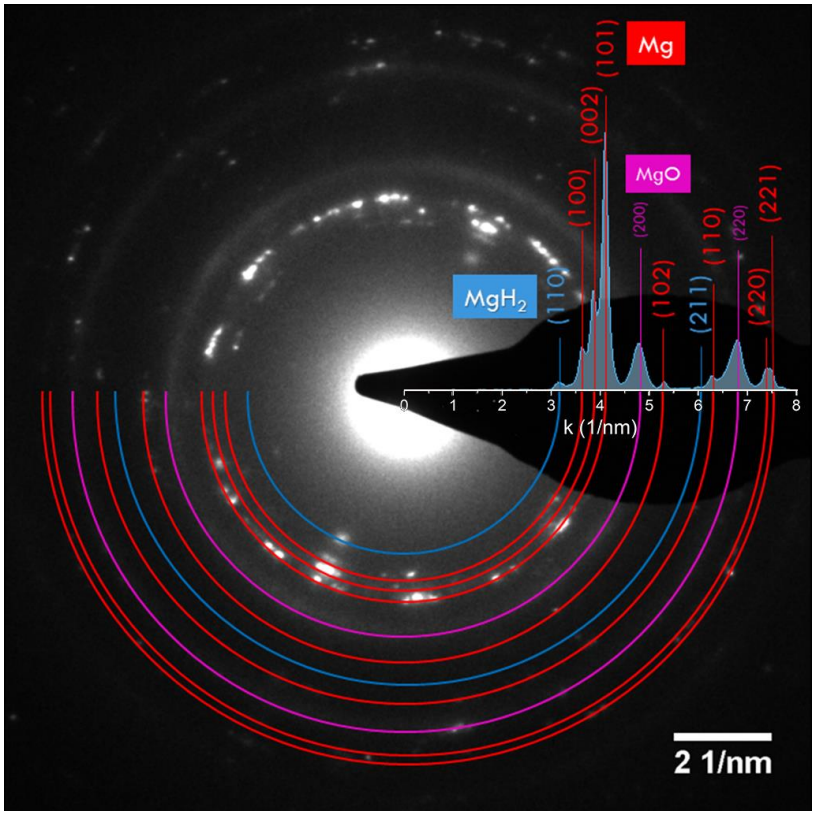

Figure 3.13. SAD acquisition for the $\mathrm{Mg-14Ti-H}$. The overlaying blue plot is obtained by azimuthal integration of the intensity of the recorded pattern as a function of the reciprocal vector k, using the plugin PASAD for the Gatan Digital Micrograph software[99]. Three phases are detected: Mg, MgO and the tetragonal $\alpha-\mathrm{MgH_2}$, highlighted in red, purple and blue respectively. The $\mathrm{TiH_2}$phase is not observed. MgO diffraction spots are not singularly distinguishable, but appear as halos, this pointing out to the small size of crystallites and their isotropic orientation. The SAD was collected right after the first exposure of the sample to the electron beam. This, together with the presence of bigger nanoparticles due to the coarsening, could explain the presence of residual $\alpha-\mathrm{MgH_2}$ spots.

The High Resolution (HR-TEM) image in Figure 3.14 displays a single nanoparticle of the $\mathrm{Mg-15Ti-H}$ sample. Applying a Fast Fourier Transform to the image, each periodicity within the HR-TEM image is represented by a bright spot. The image in Figure 3.15 is obtained by separating the contribution belonging to the different crystal phases and highlights a $\mathrm{Mg/MgO}$ core-shell structure. The MgO forms a $\sim 3\ \mathrm{nm}$ thin shell due to the slow $\mathrm{O_2}$ exposure, as reported by several works [29,94]. The small size of MgO crystals and their random orientation determines the broad halos in the SAD pattern. No evidence of $\mathrm{TiH_2}$, Ti or Ti-oxide is observed for this low Ti content sample. This is likely due to thesmall size of crystallites, to the low Ti content and partial overlapping with MgO halos, which can hinder their presence. Noticeably, two diffraction spots are detected corresponding to the rutile-type $\alpha-\mathrm{MgH_2}$ phase (110) and (211). This can be due to the presence of larger particles and the low dose impinging the sample: in fact, the SAD pattern was recorded right after the sample was firstly exposed to the electron beam. Figure 3.16 shows a part of the sample where

some bigger nanoparticles are agglomerated. Figure 3.17 is a detail of the central part of the image highlighting 3.07Å spaced fringes which correspond to the $\beta - \mathrm{MgH_2}$ (110) reflection.

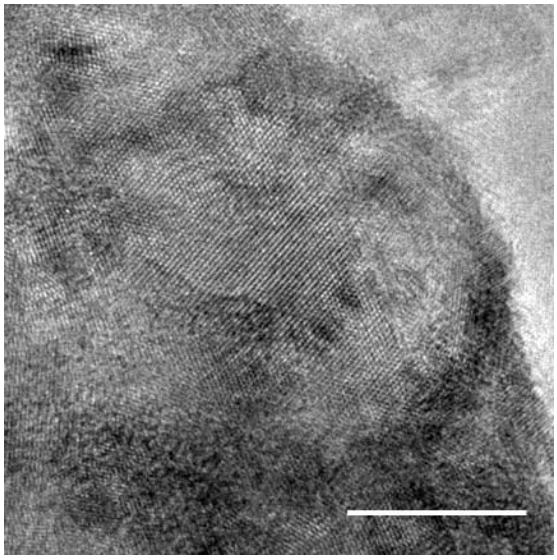

Figure 3.14. HR-TEM image of sample $\mathrm{Mg} - 15\mathrm{Ti} - \mathrm{H}$.

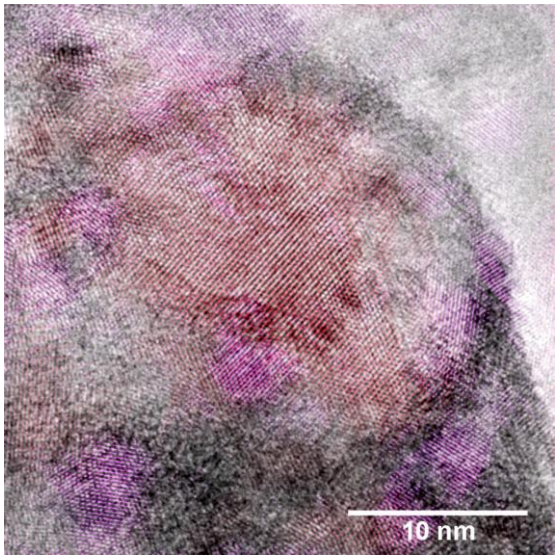

Figure 3.15. HR-TEM image of sample $\mathrm{Mg} - 15\mathrm{Ti} - \mathrm{H}$. A ~20nm core-shell NP is clearly distinguishable, where the core is constituted by a single Mg crystal whose lattice finges are highlighted in red. MgO (200) fringes are detected in the outer shell. TiH_2 fringes s are not observed.

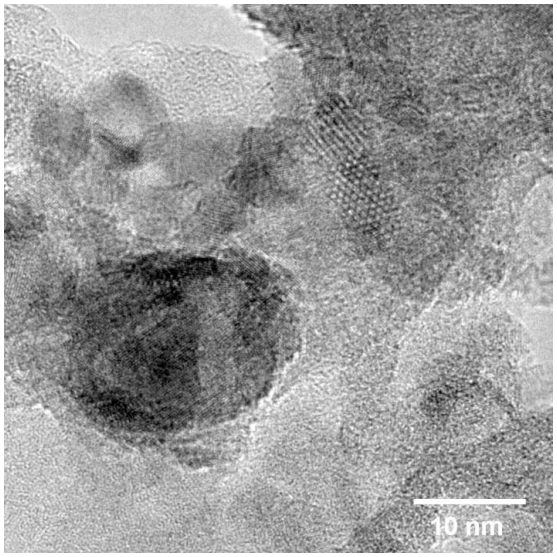

Figure 3.16. HR image of $\mathrm{Mg} - 15\mathrm{Ti} - \mathrm{H}$.

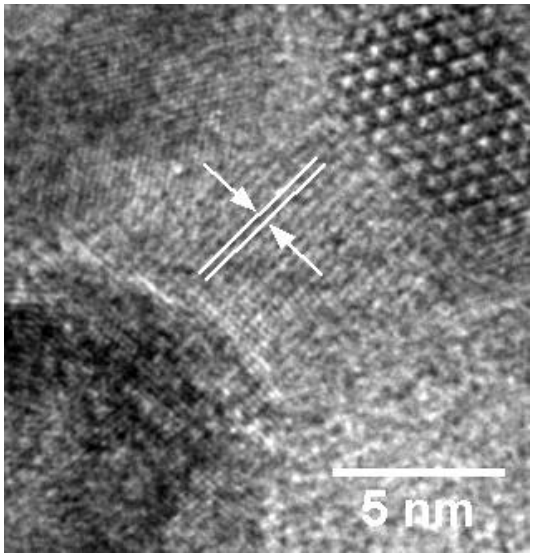

Figure 3.17. HR image of $\mathrm{Mg} - 15\mathrm{Ti} - \mathrm{H}$. The indicated lattice spacing is d=3.07Å and correspond to the rutile-type tetragonal $\alpha - \mathrm{MgH_2}$ (110).

The SAD pattern recorded for a higher Ti content sample, $Mg-46Ti-H$, is displayed in Figure 3.18. Two phases are spotted, TiH_2 and MgO, being the MgO organized as halos in the pattern, which reflects the isotropic orientation of small crystallites. The absence of metallic Mg may be due to the smaller NPs size that facilitates full oxidation by residual gaseous impurities in the TEM column. The broadening of the halos formed by the TiH_2 crystallites also suggests the presence of small TiH_2 crystallites within the sample. Neither Mg or MgH_2 phases are detected in the high Ti content samples.

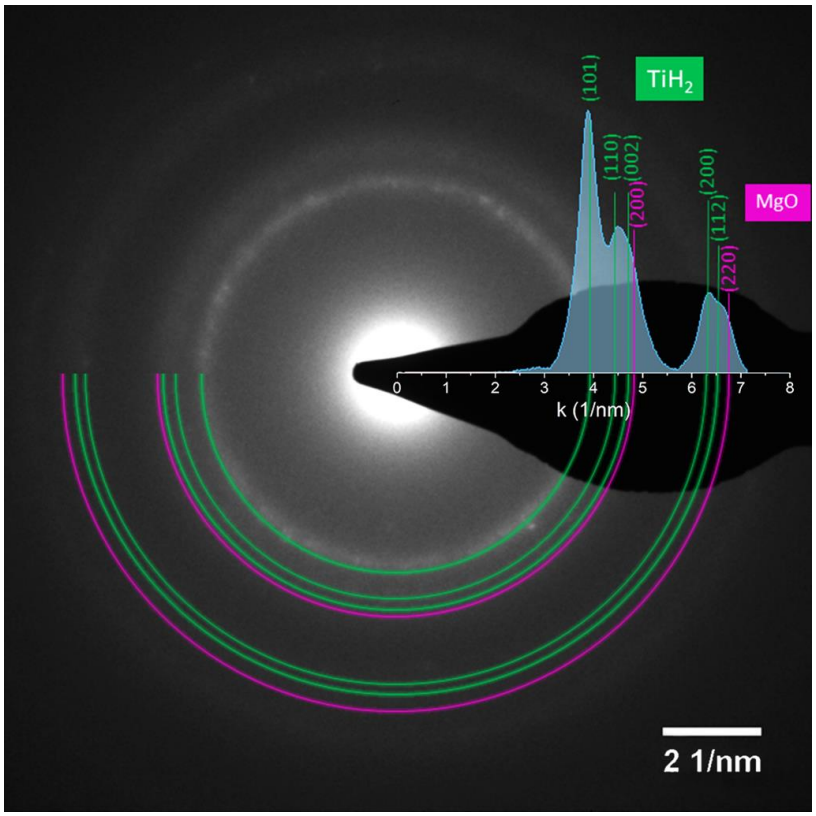

Figure 3.18. SAD acquisition for the $Mg-46Ti-H$. The overlaying blue plot is obtained by azimuthal integration of the intensity of the recorded pattern as a function of the reciprocal vector k, using the plugin PASAD for the Gatan Digital Micrograph software[99]. Two main phases are detected, TiH_2 and MgO, whose spots are organized as broad halos, pointing at the random orientation and small size of the crystals. The corresponding diffraction spots and halos are highlighted with green and purple circles respectively.

In this sort of *post mortem* scenario, one can figure out the original spatial distribution of TiH_2 and MgH_2 phases through HR-TEM images that highlight the lattice spacing of TiH_2 (111) and MgO (200), as shown in Figure 3.19 and Figure 3.20 for the $Mg-46Ti-H$ sample. Here ~ 10 nm NPs TiH_2 crystallites are seen in close proximity to MgO crystallites, indicating that many MgH_2/TiH_2 interfaces were present in the samples before the decomposition under the electron beam. These interfaces are the

subject of the discussion of Chapter 3.6 and 3.7, centered on improved hydrogen thermodynamics and kinetics of $Mg - Ti - H$ NPs.

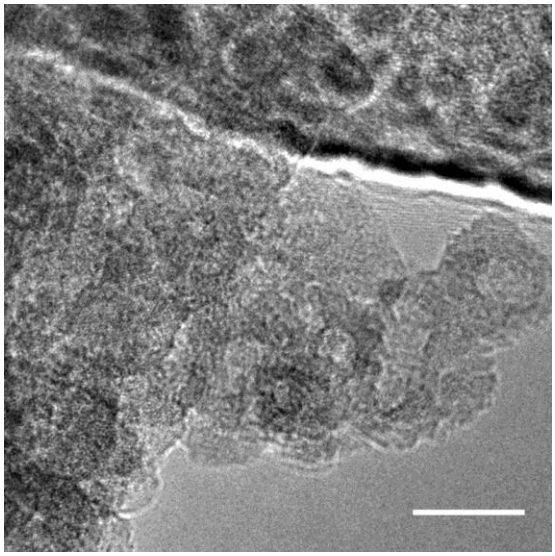

Figure 3.19. HR-TEM image of the $Mg - 46Ti - H$ sample, spotting agglomerated NPs suspended on a hole of the carbon tape of the TEM grid.

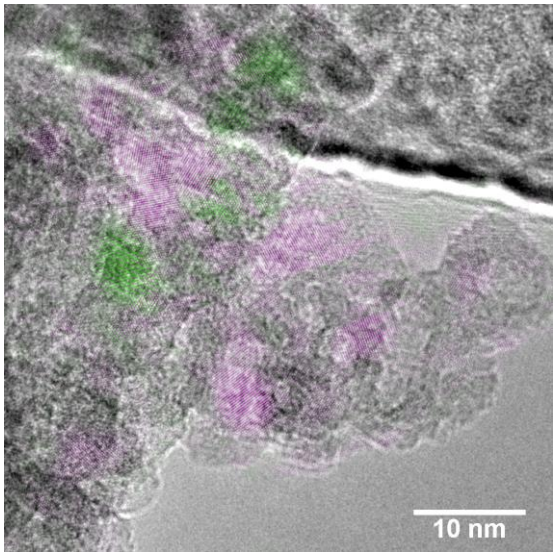

Figure 3.20. The fringes corresponding to the MgO (200) fringes and TiH_2(111) family of planes are highlighted in magenta and green, respectively.

3.5.2. Coarsening and thermal stability

Mild temperature regime ($373 - 423$ K)

The samples discussed in this chapter were analyzed in the relatively mild temperature range $373 - 423$ K in order to avoid as much as possible the evolution and coarsening effects and to address thermodynamic and kinetic properties to the peculiar structure of the samples. The $Mg - Ti - H$ NPs exhibit good thermal stability in the investigated temperature range. Samples with lower Ti content exhibit coarsening of the microstructure, as demonstrated by the presence of some larger Mg NPs in the STEM image in Figure 3.21a,c. However, most of the sample preserves its original morphology and elemental distribution, as displayed in Figure 3.21b,d.

This picture is confirmed by the HR-TEM image in Figure 3.22a, performed over a locally coarsened area (Figure 3.22b), in where Mg (101) are highlighted. The particle is constituted by Mg, while only the MgO phase is detected on the smaller ~ 10 nm nanoparticles.

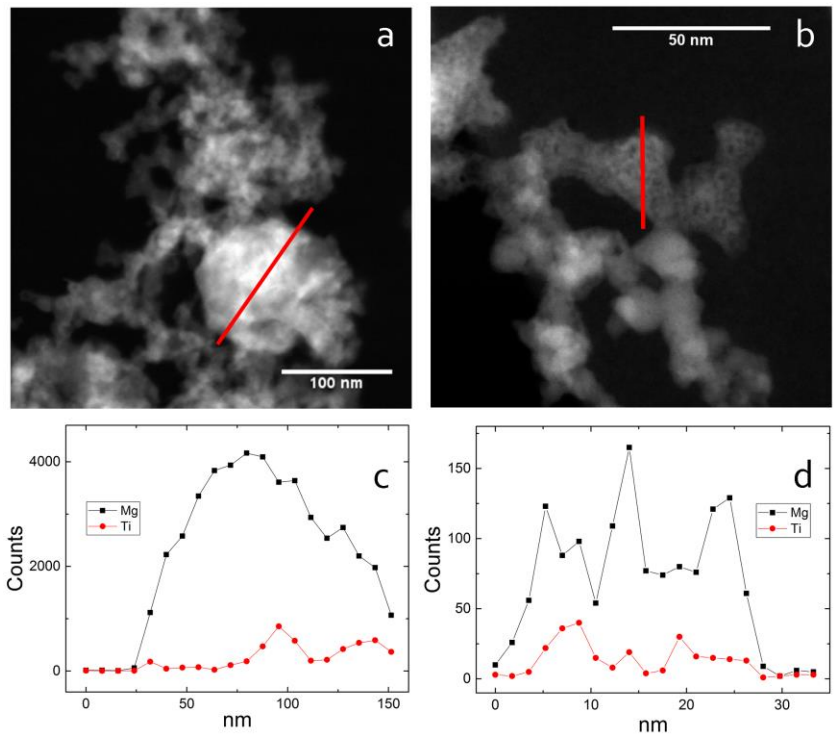

Figure 3.21. (a, b) HAADF-STEM images of $Mg-15Ti-H$ NPs subjected to hydrogen sorption measurements at T<425 K; c and d represent the STEM-EDX line scans taken along the red lines in a and b, respectively.

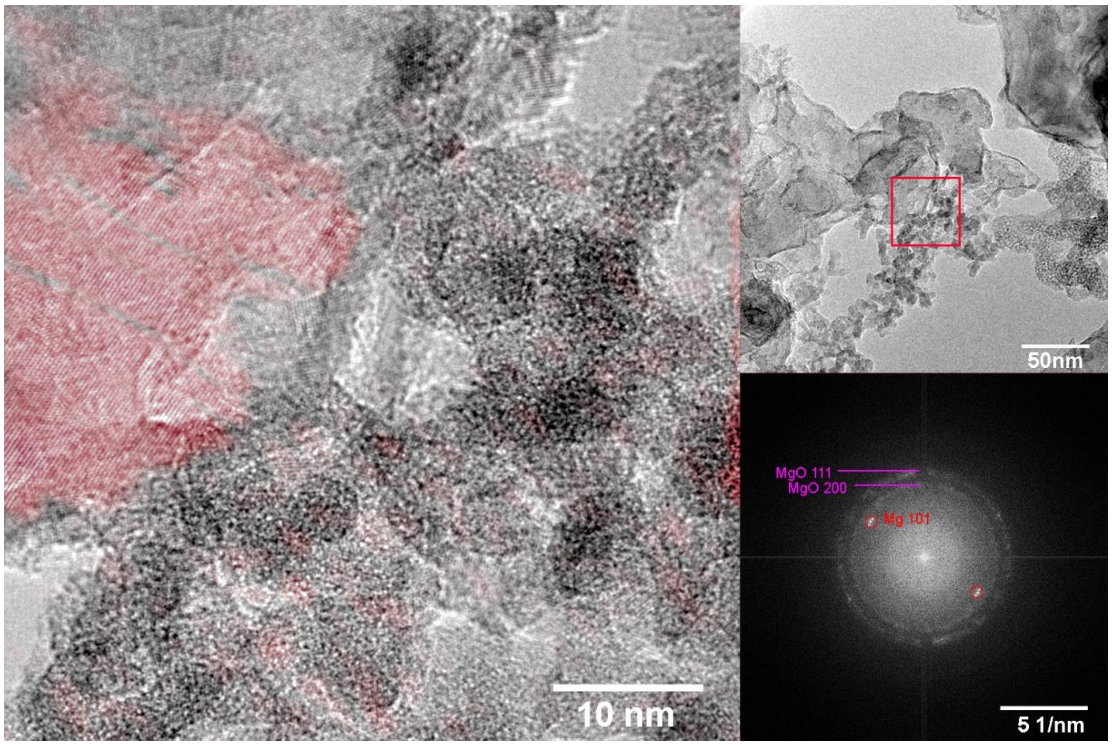

Figure 3.22. HR image of $Mg-15Ti-H$.The corresponding LR image spots the presence of larger nanoparticles (50-80nm in diameter) which results from the coarsening of the nanostructure. The Mg(101) lattice fringes highlighted in the HRTEM image are indicated also in in the Fast Fourier transform of the image. The smaller nanoparticles (~10nm) are mostly oxidized, corresponding to the MgO (111) and (200) halos in the FFT.

High Temperature regime (> 430 K)

In general, the thermal stability is determined by the Ti content and the time/temperature history. The Rietveld analysis of the XRD patterns in Figure 3.23 recorded for samples repeatedly cycled at higher temperature (> 430 K) is reported in Table 3.4, revealing the presence of 80 nm diameter $\mathrm{MgH_2}$ crystallites in the $\mathrm{Mg-6Ti-H}$ sample. In Figure 3.24, STEM-EDS analysis spots the morphological evolution of the $\mathrm{Mg-6Ti-H}$ sample exposed to high temperature, revealing two features: (1) the presence of bigger NPs hundreds of nm in size and mainly composed of Mg where Ti is not evenly distributed but is localized in larger crystals, compatibly with the larger $\mathrm{TiH_2}$ observed in the XRD pattern analysis and (2) almost Mg emptied NPs appearing with a hollow morphology. This can be attributed to the Mg diffusion and sublimation during multiple sorption processes at high temperature[100].

Table 3.4. Results for Rietveld refinement of XRD profiles for the NPs after hydrogen sorption cycles at $T > 430$ K. The numbers in parentheses represent the standard deviations referred to the last digit. Where (*) is given, the parameter was fixed to ensure fit stability due to the low phase amount and/or very small crystallite size.

X_{Ti}	α-$\mathrm{MgH_2}$				ε-$\mathrm{TiH_2}$				MgO	γ-$\mathrm{MgH_2}$	Mg	R_{wp}	R_{exp}
at.%	wt%	$d_{\mathrm{MgH_2}}$ (nm)	*a* (Å)	*c* (Å)	wt%	$d_{\mathrm{TiH_2}}$ (nm)	*a* (Å)	*c* (Å)	wt%	wt%	wt%	(%)	(%)
after hydrogen sorption cycles at T> 430 K													
6(1)	78(5)	80(8)	4.5193(2)	3.0225(1)	13(2)	4(*)	3.1831(*)	4.386	9(1)	0	0	5.5	2.8
30(3)	36(4)	25(3)	4.5207(4)	3.0242(3)	55(5)	7(1)	3.1831(7)	4.386(2)	9(1)	0	1	5.1	2.1
60(5)	7(2)	14(*)	4.529(2)	3.0267	85(7)	8(1)	3.192(1)	4.381(2)	8(2)	0	0	6.4	2.8

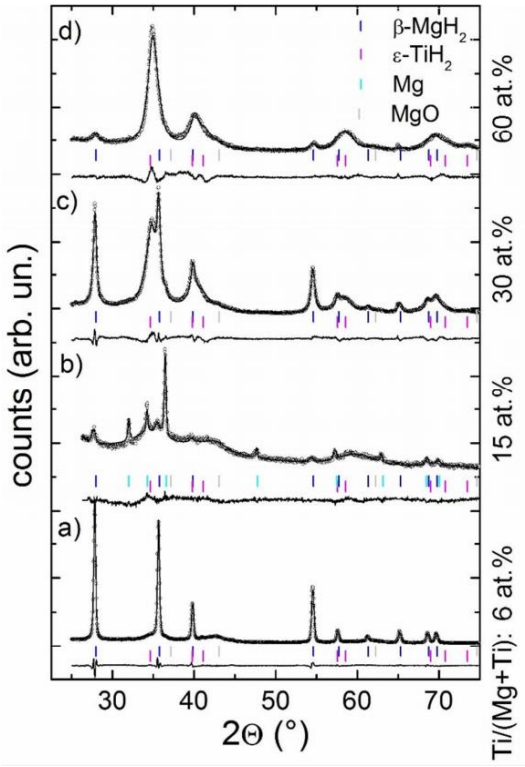

Figure 3.23. XRD patterns of $\mathrm{Mg-Ti-H}$ NPs after hydrogen sorption cycles at elevated temperature ($T > 430\ \mathrm{K}$). Open circles are experimental data while the calculated Rietveld best fit is represented by the solid line. The fit residual is shown below each pattern, and the coloured vertical bars mark the Bragg reflections of the main crystalline phases. The sample $\mathrm{Mg-15Ti-H}$ (shown in b) underwent a hydrogen desorption at $423\ \mathrm{K}$ before XRD analysis and therefore metallic Mg overwhelms $\mathrm{MgH_2}$. For the other samples, the last step was hydrogen absorption: metallic Mg was not detected in these cases.

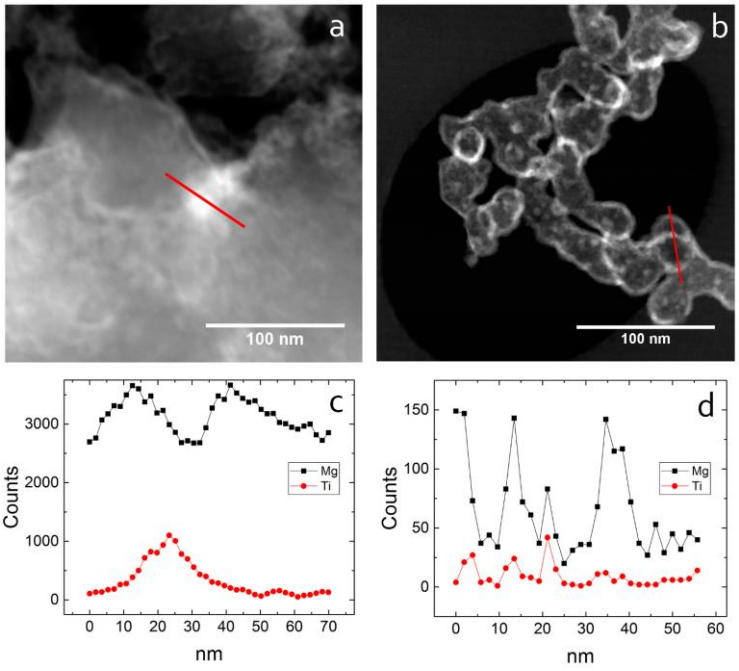

Figure 3.24. HAADF-STEM images (a,b) of the $\mathrm{Mg-6Ti-H}$ sample subjected to sorption cycles up to $523\ \mathrm{K}$. The STEM-EDS profiles acquired along the red lines are reported in c and d, respectively.

3.6. Results: Kinetics of Mg-Ti-H NPs

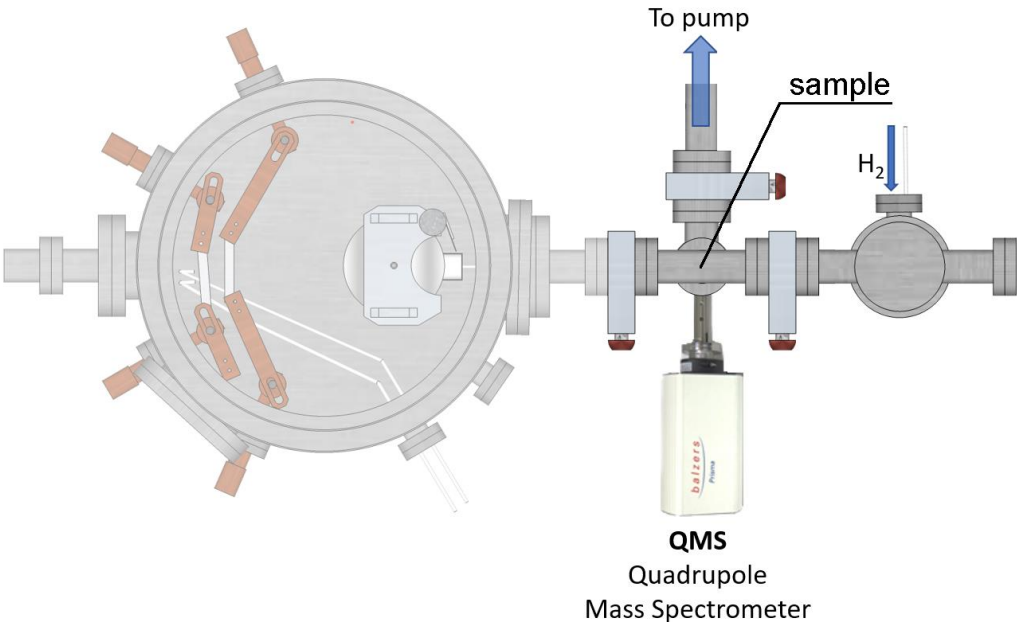

Figure 3.25. The in-situ Sievert-type apparatus is highlighted, showing the position of the sample, the H_2 inlet and outlet, and gate valves. The Quadrupole Mass Spectrometer is placed in proximity of the sample.

Before going into the results, a brief description of the system and the measurement procedure is given. A manometric Sievert apparatus relates the hydrogen uptake and release to the pressure variations in a calibrated volume kept in isothermal conditions. In the relatively mild conditions of our experiments ($p < 1\ \mathrm{MPa}$), the ideal gas law can be applied to calculate the H_2 moles exchanged by the sample. For this purpose, the secondary chamber was turned into a Sievert type apparatus, as anticipated in Chapter 2.4, by calibrating its volume (~5 liters) and adding a ceramic pressure sensor that enabled to follow the H-exchange with the examined sample. Pressure data are recorded with a *LabVIEW* software designed in the framework of this Thesis. The sample, collected into a vial, is heated by a surrounding winding connected to a power supply.

3.6.1. Experimental

The kinetic experiments were carried out in this chamber (Figure 3.25) equipped with a Pfeiffer QMS 200 quadrupole mass spectrometer and a Varian Capacitance Diaphragm Gauge (CDG) for measurement of the absolute pressure from 1 to $10^5\mathrm{Pa}$. The NPs were contained in a glass ampoule that could be heated by an externally wound wire resistance connected to a power supply and temperature controller. A typical sample consisted in about $50\ \mathrm{mg}$ of NPs.

Before starting the kinetic measurements, the NPs were soaked in $20\,\mathrm{kPa}$ hydrogen at $423\,\mathrm{K}$ for about 1 hour. These conditions are known to induce complete formation of the hydride phase[85]. Afterwards, hydrogen desorption kinetics were measured isothermally under high vacuum ($\sim 10^{-2}\,\mathrm{Pa}$) by recording the QMS ion current for $m/Z = 2$ while the chamber was dynamically evacuated using a turbomolecular pump. An example of the raw data is shown in Figure 3.26.

The hydrogen absorption kinetics were measured by using the CDG to monitor the pressure decrease $\Delta p(t) = p(t) - p_{in}$, where p_{in} is the initial pressure. For all measurements, $\Delta p \ll p_{\mathrm{in}}$ so that the experiments are isobaric to a good approximation. The value of p_{in} at each temperature was chosen in order to keep constant the driving force of the transformation, e.g. the ratio $p_{\mathrm{in}}/p_{\mathrm{abs}}$ where p_{abs} is the plateau pressure for absorption[98]. This procedure is of extreme importance to determine correctly the temperature dependence of the kinetic parameters. In Figure 3.27, an example of raw $\Delta p(t)$ data at the different temperatures is given. The value of p_{abs} was estimated by stepwise pressure increases: once the start of absorption was determined, the chamber was evacuated again to attain the fully unloaded state, the pressure was set to $p_{in} \sim 18\, p_{\mathrm{abs}}$, and the absorption kinetics were recorded.

The reversible gravimetric capacity ρ_m was determined from the maximum Δp value and the previously calibrated volume of the chamber. The value of ρ_m was also used to convert the integrated ion current measured during desorption kinetics into a mass change. For all samples, the temperature sequence was 150, 100, and $125°\mathrm{C}$. Finally, one cycle of desorption and absorption was carried out again at $150°\mathrm{C}$ to check reproducibility.

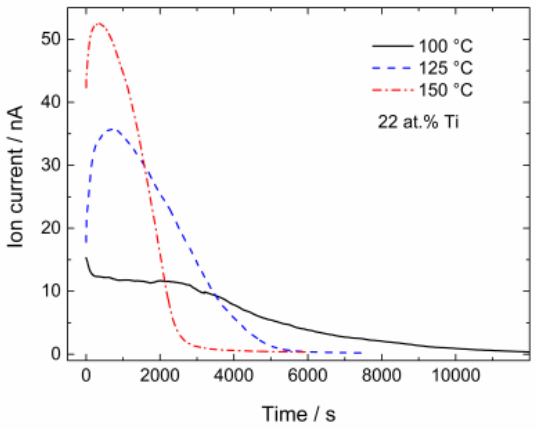

Figure 3.26. Ion current corresponding to the $\boldsymbol{m/Z = 2}$ signal recorded with QMS for the H-desorption kinetics of sample $\mathrm{Mg-22Ti-H}$ at different temperatures.

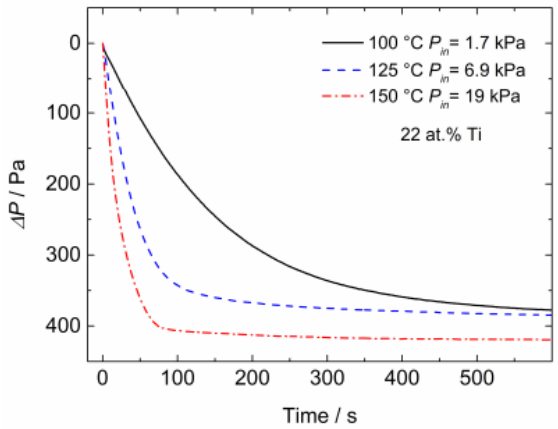

Figure 3.27. Pressure change $\Delta p(t)$ at different temperature for $\mathrm{Mg-22Ti-H}$ sample. The initial pressure p_{in} reported in the legend was chosen to provide the same driving force for hydride formation.

3.6.2. Measurements and analysis of the Kinetics

Figure 3.28 and Figure 3.29 displays, respectively, the full collection of absorption and desorption kinetics at 100, 125 and $150\,°\mathrm{C}$ for different Ti loadings ($X_{\mathrm{Ti}} = 14, 22, 46, 63\ \mathrm{at\%}$).

The absorption process is impressively fast. At $150°\mathrm{C}$, all the samples in the collection reach 90% of the total gravimetric capacity ρ_m in less than $100\,s$, and the transformation rate increases with the X_{Ti}. The desorption process is significantly slower, as generally expected for Mg-based systems, but still impressive considering the low temperature range of the experiments, that requires the addition of expensive noble metal catalysts like Pd for H-release to be observable. For comparison, at $150°\mathrm{C}$ it takes $\sim 2000\,s$ for 90% of the total stored $\mathrm{H_2}$ to be released. Again, the rapidity of the process increases with X_{Ti}, at the expenses of the total ρ_m, as reported also by many other studies[45,93]. This can be related with the high stability of $\mathrm{TiH_2}$, which does not decompose under these thermodynamic conditions. The reversible capacity ρ_m, are compatible with the $\mathrm{MgH_2}$ content determined from the XRD analysis reported in the previous section (Table 3.3).

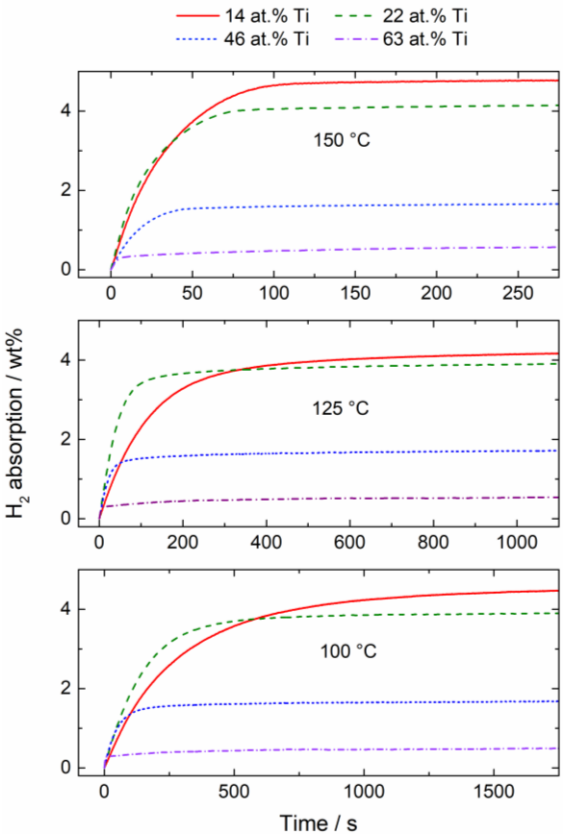

Figure 3.28. Hydrogen absorption kinetics for all samples and temperatures.

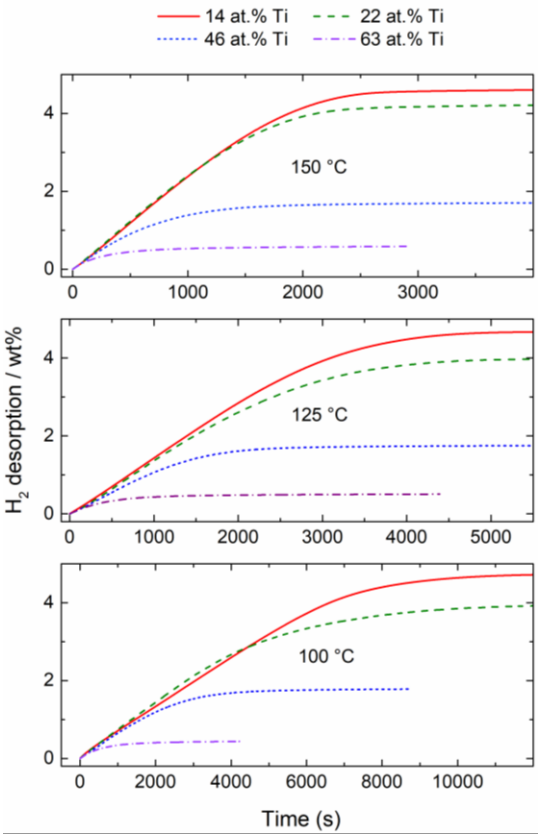

Figure 3.29. Hydrogen desorption kinetics for all samples and temperatures.

3.6.3. Absorption Kinetics

To correlate the kinetics with the Ti content and to calculate the activation energy as a function of Ti content, we have to identify the kinetic model ruling the H-sorption process. The following single nanoparticle models have been taken into consideration, as commonly reported for the metal to hydride kinetics analyses[101,102]:

Johnson-Mehl-Avrami-Kolmogorov (JMAK). This model assumes the random nucleation and growth of the new phase both in the bulk and surface of the particle and the transformed fraction as a function of time $\alpha_{NG}(t)$ is expressed by $\alpha_{NG}(t) = 1 - \exp(-(k_{NG}t)^n)$, where k_{NG} is the rate constant, and n is the Avrami parameter, which can be further developed as $n = a + bd$, where a ranges from 0 (instantaneous nucleation) to 1 (constant nucleation rate), b is $1/2$ for diffusion limited or 1 for interface limited growth and d stands for the growth dimensionality. It is possible to identify a function $F_{NG}(\alpha)$ which is linear with the time:

$$F_{NG}(\alpha) = -(\ln(1-\alpha))^{1/2} \quad = k_{NG}t \tag{3.9}$$

Contracting Volume (CV). In this case, the new phase initially develops as a thin layer at the surface which expands towards the core of the nanoparticle. When the interface between the two phases progresses at constant velocity, one has $\alpha_{CV}(t) = 1-(1-k_{CV}t)^n$ where n is the growth dimensionality. Again, we can easily identify a simple relation linear with the time

$$F_{CV}(t) = 1-(1-\alpha)^{1/n} = k_{CV}t \tag{3.10}$$

In case where the H diffusion through the new phase is the rate limiting process, then the velocity of the boundary decreases with time and the analysis becomes rather complex. In that case the equation that best fits the experimental results is

$$F_{CV}^{\mathrm{dec}}(t) = 1-\left(\frac{2\alpha}{3}\right)-(1-\alpha)^{\frac{2}{3}} = k_{CV}^{\mathrm{dec}}t \tag{3.11}$$

Surface-limited (SL). As the name suggest, the model assumes that the rate limiting process is the dissociation/recombination of the $\mathrm{H_2}$ molecules at the surface. In this case the transformed fraction is proportional to the time, as in

$$F_{SL}(t) = k_{SL}t \tag{3.12}$$

A first hint at the kinetic model that best describes the transformation can be gained by inspecting the linearity of the relevant expression for $F(\alpha)$. Figure 3.30 displays an example of this approach applied to the absorption of the $\mathrm{Mg-22Ti-H}$ sample at $100°\mathrm{C}$ temperature. Here we see that $F_{NG}(\alpha),\ n=1.$ is linear up to a time, for which $\alpha \approx 0.85$, whereas the other models deviate significantly from linearity.

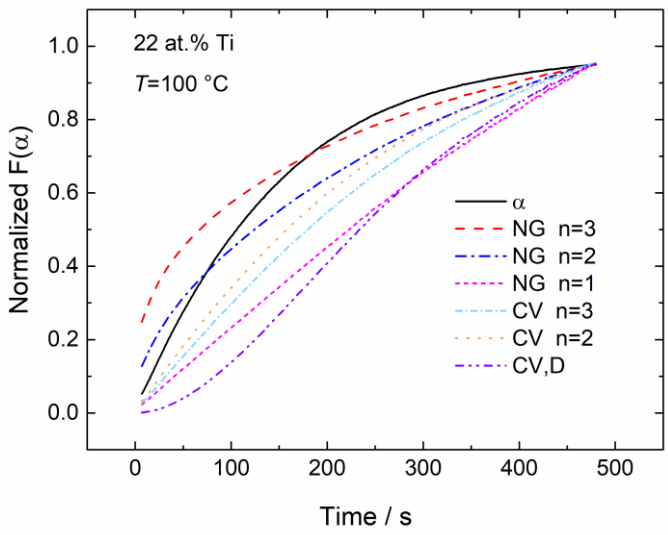

Figure 3.30. Analysis of different kinetic models applied to H-absorption by the $\mathrm{Mg-22Ti-H}$ NPs at 100°C. The $F_{NG}(\alpha),\ n=1$ model is the one that best fits the linear behavior.

After the identification of the JMAK model, we proceed to the non-linear fit of $\alpha(t)$, in order to obtain the kinetic parameter k_{NG} and the Avrami parameter n. Figure 3.31 shows the quality of the fit applied to $\mathrm{Mg-22Ti-H}$ sample at different temperatures.

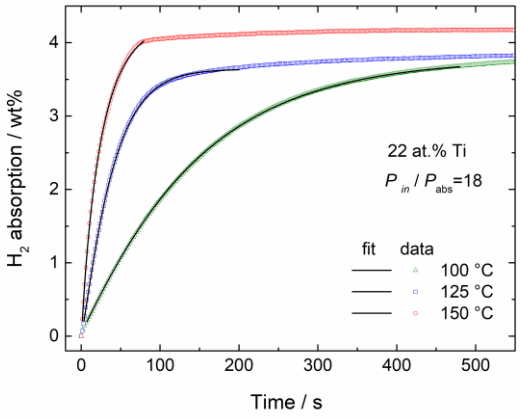

Figure 3.31. Result of the non-linear fit (black solid line) applied to the absorption data for $\mathbf{Mg-22Ti-H}$sample at different temperatures ($\mathbf{100}$, $\mathbf{125}$ and $\mathbf{150°C}$).

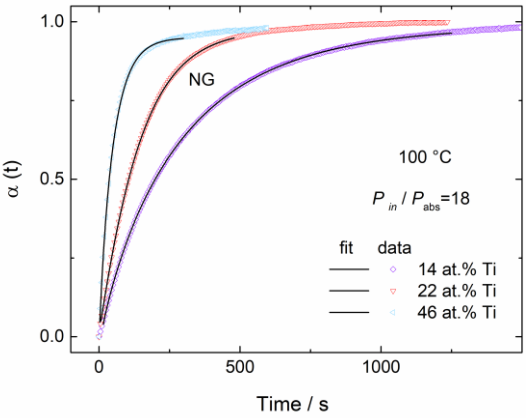

Figure 3.32. Result of the non-linear fit (black solid line) applied to the absorption data at different temperature $\boldsymbol{T=100°C}$ and varying $\mathbf{Ti}$ content ($\boldsymbol{X_{Ti}=14,22,46}$ at%).

Figure 3.32, similarly, shows the results of the fitting procedure applied to the absorption kinetics of different samples at the same temperature $T=100°\mathrm{C}$. The same model applies to all the composition reported. The small variations of n in the $0.9-1.1$ range do not reveal any significant relation with X_{Ti}, , while the activation energy is decreases with X_{Ti}.The values for E_a and k calculated as $150\ °\mathrm{C}$ are summarized in Table 3.5.

For the sample with higher Ti content ($Mg-63Ti-H$), the absorption kinetics was so fast that it was not possible to keep track of the initial part of the transformation, meaning that it has not been possible to carry out any reliable quantitative analysis on the absorption data. The initial stage of the transformation is surprisingly steep, as shown in Figure 3.33a, suggesting that the absorption process for this sample is the composed result of two markedly distinct thermodynamics. This is confirmed by Figure 3.33b, where two subsequent absorption processes are compared: the first one, (black line) having a starting pressure which is far below the equilibrium pressure of Mg bulk, completes in few seconds while the second one (red line), requires higher pressures for the transformation to start.

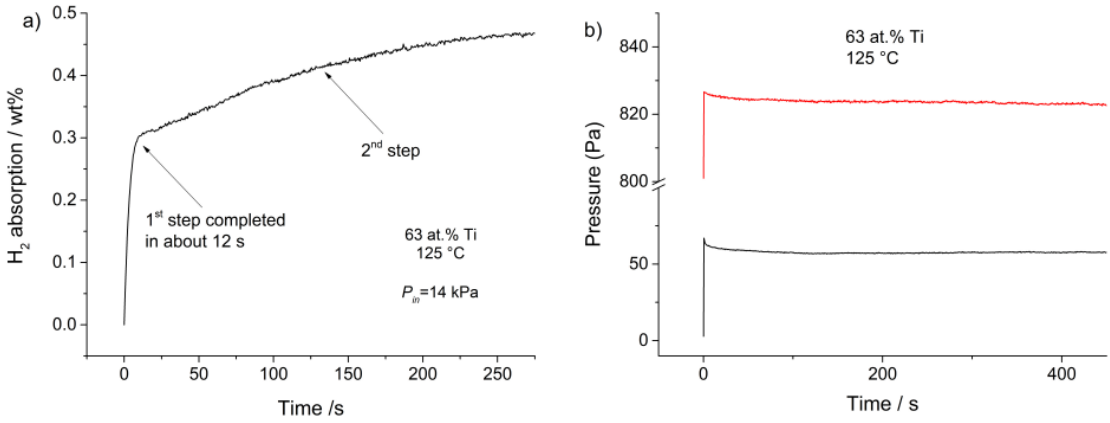

Figure 3.33. Absorption kinetics for sample $Mg-63Ti-H$ at 125°C. The left panel displays the overall kinetics. In the right panel, are represented two consecutive kinetics: the first (one) at lower pressures (~ 70 Pa) is completed within seconds; the second (red line) requires higher pressures to start the absorption process.

Assuming an Arrhenius-like temperature dependence of the rate constant,

$$k(T) = k_0 \exp\left(-\frac{E_a}{RT}\right) \tag{3.13}$$

we can estimate the activation energy E_a associated with the rate-limiting step of the transformation. The Arrhenius plots for absorption are reported in the top part of Figure 3.37. The corresponding E_a values, listed in Table 3.5, span in the $43-52$ kJ/mol range, much lower than for hydrogen absorption in pure Mg [103]. Such a low activation barrier explains the observed outstanding absorption kinetics.

3.6.4. Desorption Kinetics

Understanding the mechanism ruling the desorption process is, if possible, even more important because it is the key to further improve the H-sorption kinetics. We applied the same approach as in the absorption case. In Figure 3.34, we observe that no one of the proposed models is linear over the complete transformation. However, the transformed fraction itself is time-linear up to the first half of the transformation is completed, as expected from a Surface-Limited model (represented as a black solid line), while the second half is better described by a Contracting Volume model with either $n = 2$ or $n = 3$.

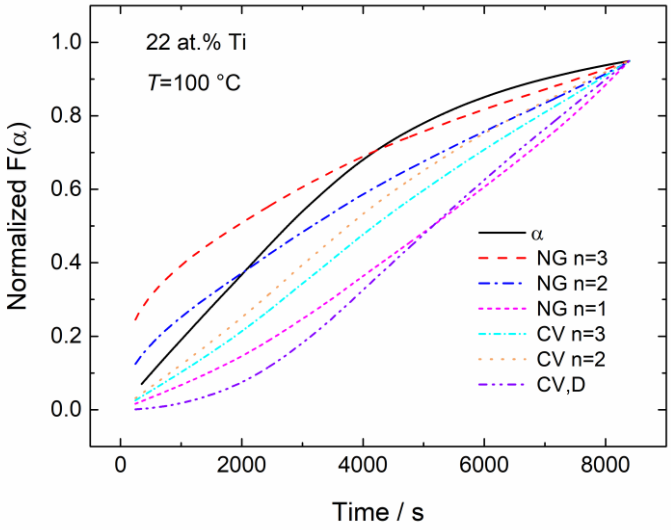

Figure 3.34. Analysis of different kinetic models applied to H-desorption by the $\mathrm{Mg-22Ti-H}$ NPs at 100°C.

To obtain the relevant kinetic parameters, the kinetics with a model composed of two equations

$$\begin{aligned} \alpha(t) &= k_{SL}t && t < \tilde{t} \\ \alpha(t) &= k_{SL}\tilde{t} + (1 - k_{SL}\tilde{t})\,\alpha_{CV}(t-\tilde{t}), && t \geq \tilde{t} \end{aligned} \tag{3.14}$$

Where the fit parameters are k_{SL}, k_{CV}, t and n and $\alpha_{CV}(t-\tilde{t})$ is the time-shifted equation for the CV model. The result of the fitting operation is shown in Figure 3.35 for different temperature and in Figure 3.36 for different samples. The values for E_a and k calculated as $150\ °\mathrm{C}$ are reported for the initial part of the transformation and are summarized in Table 3.5. The activation energy span in the range $31 - 35\ \mathrm{kJ/mol}$ for all the samples, and the kinetic parameter k increases with the Ti content. The kinetic

parameter k is an order of magnitude smaller in the desorption process, as shown in the Arrhenius plots in Figure 3.37, even if the desorption energy barrier E_a is smaller than the one calculated in the absorption case. The sample with $X_{\mathrm{Ti}} = 63\ \mathrm{at\%}$, differently from the others, is well described by a JMAK model with $n \approx 1$ and the activation energy is even lower ($23\ \mathrm{kJ/mol}$) but suffer from a large uncertainty.

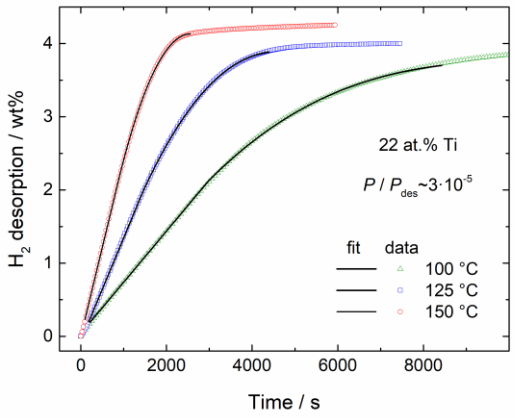

Figure 3.35. Result of the non-linear fit (black solid line) applied to the desorption data for $\mathrm{Mg-22Ti-H}$ sample at different temperature (100, 125 and $150°C$).

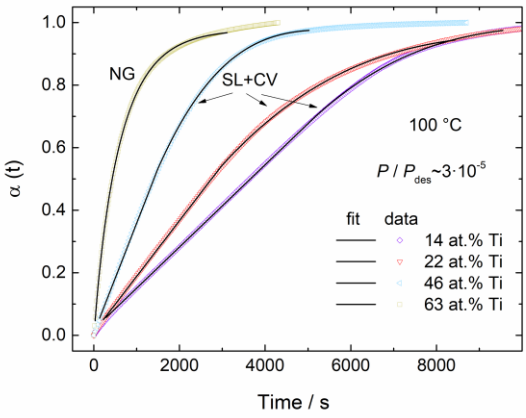

Figure 3.36. Result of the non-linear fit (black solid line) applied to the desorption data at different temperature $\mathrm{T} = 100°\mathrm{C}$ and varying Ti content ($X_{\mathrm{Ti}} = 14, 22, 46\ \mathrm{at\%}$).

3.6.5. Discussion

The mechanism behind the catalytic role of certain additives in the $\mathrm{Mg/MgH_2}$ sorption kinetics has widely been investigated. In the case of the benchmark catalyst $\mathrm{Nb_2O_5}$, Barkhordarian et al.[70] found that the desorption kinetics is SL at low catalyst content and start to follow a CV model with increasing catalyst loading. The activation energy correspondingly decreases from $72\ \mathrm{kJ/mol}$ to $62\ \mathrm{kJ/mol}$. The absorption kinetics for these samples followed a diffusion-controlled CV model. Using V as catalyst, Liang et al[104] showed that the desorption kinetics at high temperature and high driving force follow a CV model with activation energy of $52\ \mathrm{kJ/mol}$. These values are all significantly lower than $120–150\ \mathrm{kJ/mol}$ reported for non-catalysed Mg[98,105],but are larger than the $31–35\ \mathrm{kJ/mol}$ obtained for the desorption kinetics of $\mathrm{Mg-Ti-H}$ NPs discussed in this Thesis.

Coming now to $\mathrm{TiH_2}$, Choi et al[106] obtained an activation energy of $73\ \mathrm{kJ/mol}$ for desorption in ball-milled $\mathrm{MgH_2-TiH_2}$ composites with 9.1 mol% $\mathrm{TiH_2}$. The kinetic mechanism was not investigated but it was proposed that the weakening of the Mg –

H bond induced by TiH_2 incorporation may be responsible for the enhanced kinetics. Using X-ray and neutron diffraction on deuterated $MgD_2 - TiD_2$ ball-milled composites, Ponthieu et al.[107] demonstrated that TiH_2 favours H mobility through the existence of coherent MgH_2/TiH_2interfaces and the presence of sub-stoichiometric $MgH_{2-\eta}$ and $TiH_{2-\eta}$ phases. The rate limiting mechanism at $548\ K$ was identified in hydrogen diffusion through the hydride for absorption and in Mg/MgH_2 interface displacement for desorption.

However, the aforementioned studies examined hydrogen sorption at significantly higher temperatures (typically $523–\ 623\ K$). Moreover, the size of Mg/MgH_2 particles was about 2–3 orders of magnitude larger than our $Mg-Ti-H$ NPs. It is therefore not surprising that different kinetic mechanisms could come into play. In fact, those mechanisms characterized by higher values of the pre-exponential factor of the pre-exponential factor k_0 and of E_a that dominate above a certain temperature can become slower than other mechanisms characterized by lower k_0 and E_a when the temperature is decreased.

Table 3.5 Summary of structural and kinetic data on the four $Mg-Ti-H$ NPs samples. Ti content, average nanoparticle diameter d_{NP}, hydrogen reversiblecapacity ρ_m, kinetic model used for the fitting, rate constant k at 150°C and activation energy Ea obtained from the temperature dependence of k. The numbers in parenthesis represent the standard deviation in units of the last significant digit.

			Absorption			Desorption		
X_{Ti}	d_{NP}	ρ_m	Model	E_a	k	Model	E_a	k
at.%	nm	wt%		kJ mol^{-1}	$10^{-3}s^{-1}$		kJ mol^{-1}	$10^{-3}s^{-1}$
14(2)	14(2)	4.8(1)	NG, $n \approx 1$	52(4)	27(1)	SL+CV [(a)]	35 (3)	0.52 (1) [(c)]
22(2)	14(2)	4.2(1)	NG, $n \approx 1$	47(6)	40(1)	SL+CV [(a)]	31 (2)	0.59 (1) [(c)]
46(3)	10(2)	1.8(1)	NG, $n \approx 1$	43(5)	92(2)	SL+CV [(b)]	31 (3)	1.17 (2) [(c)]
63(5)	7(2)	0.60(5)				NG, $n \approx 1$	23 (5)	3.5(1)

(a) For CV kinetics, n ¼ 3 at 100°C while n ¼ 2 at 125°C and 150°C. (b) For CV kinetics, n ¼ 3. (c) The rate constant of the SL initial stage is reported.

The results obtained for $Mg-Ti-H$ NPs are reported in Table 3.5 and the correspondent Arrhenius plots for absorption and desorption are shown in Figure 3.37 for direct comparison.

In Chapter 3.6.3, the absorption kinetics was found to follow a NG model with $n \approx 1$. Since a constant nucleation rate implies that $n \geq 3/2$, this finding suggests that nucleation is almost instantaneous, meaning that it takes place on a shorter time scale compared to the growth. The value $n \approx 1$ means also that the growth of nuclei can be either 2-dimensional limited by diffusion or 1-dimensional controlled by interface

motion. With increasing Ti content, three factors may contribute to the observed speed up of the absorption reaction. First, the increase in the number of nucleation sites associated with Mg/TiH_2 interfaces within the NPs. Second, the decrease of the average NP size. Third, the barrier associated with atom H diffusion or MgH_2 interface motion may also be lowered by the abundance of TiH_2 and possibly by sub-stoichiometric interfacial phases[89,108]. The values listed in Table 3.5 for absorption indeed seem to suggest a slight decrease of E_a with increasing Ti content. However, the rather large uncertainties do not permit to draw a clear conclusion in this respect.

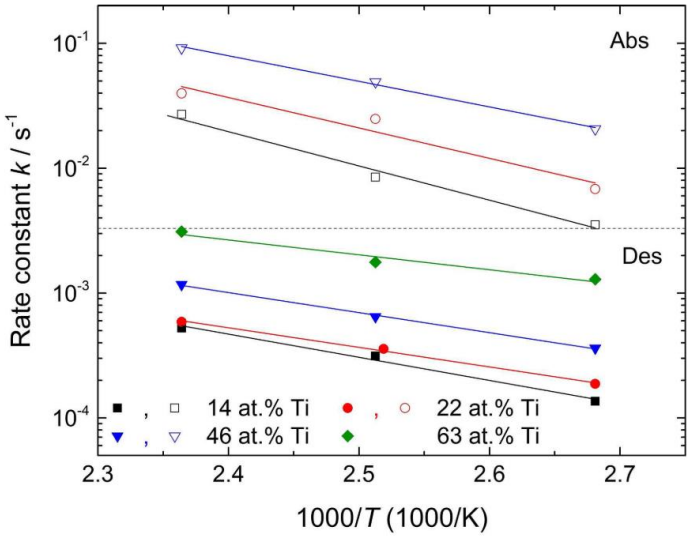

Figure 3.37. Arrhenius plot of the rate constants as obtained from the non-linear fit of the absorption (open symbols) and desorption kinetics (filled symbols).

Even if slower than absorption, the desorption kinetics (Chapter 3.6.4) are particularly interesting because they demonstrate the possibility to release hydrogen from a Mg –based material, which is both Pd –free and compatible with scale-up, in about 1–2 hours and at temperatures close to the ambient. The initial stages of the transformation appear rate-limited by H_2 recombination at the surface. We can only suggest that TiH_2 plays the role of the catalyst, but it is not possible to speculate on the precise atomistic mechanism at play. The activation energy of $31-35\ kJ/mol$ is much lower than $72\ kJ/mol$ reported for H_2 recombination using Nb_2O_5 as catalyst. Despite this low activation barrier, the rate constant k is low, about 2 orders of magnitude smaller than for absorption. This may relate to the observation that TiH_2 is distributed within the NPs and not concentrated at the surface. Another option is that the desorption mechanism is a complex one, requiring cooperative atomic motion. The possibility to lower the activation energy by a concerted motion of atoms has been demonstrated recently for hydrogen absorption at the Pd (110) surface[109].

In a purely SL process, the transformed fraction $\alpha(t)$ should be linear with time until completion. This is seldom observed in practice and the transformation rate usually decreases because other steps become rate limiting. We suggest that the initial SL desorption stage leads to the formation of a Mg shell of thickness δ at the NPs surface. Afterwards, dehydrogenation appears controlled by the displacement of the $\mathrm{Mg/MgH_2}$ interface. Using the relation (valid for spherical particles) $\alpha \approx 6\delta/d_{NP}$ and considering a half-completed transformation ($\alpha = 0.5$) and d_{NP}~$10 - 15\ \mathrm{nm}$, we can estimate that $\delta \sim 0.5 d_{NP}/6 \sim 0.8 - 1.2\ \mathrm{nm}$. Clearly, for the influence of such a thin shell to represent an observable and relevant fraction of the desorption, the particle size has to be in the nm range.

The analysis of the desorption for $\mathrm{Mg - 63Ti - H}$ sample is complicated by the overlapping of the two different kinetics previously described. It is possible that the faster rate and lower activation energy compared to lower Ti content samples are influenced by hydrogen desorption from $\mathrm{Mg_3TiH_8}$-type clusters, which are thermodynamically more stable than pure Mg [110]. However, the fact that a SL process is not observed in this sample seems consistent with the picture of ultra-fine $\mathrm{MgH_2}$ crystallites embedded within $\mathrm{TiH_2}$ NPs.

3.6.6. Final remarks on kinetics of Mg-Ti-H NPs

Each sample presented in this Chapter was subjected typically to five complete H absorption/desorption cycles in the $373 - 423\ \mathrm{K}$ range. In this time/temperature window, we did not observe significant changes in both reversible capacity and speed of the reaction. For both absorption and desorption, the transformation rate increases with increasing Ti content, while the gravimetric capacity decreases. The stability of the NPs against coarsening also improves with increasing Ti content.

The sample with $22\ \mathrm{at.\%\ Ti}$ represents a good compromise between hydrogen capacity (~$4.2\ \mathrm{wt\%}$), reaction speed, and morphological stability. Hydride formation proceeds via nucleation and growth with $n \approx 1$ with a low activation energy of $43 - 52\ \mathrm{kJ/mol}$. Hydride decomposition is initially surface-limited, except in the sample with the highest Ti content ($63\ \mathrm{at.\%\ Ti}$) where nucleation and growth prevails. The activation energy for $\mathrm{H_2}$ recombination is remarkably small (~$32\ \mathrm{kJ/mol}$ average value) and points at a new mechanism active in the low temperature, nanosized particles regime.

3.7. Results: Thermodynamics of Mg-Ti-H NPs

3.7.1. PCIs and equilibrium measurements

For some selected samples ($X_{\mathrm{Ti}} = 7, 35, 63\%$), representing the limiting values of the investigated compositional range and an intermediate value, the full PCI at $150\ ^{\circ}\mathrm{C}$ was recorded. The results are displayed in Figure 3.38 and, in a normalized scale for direct comparison, in Figure 3.39.

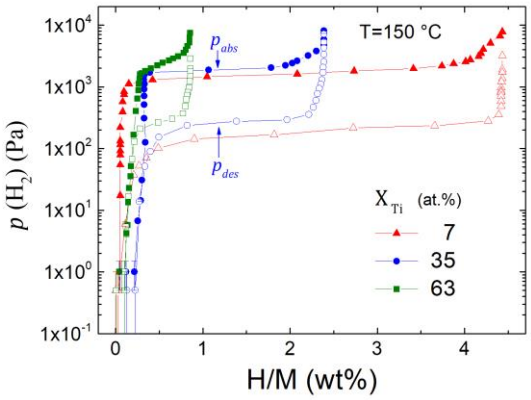

Figure 3.38. PCI curves measured for the liming and an intermediate composition $X_{\mathrm{Ti}} = 7, 35, 63$ at% Ti at temperature $T = 150°C$.

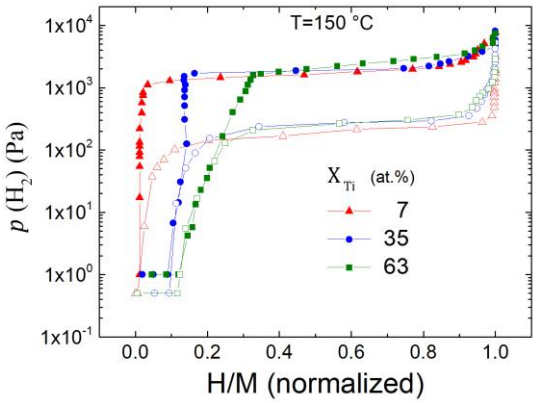

Figure 3.39. PCI curves normalized to the maximum reversible gravimetric capacity. The direct comparison highlights the presence of a second plateau for the samples with higher Ti content.

From the analysis of these PCIs, we can identify several features which depends on the composition of the $\mathrm{Mg-Ti-H}$ NPs.

1. The reversible gravimetric capacity decreases with increasing X_{Ti}. As we already pointed out comparing sorption kinetics (Chapter 3.6.3 - 3.6.4), the main contribution to $\mathrm{H_2}$ reversible exchange comes from the $\mathrm{MgH_2}$ decomposition transformation, while $\mathrm{TiH_2}$ is stable in the temperature/pressure condition of these experiments.

2. The samples with higher Ti content ($X_{\mathrm{Ti}} = 35, 63\%$) feature a second reversible plateau at pressure lower than $1\ \mathrm{Pa}$, which is the detection limit for the ceramic pressure sensor we used to characterize these materials. The relative importance of the extent of this second plateau increases with X_{Ti}, as shown by the normalized PCIs in Figure 3.39. Studies on $\mathrm{Mg_{1-y}Ti_y}$ thin films[110] revealed that

the existence of low-pressure reversible plateaux could be associated to the presence of thermodynamically more stable $\mathrm{Mg_{4-n}Ti_n}$ clusters. This is supported by the Mg solubility in $\mathrm{TiH_2}$ indicated by XRD data collected on the as-prepared samples, as discussed in Chapter 3.5.

3. The mid-plateau absorption pressure p_{abs} shifts upward with X_{Ti}. Measuring the desorption plateau is a fundamental step in claiming the true destabilization of the system[10]. In the presented experiment, the full cyclability of the sorption process in $\mathrm{Mg-Ti-H}$ NPs assure the possibility to reliably investigate the desorption plateau and the thermodynamics of the system. In particular, we can see that the mid-plateau desorption pressures p_{des} slightly shift upward with Ti content. The overall asymmetrical deviation from the bulk equilibrium pressures values indicates the presence of a thermodynamical bias that is composition dependent and increasing with X_{Ti}.

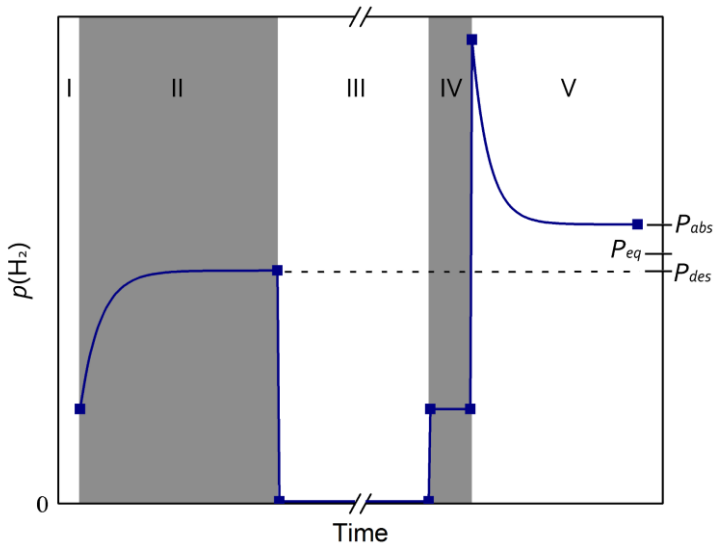

Figure 3.40. Sketch of the procedure[85] used to determine plateau pressures for hydrogen absorption and desorption. (I) The sample is heated at the desired temperature under $p(\mathrm{H_2}) \gg P_{\mathrm{eq}}$ in order to avoid desorption. (II) $p(\mathrm{H_2})$ is decreased below p_{eq}, where the desorption process begins; p_{des} is the pressure when system reaches equilibrium. (III) the sample is fully desorbed under high vacuum. (IV) A check is carried out to verify that desorption is completed. (V) $p(\mathrm{H_2})$ is raised above p_{eq}, and the system is allowed to rach equilibrium again corresponding to the p_{abs} value. The procedure is repeated to ensure that the steady state corresponds to metal hydride coexistence at equilibrium.

In agreement with the last observation, the composition dependent thermodynamics was investigated by measuring the absorption and desorption pressures for four different compositions ($X_{\mathrm{Ti}} = 14, 22, 46, 63$ at%Ti) in the $100 - 150$°C ($373 - 423$ K) temperature range following the procedure[85] sketched in Figure 3.40. This procedure was introduced to deal with the low temperature and pressure (down

to $\sim 60\ \mathrm{Pa}$) and the small driving-forces involved when the system is close to the equilibrium conditions. Furthermore, we wanted to reduce as much as possible the coarsening of the microstructure which can occur upon cycling, as we will discuss earlier in this Chapter. The results for absorption and desorption are shown in Figure 3.41 and Figure 3.42, respectively. The colored dashed lines represent the best linear fits of the experimental data. The vertical axe of the graphs is the same to highlight the small hysteresis observed between the absorption and desorption equilibrium pressures.

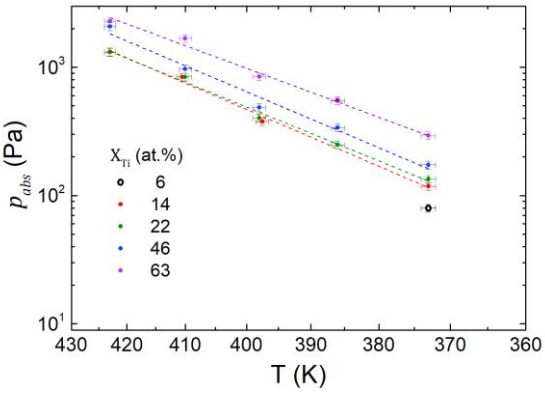

Figure 3.41. Absorption pressures for the $\mathrm{Mg-Ti-H}$ samples with different Ti content.

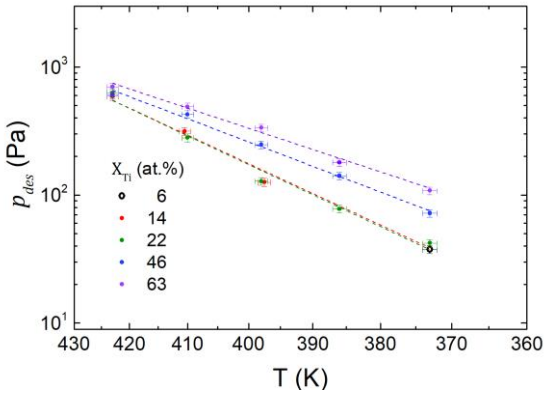

Figure 3.42. Desorption pressures for the $\mathrm{Mg-Ti-H}$ samples with different Ti content.

The Van't Hoff plots of equilibrium pressures, as determined accordingly with Equation (3.4), are reported in Figure 3.43 for the different compositions. Here the black dashed line is the extrapolation of the thermodynamics of bulk $\mathrm{MgH_2}$ starting from the $\Delta H^0_{\mathrm{bulk}} = -74.1\ \mathrm{kJ/mol}$ and $\Delta S^0_{\mathrm{bulk}} = -133.4\mathrm{J/K \cdot mol}$ values calculated at $573\ \mathrm{K}$, since no experimental data is available for the bulk system in this low temperature regime. These extrapolated results are in good accordance with the $50\ \mathrm{nm}$ unclamped Mg thin film data measured at $363\ \mathrm{K}$, supporting the validity of this assumption.

The fundamental information is that all the p_{eq} values reported in Figure 3.43 clearly lay above the bulk equilibrium pressure line, and the shift upwards with increasing Ti content, although both data and fit for $X_{\mathrm{Ti}} = 14$ and 22 at.% are nearly superposed and indistinguishable within the experimental uncertainties. The ΔS^0 and ΔH^0 values obtained from the best fit of the van't Hoff plot are represented in the inset of Figure 3.43. Albeit the large uncertainties due to the restricted temperature range investigated, the enthalpy and entropy values differs from the Mg bulk values and exhibit a decreasing trend, in absolute value, with increasing X_{Ti}.

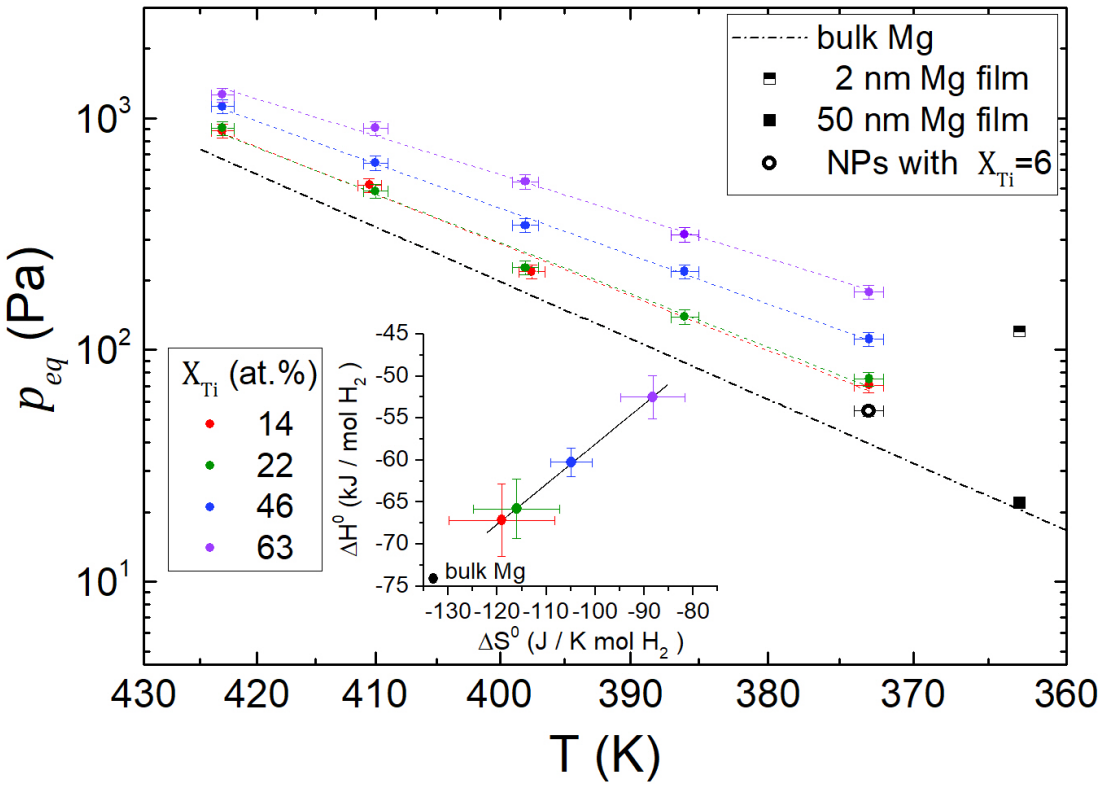

Figure 3.43. Van't Hoff plot of equilibrium pressures p_{eq} (log scale) versus T (reciprocal scale) for all the $\mathrm{Mg-Ti-H}$. The dashed black line is an extrapolation of high temperature data on bulk $\mathrm{Mg/MgH_2}$. Reference data on $\mathrm{Mg/Ti/Pd}$ nanodots[82] (a,b) and $\mathrm{Mg/Ti/Pd\ 50\ nm}$ films[66] (c) are also reported. In the inset, the corresponding ΔH and ΔS values are reported.

3.7.2. Discussion

In the previous section we saw that the thermodynamics of $\mathrm{Mg-Ti-H}$ NPs is altered with respect to bulk Mg. In this section we will discuss the possible causes for this deviation from bulk behavior.

The first possible source of destabilization is the stress generated by nanoconfinement. This hypothesis can be excluded by TEM observations of free-standing $\mathrm{Mg-Ti-H}$ NPs (see Chapter 3.5) that are relatively free to expand outward. Furthermore, the $\mathrm{Mg/Ti}$ interfaces are unlikely to be considered the source of relevant elastic constraint. These observations are also corroborated by the much smaller pressure hysteresis $p_{\mathrm{abs}}/p_{\mathrm{des}}$ measured for this system, if compared with constrained $\mathrm{Mg/Ti/Pd}$ nanodots[82] of different sizes and with $\mathrm{Mg/Ti/Pd\ 50\ nm}$ films[66], as demonstrated in Figure 3.44.

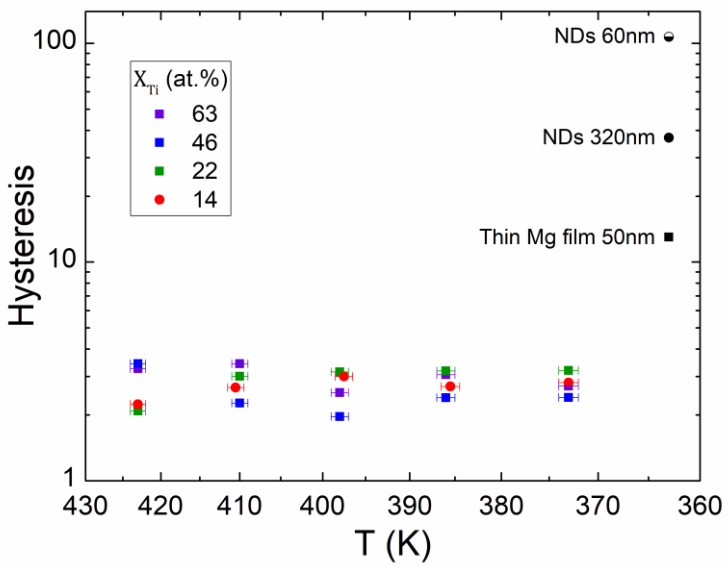

Figure 3.44. Collection of pressure hysteresis values Pabs/Pdes, as discussed for Equations (3.3)-(3.4), versus temperature measured on $\mathrm{Mg-Ti-H}$ NPs samples with Ti content $X_{\mathrm{Ti}} = 14, 22, 46, 63\ \mathrm{at\%}$. The plot reports also values recently measured on $\mathrm{Mg/Ti/Pd}$ three-layer nanodots (NDs)[82] with lateral size of 60 and 320 nm 32 and on a quasi-free Mg film 50 nm thick[66].

A second effect could be the presence of Ti atoms in solid solution within the $\mathrm{Mg/MgH_2}$ lattice. However, this case is readily excluded from XRD pattern analysis. Furthermore, we already discussed the presence of Mg in the $\mathrm{TiH_2}$ lattice and associated it with the existence for the Ti-richer samples of the secondary sorption plateau at lower pressure.

The third possible contribution comes from the total interface free energy change upon the H –sorption. According to the discussion in Chapter 3.3.3, we can estimate its contribution to the determination of a thermodynamical bias according to:

$$\delta(\Delta G^0)_{\mathrm{int}} = \frac{\bar{V}_M}{V_M}\left(\sum_i A_{MH|i}\gamma_{MH|i} - \sum_j A_{M|j}\gamma_{M|j}\right) \tag{3.15}$$

where $\gamma_{MH|i}^{int}$ and $\gamma_{M|j}^{int}$ are the interface free energy for unit area for the metal hydride and the metal. The summations are calculated over all the corresponding interface areas, named $A_{MH|i}^{int}$ and $A_{M|j}^{int}$. In the relatively simple case where the total interface area does not change after the phase transformation, the thermodynamic bias in (3.15) is directly proportional to the $\Delta\gamma_{\mathrm{TiH_2}} = \gamma_{MH|\mathrm{TiH_2}} - \gamma_{M|\mathrm{TiH_2}}$.

Based on the TEM and XRD results, we concluded that MgH_2 and TiH_2 crystallites intimately coexist within the single $Mg-Ti-H$ NPs. Taking in consideration the model system sketched in Figure 3.45, where small TiH_2 and well separated nanometric spheres are dispersed within a larger Mg/MgH_2 nanoparticle, Equation (3.15) is rewritten as:

$$\delta(\Delta G^0)_{\text{int}} = \frac{X_{\text{Ti}}}{1-X_{\text{Ti}}}\frac{6\bar{V}_{TiH_2}}{d_{TiH_2}}\Delta\gamma_{TiH_2} = A_{int}\cdot\Delta\gamma_{TiH_2} \tag{3.16}$$

where $\bar{V}_{TiH_2} = 13.30\times10^{-6}\text{m}^3$ is the molar volume of TiH_2 and the proportionality factor depends on the structure and the composition of NPs, more specifically on the Ti content X_{Ti}, and on the TiH_2 crystallite size d_{TiH_2}. This approximation reasonably describes the $Mg-Ti-H$ NPs system for low X_{Ti}, in order to avoid the contact between TiH_2 that would diminish the total interface area.

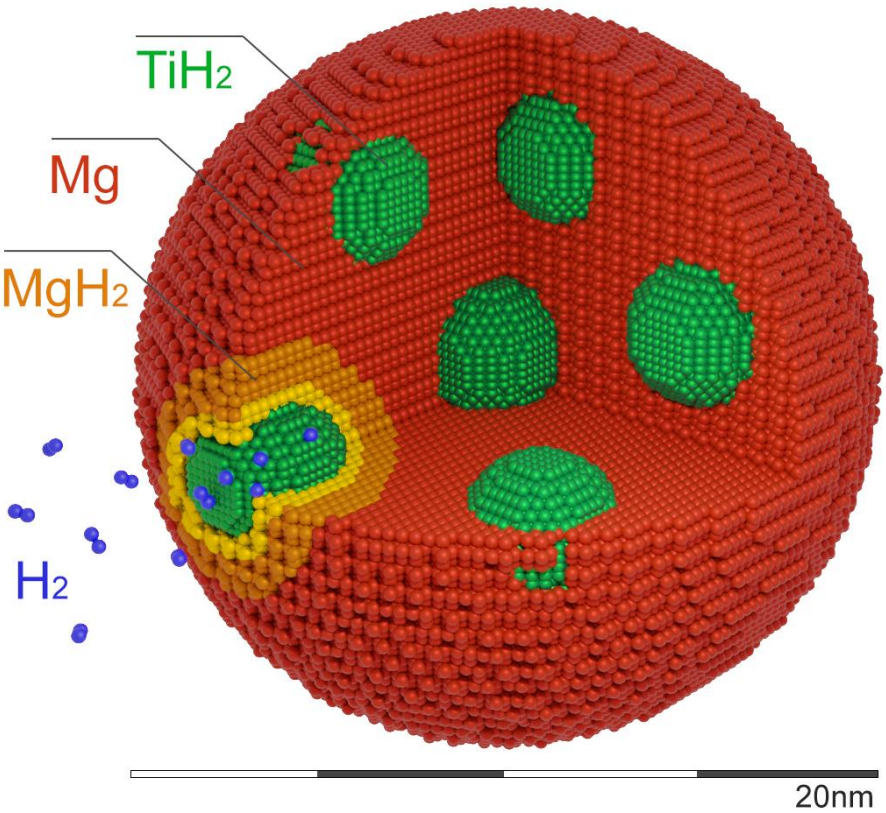

Figure 3.45. 3D model for $Mg-Ti-H$ composite NPs with low X_{Ti}; $d_{TiH_2} = 4\text{nm}$ and $d_{Mg/MgH_2} = 20\text{nm}$. are the average TiH_2 and MgH_2 crystallite size [64]. The dissociation of H_2 molecules at the surface is also represented together with the nucleation of the MgH_2hydride phase close to the interface, colored in yellow.

Exploiting the enthalpic end entropic contribution to the interface free energy:

$$\Delta\gamma_{\mathrm{TiH_2}} = \Delta h_{\mathrm{TiH_2}} - T\Delta s_{\mathrm{TiH_2}} \tag{3.17}$$

we can then separately evaluate the enthalpic and entropic contribution to the interface free energy. The substitution of (3.17) in (3.16) leads to:

$$\delta(\Delta G^0)_{\mathrm{int}} = \frac{X_{\mathrm{Ti}}}{1-X_{\mathrm{Ti}}}\frac{6\bar{V}_{\mathrm{TiH_2}}}{d_{\mathrm{TiH_2}}}\left(\Delta h_{\mathrm{TiH_2}} - T\Delta s_{\mathrm{TiH_2}}\right) = \delta(\Delta H^0)_{\mathrm{int}} - T\delta(\Delta S^0)_{\mathrm{int}} \tag{3.18}$$

Hao *et al.*[111] reported Density Functional Theory calculations of the $\mathrm{Mg|TiH_2}$ and $\mathrm{MgH_2|TiH_2}$ interface energy, yielding $\Delta h^{int}_{\mathrm{TiH_2}} = 0.59 \div 0.69\ \mathrm{J/m^2}$. Unfortunately, it is more challenging to obtain the interfacial entropy either from simulations or from experiments. The entropy has both a configurational and a vibrational term. The configurational term is due to the fraction of atom in the small (about $1\ \mathrm{nm}$ thick) interfacial region that accommodates the crystalline mismatch between different phases. According to literature[112], a rather generous estimation for this value is the one associated with the glass transition entropy, $\Delta s^{conf}_{at} \approx 1k_B/\mathrm{H}^{int}_{at}$. The vibrational entropy term is even more challenging to assess and depends critically on the nature of the interfaces. For nanocrystalline materials, an increased vibrational entropy at interfaces $\Delta s^{vib}_{at} \approx 0.2k_B/\mathrm{H}^{int}_{at}$ seems a realistic estimate[112]. It therefore appears reasonable to consider an overall entropy per interface H atom of $\Delta s_{at} = \Delta s^{conf}_{at} + \Delta s^{vib}_{at} \approx 1k_B/\mathrm{H}^{int}_{at}$. The interface-induced entropy variation per unit area Δs^{int} can then be calculated with the approximation that the volume of H atoms at the interface is the average $\langle\overline{V_{\mathrm{H}}}\rangle = 1.70\ \mathrm{cm^3/mol}$ of the corresponding volumes in $\mathrm{MgH_2}$ ($2.08\ \mathrm{cm^3/mol}$) and in $\mathrm{TiH_2}$ ($1.32\ \mathrm{cm^3/mol}$):

$$\Delta s^{int}_{\mathrm{TiH_2}} = \frac{1}{A^{int}}\frac{V^{int}}{\langle\overline{V_{\mathrm{H}}}\rangle}\Delta s_{at} = \frac{\delta^{int}\cdot\Delta s_{at}}{\langle\overline{V_H}\rangle} \tag{3.19}$$

where V^{int} and A^{int} are interface volume and area, respectively. Assuming $\delta^{int} = 1\ \mathrm{nm}$, we obtain $\Delta s^{int}_{\mathrm{TiH_2}} \approx 0.9\cdot 10^{-3}\mathrm{J/K\cdot m^2}$.

We can now apply the proposed model to the grown $\mathrm{Mg-Ti-H}$ samples, for which A_{int} can be determined starting from X_{Ti} and $d_{\mathrm{TiH_2}}$ was determined from the SEM-EDX and XRD analysis (Chapter 3.5). For the NPs with higher Ti content of 46 and 63 at.%, we have assumed a reduction of the interface area by 20 % and 25 %, respectively, to account for the impingement of $\mathrm{TiH_2}$ crystallites (this estimate is based on the analysis of the real surface of aggregates with typical 20-25% overlapping between diameters in adjacent particles, as carried out by Brasil et al[113]) and assuming 10% relative error on all calculated values of A_{int}.

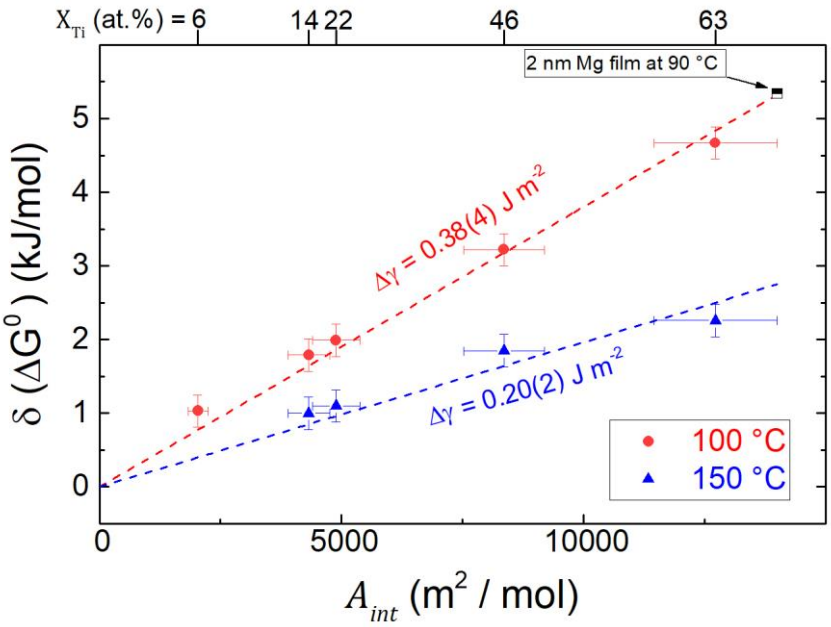

Figure 3.46. Experimentally determined thermodynamic bias $\delta\Delta G^0$ as a function of the interface area A_{int} obtained from $\mathrm{X_{Ti}}$ by means of microstructural parameters for the limiting temperatures 100°C and 150°C. The dashed lines represents the linear fit according with Equation (3.16). The interface free energy as determined from the fit is reported. As a reference, the thermodynamical bias measured for $2\ \mathrm{nm}$ thin Mg films capped with $\mathrm{TiH_2}$ is reported[66].

Figure 3.46 displays the free energy bias $\delta\Delta G^0$ evaluated starting from the equilibrium pressures according to Equation (3.6) for the boundaries of the investigated temperature range, 373 and $423\ \mathrm{K}$, as a function of the A_{int}. The thermodynamical bias decreases with increasing T. In particular, at $T = 373\ K$ and $\mathrm{X_{Ti}} = 63$ at.%, we determined $\delta\Delta G^0 \approx 4.6\ \mathrm{kJ/mol\ H_2}$, which corresponds to a pressure increase $p_{eq,nano}/p_{eq,bulk} \approx 4.5$.

From the linear fits, according to Equation (3.16), we obtain $\Delta\gamma(423\ \mathrm{K}) = (0.20 \pm 0.02)\ \mathrm{Jm^{-2}}$ and $\Delta\gamma\ (373\ \mathrm{K}) = (0.38 \pm 0.04)\ \mathrm{Jm^{-2}}$.

The interfacial free energy estimated is compatible with the $\Delta\gamma = 0.26\ \mathrm{Jm^{-2}}$ value predicted at $423\ \mathrm{K}$ considering the $\Delta h^{int}_{TiH_2} = 0.64\ \mathrm{Jm^{-2}}$ and $\Delta s^{int}_{TiH_2} = 0.9 \cdot 10^{-3}\ \mathrm{J/K \cdot m^2}$ reported in the previous discussion. DFT calculations[66,111] reports $\Delta\gamma_{TiH_2}(0\ \mathrm{K}) = \Delta h_{TiH_2} = 0.53 - 0.59\ \mathrm{Jm^{-2}}$. Mooij at al.[66] estimated the interface free energy for a $2\ \mathrm{nm}$ Mg thin films capped with TiH_2 investigated at $T = 263\ \mathrm{K}$ as $\Delta\gamma_{TiH_2}(263\ \mathrm{K}) = (0.33 \pm 0.01)\ \mathrm{Jm^{-2}}$. All these results are in good agreement with our results for $\mathrm{Mg-Ti-H}$ free-standing NPs, once considered the temperature dependent entropic contribution to the $\Delta\gamma_{TiH_2}$ in Equation (3.17), and support the interpretation that the thermodynamical bias is originated from the interface free energy difference between hydride and metal phase.

3.7.3. A remark: compensation temperature

Equation (3.18) has interesting implications on the possible presence of a unique enthalpy-entropy compensation temperature T^{comp} in nanomaterials that does not depend on microstructural parameters.

T^{comp} is the temperature at which the entropic and enthalpic biases compensate each other and all samples have the same Gibbs free energy ΔG^0_{nano} and, therefore, the same plateau pressure. The non-trivial issue about the uniqueness of T^{comp} is often source of discussions and controversies and attention should be paid while invoking it to explain measured results. It is sometimes reported in literature unexpectedly large enthalpic changes with respect to the bulk Mg system that are far beyond theoretical expectations. Some experiments[114] on $\sim 15\mathrm{nm}$ NPs investigated at $573\ \mathrm{K}$, where these materials are not stable anymore (as discussed in Chapter 3.5.2), reported a $\delta(\Delta H^0) \approx 15\ \mathrm{kJ/mol}$, even though no correspondingly large deviation from Mg bulk equilibrium pressure was observed. The authors attributed this unexpected behavior to an entropic compensation effect. However, only absorption data in a small temperature range were presented, and the presence of a large hysteresis could also explain the not-changed thermodynamics. In many cases the apparent enthalpy-entropy correlation is also explainable as phantom statistical phenomenon[112,115] associated with the limited temperature range explorable.

Starting from (3.18), valid for the free-standing $\mathrm{Mg-Ti-H}$ NPs system, we immediately observe that the enthalpy and entropy changes are proportional to the

same geometrical factor. The temperature T^{comp}, at which $\delta(\Delta H^0)_{\mathrm{int}}$ and $-T\delta(\Delta S^0)_{\mathrm{int}}$ compensate each other, is readily obtained as

$$\delta(\Delta G^0)_{\mathrm{int}} = \delta(\Delta H^0)_{\mathrm{int}} - T^{\mathrm{comp}}\delta(\Delta S^0)_{\mathrm{int}} = 0 \quad \Leftrightarrow \quad T^{\mathrm{comp}} = \frac{\Delta h_{\mathrm{TiH_2}}}{\Delta s_{\mathrm{TiH_2}}} \tag{3.20}$$

Equation (3.20) clearly indicates that T^{comp} is independent both from the composition and the geometry of the system, provided that the interface free-energy is the same for all the interfaces.

For the $\mathrm{Mg-Ti-H}$ samples, the inset in Figure 3.43 displays the best linear fit to the ΔH^0_{nano} vs ΔS^0_{nano} series obtained for samples with different X_{Ti}. Its slope represents an apparent enthalpy-entropy compensation temperature $T^{comp} = 477 \pm 5$ K. The fact that this temperature is well above the range of the measurements may point to a genuine enthalpy-entropy compensation temperature. However, in our opinion a solid proof of such a compensation would require a more accurate determination of enthalpy and entropy through measurements over a more extended temperature range

3.8. Major Results

In this Chapter, a strategy that permitted growth of a new concept of nanomaterial is presented. $\mathrm{Mg-Ti-H}$ NPs with different Ti contents by Thermal GPC by co-evaporating Mg and Ti under a $\mathrm{H_2}$-containing atmosphere. The main results are summarized in the following.

- This procedure yields ultrafine NPs (initially 7-14 nm in diameter depending on Ti content), in which Mg (or $\mathrm{MgH_2}$) and $\mathrm{TiH_2}$ coexist intimately at the single NP level, as discussed in relation to XRD and TEM structural and morphological characterization. The main features of $\mathrm{Mg-Ti-H}$ NPs nanostructure are the high density of $\mathrm{MgH_2/TiH_2}$ interfaces and the small domains size.

- The peculiar nanostructure promotes outstanding H-kinetic properties without the addition of any Pd expensive catalyst, even in the relatively mild $373-423\,\mathrm{K}$ temperature range. Both the hydrogen absorption and desorption kinetics were investigated in $373-423\,\mathrm{K}$ temperature range. In both cases, the transformation rate increases with increasing Ti content, at the expenses of the gravimetric capacity. Hydride formation proceeds via nucleation and growth with $n \approx 1$ with a low activation energy of $43–52\,\mathrm{kJ/mol}$. Hydride decomposition is initially surface-limited, except in the sample with the highest Ti content ($63\,\mathrm{at.\%\,Ti}$) where nucleation and growth prevails. The activation energy for $\mathrm{H_2}$ recombination is remarkably small ($\sim 32\,\mathrm{kJ/mol}$ average value) and points at a new mechanism active in the low temperature, nanosized particles regime.

- The remarkably fast desorption kinetics allowed also to explore the thermodynamics in the $373-423\,\mathrm{K}$ temperature range. A thermodynamical bias was $\delta\Delta G^0$ was experimentally determined. $\delta\Delta G^0$ decreases with increasing T. In particular, at $T = 373\,K$ and $\mathrm{X_{Ti}} = 63$ at.%, we determined $\delta\Delta G^0 \approx 4.6\,\mathrm{kJ/mol\,H_2}$, which corresponds to a pressure increase $p_{eq,nano}/p_{eq,bulk} \approx 4.5$. However, this thermodynamic alteration comes at the cost of a reduced gravimetric capacity linked with the high weight fraction of $\mathrm{TiH_2}$.

- The effect of the $\mathrm{MgH_2/TiH_2}$ interfacial free energy on the thermodynamics of hydrogen sorption in $\mathrm{Mg-Ti-H}$ NPs was discussed in the framework of a

thermodynamical model that allowed to determine an interface free energy interfacial free energy difference $\Delta\gamma = 0.40(4)$ and $0.20(2)\ \mathrm{Jm}^{-2}$ at $T = 100$ and 150 °C respectively. This result is in good agreement with DFT predictions and other experimental values reported in literature.

- The van 't Hoff analysis and the temperature dependence of $\delta\Delta G^0$ suggest that $\Delta\gamma$ contains an enthalpic and an entropic contribution, the latter partly compensating the destabilization induced by the former. Therefore, further advances in destabilization of $\mathrm{MgH_2}$ nanostructures would certainly benefit from a progress in the modelling and engineering of the interfacial entropy.

In summary, this work proves that properly designed nanostructures can significantly stretch the temperature / pressure window for fast Mg-based hydrogen sorption toward ambient conditions.

Chapter 4.

Fe-Co nanoparticles for catalysis

Since the development of metallurgy in ancient times, a way to tailor physical properties of materials is to combine metals into alloys. This concept has been applied also in nanoscience to grow nanoalloy materials with tailorable properties depending also on composition rather than only on size. Additional enriching degree of freedom can arise with the formation surface structures and segregation properties of this class of materials[116,117] that are important in determining chemical reactivity and especially catalytic activity.

Nanoalloys can also feature unique structures depending also on the synthesis method[118,119]. Figure 4.1 illustrates some archetypal patterns possible in binary nano-alloys[120] and differing on chemical ordering: core-shell, three shell and Janus structures exhibit element segregation, but also the formation of random or ordered alloys is possible[7].

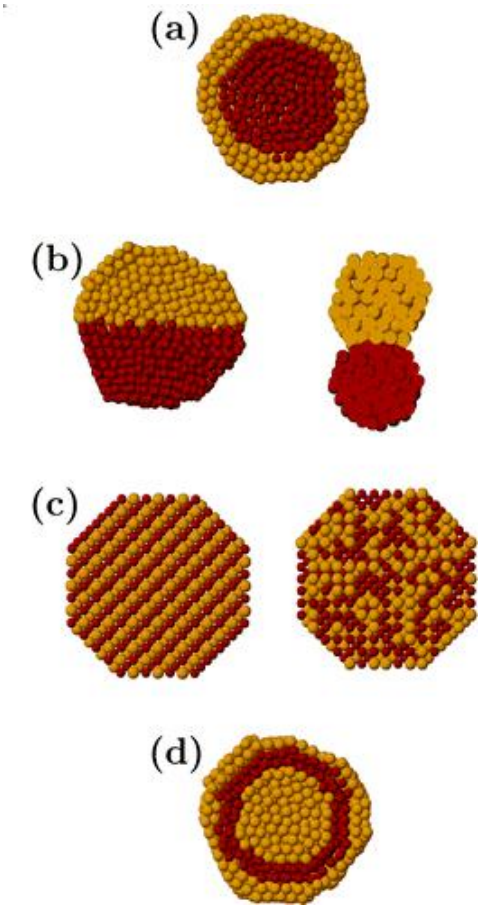

Figure 4.1. Some archetypal mixing pattern for bimetallic alloys: (a) core/shell, (b) Janus structure and segregation (c) ordered and random alloys and (d) three shell structure. Image taken from Ferrando et al. [108]

In this chapter, the $Fe-Co$ system was selected as a case of study. $Fe-Co$ nanoalloys are of great interest in many fields such as magnetism[121,122], drug delivery[123], MRI contrast enhancement[124] and catalysis[125].

In the case of this work, Fe and Co were selected mainly because the difference of saturation vapor pressure and surface tension between the two elements are comparable[126]. This requirement is important for the stoichiometry of a precursor alloy to be respected during the evaporation in the case of Thermal GPC. Pulsed Laser GPC was also employed to grow $Fe-Co$ NPs and the results obtained are compared. Finally, a possible field of application, the role in the catalysis of CO_2 reduction using hydrogen is selected and preliminary catalytic tests results are shown.

4.1. Fe-Co via IGC

4.1.1. Experimental setup

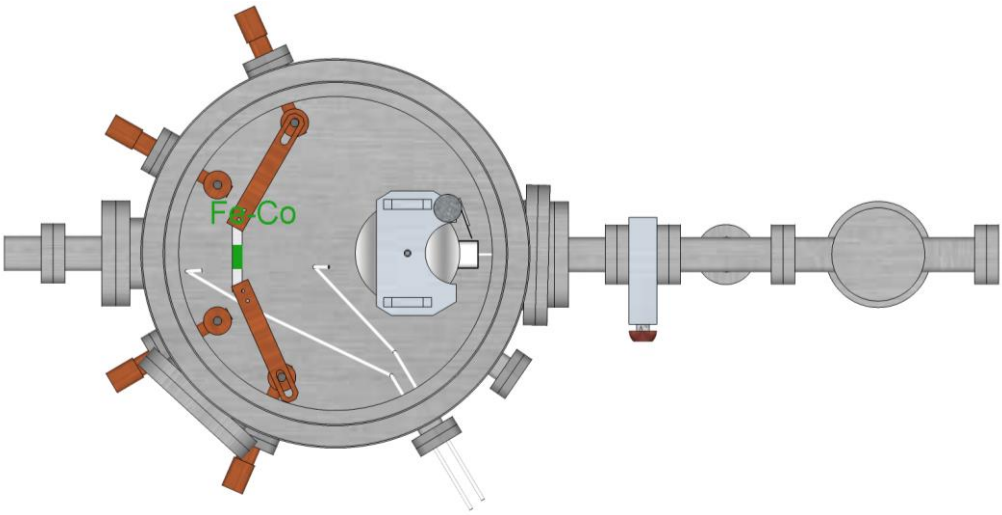

Figure 4.2. Setup of the Thermal GPC apparatus for the growth of the of Fe-Co NPs.

A top view of the RIGC setup for the growth of Fe-Co NPs (NCs) is portraited in Figure 4.2. During the synthesis, He (99.9996% purity) is fed into the chamber. The powders are melted under high vacuum and rapidly cooled to about 1000 °C in order to homogenize the alloy precursor. Four samples with composition $\mathrm{Fe}_{100-x} - \mathrm{Co}_x$ (with $x = 0, 23, 48, 68$ at. %) were prepared. Table 4.1 lists the Fe and Co content of all as-prepared NPs as determined from EDX analysis.

Table 4.1. Fe – Co alloy NPs. Comparison between the composition of the precursor powder mixture and of the synthesized NPs. The samples names reflect the NPs composition as determined by SEM-EDX.

Sample	Fe – Co precursor		Fe – Co NPs	
	Fe (at%)	Co (at%)	Fe (at%)	Co (at%)
Fe_{100}	100	-	100	-
$Fe_{77}Co_{23}$	76(1)	24(1)	77(1)	23(1)
$Fe_{52}Co_{48}$	51(1)	49(1)	52(1)	48(1)
$Fe_{32}Co_{68}$	27(1)	73(1)	32(1)	68(1)

We notice that the NPs composition is compatible (within the uncertainties) with the precursor composition for all samples but the Co-richest one. For the Fe – Co system, the stoichiometry can be quite well preserved because Fe and Co have similar vapor pressures. Nevertheless, the slightly higher evaporation rate of Fe [127] can be the reason for the small increase in the Fe content, as shown in Table 4.1 for the Co-richest sample. This effect could have an important impact over the homogeneity of samples

obtained with prolonged evaporation, due to the progressive decreasing content ratio of the element with higher evaporation rate in the precursor alloy.

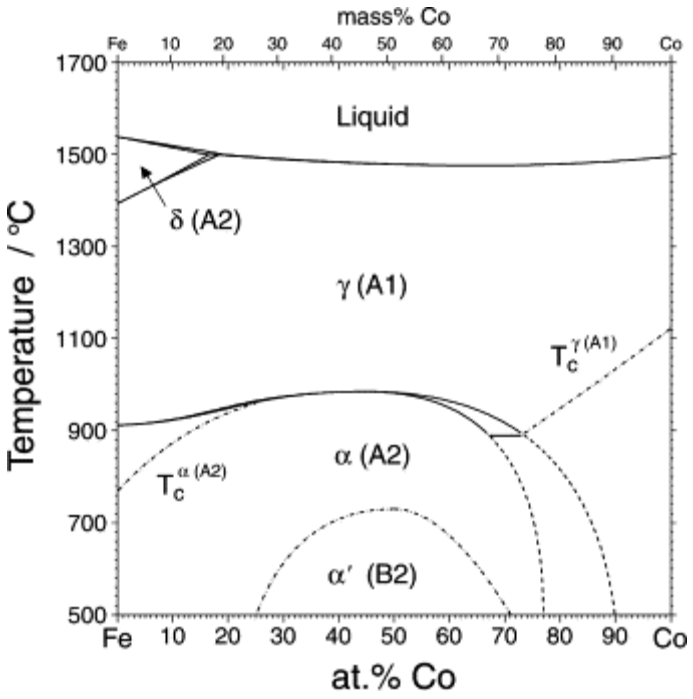

Figure 4.3. Phase diagram for the $\mathrm{Fe-Co}$ binary system. Image taken from Ohnuma et al[128].

4.1.2. Structural Characterization

The crystalline structure of the $\mathrm{Fe-Co}$ alloy nanoparticles has been investigated with a Bragg-Brentano *PANalytical X'celerator* diffractometer employing a $\mathrm{Cu\ K_\alpha}$ radiation ($\lambda_{K_a} = 1.54050\ \text{Å}$). The X-ray Diffraction (XRD) patterns have been analyzed using the MAUD Rietveld refinement software[88].

Table 4.2. Crystallite size d and lattice parameter a of the three crystalline phases identified by XRD in Fe-Co NPs. The FCC γ-phase is only observed at the highest Co content.

Sample	α-Fe-Co		Cobalt ferrite		γ-Fe-Co	
	d[nm]	*a*[Å]	*d*[nm]	*a*[Å]	*d*[nm]	*a*[Å]
Fe	15 (1)	2.8729(4)	2.0(2)	8.451(6)	-	-
$Fe_{77}Co_{23}$	19 (2)	2.8686(2)	2.7(2)	8.4272(6)	-	-
$Fe_{52}Co_{48}$	18 (2)	2.8629(1)	2.4(2)	8.442(4)	-	-
$Fe_{32}Co_{68}$	24 (2)	2.8406(2)	n.d.	n.d.	10 (2)	3.564(2)

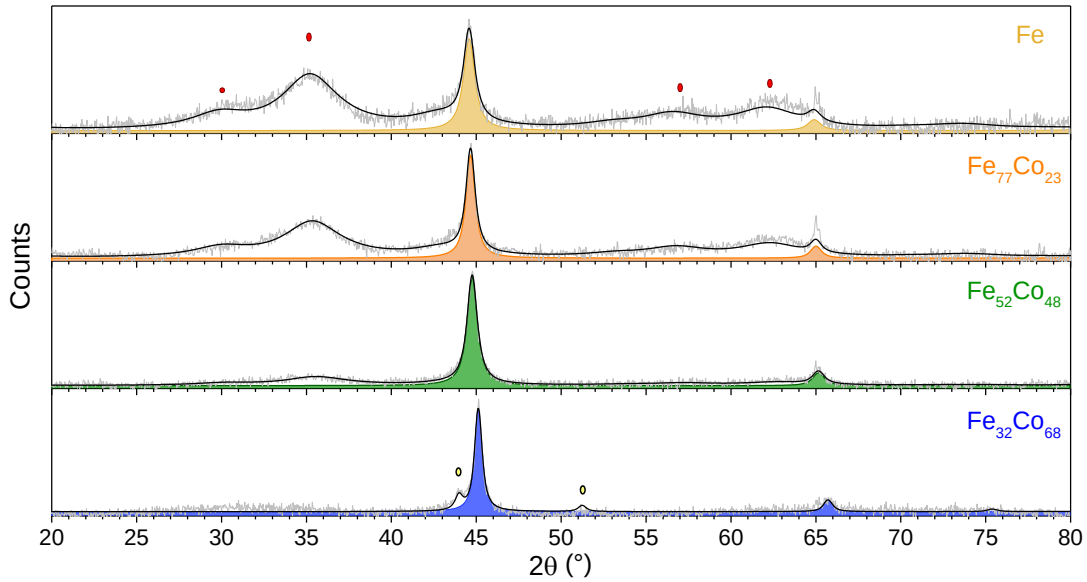

Figure 4.4. XRD patterns of $Fe_{100-x}Co_x$ samples ($x = 100, 77, 52, 32$ from top to bottom). Grey lines represent experimental data, while the black solid lines are the best fits. The main phase detected is the BCC FeCo alloy and the correspondent contribution to the XRD pattern is given by the colored areas. The Bragg reflections of cobalt ferrite (red circles) and FCC Fe-Co alloy (black hollow circles) are reported.

Figure 4.4 displays the XRD patterns of the as-prepared $Fe_{100-x} - Co_x$ NPs. The mean crystallite size d and lattice parameter of all identified phases are reported in Table 4.2. The main phase observed is the BCC $Fe - Co$ α −phase: the colored areas are the contribution to the XRD patterns and the (110) and (200) Bragg reflections are distinguishable.

The (111) and (200) Bragg reflections of the $Fe - Co$ FCC γ −phase are additionally detected only in the Co-richest sample ($Fe_{32}Co_{68}$). According to the $Fe - Co$ phase diagram[129] in Figure 4.3, Fe and Co are completely miscible at room temperature up to 72 at.% Co content forming a BCC α −phase, while FCC and BCC phases coexist at higher Co content (72 to 92 at.% Co). Here we observe the FCC γ −phase already at 68 at.% Co. This deviation with respect to the bulk phase diagram, in nanoalloy systems is due to the increase in relative magnitude of surface energy and is size-dependent[118]. FCC and BCC coexistence in $Fe - Co$ nanoalloys has already been reported above 42 at.% Co for 15 nm NPs synthetized by chemical vapor condensation[130].

The shift of the $\alpha -$ $FeCo$ reflections towards higher angles with the increasing Co content reflects in the shrinking of the cell parameter a (Table 4.2), which is consistent with the smaller atomic radius of Co with respect to Fe.

A magnetite-like spinel structure is also spotted, featuring broader diffraction peaks corresponding with an ultrafine crystallite average size of $2 - 3$ nm. This oxide

forms when the NPs get in contact with the ambient air for XRD measurements. If air exposure is fast, the NPs begin to glow and oxidize completely. Conversely, if the exposure is sufficiently slow, as in this case where air flows into the sample holder gradually in about one hour, full oxidation can be avoided through the formation of a protective oxide shell[22,131]. The intensity of the oxide broad peaks in Figure 5a shows that the oxidation resistance upon air exposure augments with increasing Co content. A remarkable stability against oxidation was also reported for $\mathrm{Fe}_{100-x} - \mathrm{Co}_x$ NPs with $x \approx 40-50$ prepared by hydrothermal synthesis[132].

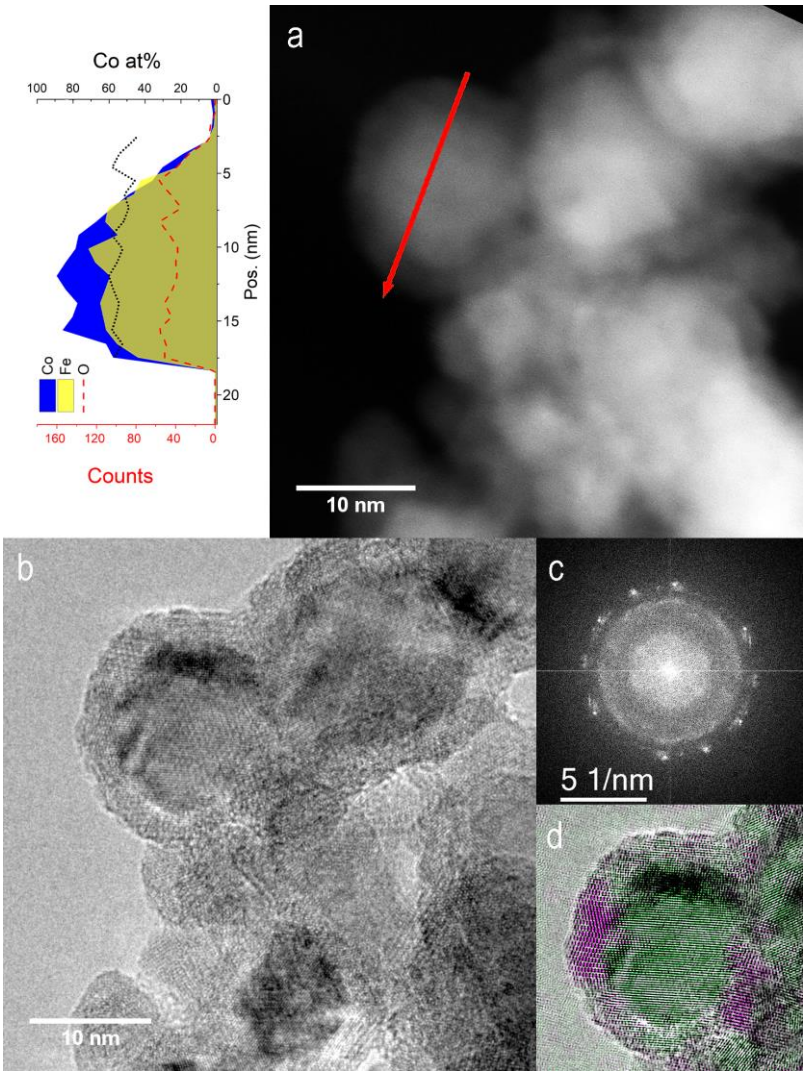

Figure 4.5. TEM analysis of $\mathrm{Fe}_{52}\mathrm{Co}_{48}$ NPs. (a) HAADF-STEM image and the corresponding EDX profile taken along the red arrow. The blue and yellow areas and the red dashed line represent Co, Fe and O X-ray fluorescence counts. The black solid line is the $\mathrm{Co}/(\mathrm{Co}+\mathrm{Fe})$ atomic ratio within the NP; (b) HR-TEM image of the same area together with its (c) Fast-Fourier-Transform (FFT); (d) Mapping of crystal phases obtained from the analysis of planar spacing. $\alpha - \mathrm{FeCo}$ (110) and cobalt ferrite (311) planes are represented in green and purple, respectively.

The High Angle Annular Dark Field (HAADF) STEM image in Figure 4.7a shows a detail of $\mathrm{Fe_{52}Co_{48}}$ sample. The NPs are surrounded by a lower contrast shell about 3 nm thick. This is a first indication in favor of the oxide nature of the shell.

In fact, the contrast in incoherent HAADF-STEM images is proportional to $tZ^{1.7}$, where t is the thickness and Z is the average atomic number. Further information on the composition of the shell is provided by the STEM-EDX profile in Figure 4.6a. The lower contrast shell corresponds to the regions, in which the Co and Fe fluorescence counts (blue and yellow areas) start to decrease while the O counts remain unvaried (red dashed line). Interestingly, the $\mathrm{Co}/(\mathrm{Co}+\mathrm{Fe})$ atomic ratio (black solid line) is similar in the core and the shell. This result demonstrates that the oxide is actually a cobalt ferrite $(\mathrm{Fe_{100-x}Co_x})_3\mathrm{O_4}$ with a magnetite-like spinel structure[133] and a $\mathrm{Co/Fe}$ ratio similar to that of the core.

The HR-TEM image of the same NPs in Figure 4.5b highlights the atomic-level structure of core and shell regions. The Fast Fourier Transform (FFT) operated over the HR-TEM image is displayed in Figure 4.5c. The bright spots correspond to $\alpha-\mathrm{FeCo}$ (110) planes, while the inner broad ring is due to the (311) crystalline planes of cobalt ferrite. These contributions can be separated by applying a filter to the FFT image followed by an inverse transformation. In this way, one obtains two separate images for the lattice planes of the two phases. In Figure 4.5d, the separate images are superposed in false colors to the HR-TEM image. The $\alpha-\mathrm{FeCo}$ lattice planes (green) are clearly visible in the core, while the cobalt ferrite planes (violet) belong to the shell.

Similar observation applies to all the samples, as shown in the STEM-EDX collection reported in Figure 4.6. The intensity of the oxide broad peaks shows an increasing oxidation resistance upon air exposure augments with increasing Co content. A remarkable stability against oxidation was also reported for $\mathrm{Fe_{100-x}Co_x}$ NPs with $x \approx 40-50$ prepared by hydrothermal synthesis[134].

The TEM images in Figure 4.7 displays the morphology of the as preprared FeCo samples. A certain degree of agglomeration between the NPs is inherent in the synthesis method and some of them appears to be welded, however they can be individually distinguished. The size of the nanoparticles is distributed lognormally, as typical of the inert gas condensation technique[135], with a mean size of 12 nm ($\mathrm{Fe_{77}Co_{23}}$).), 10 nm ($\mathrm{Fe_{52}Co_{48}}$).) and 13 nm ($\mathrm{Fe_{32}Co_{68}}$) and half of the measured particles reside in the 8-16 nm size range for all the compositions.

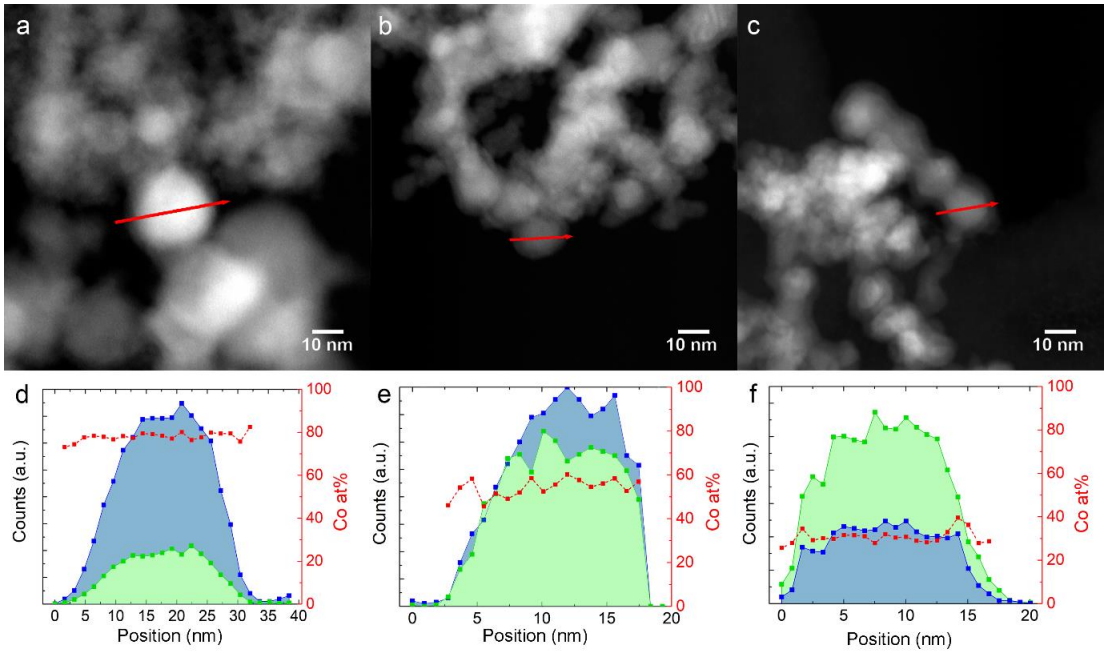

Figure 4.6. **Fe** and **Co** EDX signals alongside the red arrow showed in the STEM image above them. a, d: $Fe_{32}Co_{68}$; b, e: $Fe_{52}Co_{48}$;; c, f: $Fe_{77}Co_{23}$;.The blue and green profile represents Co and Fe counts, respectively. Red spots represent the calculated Co atomic content.

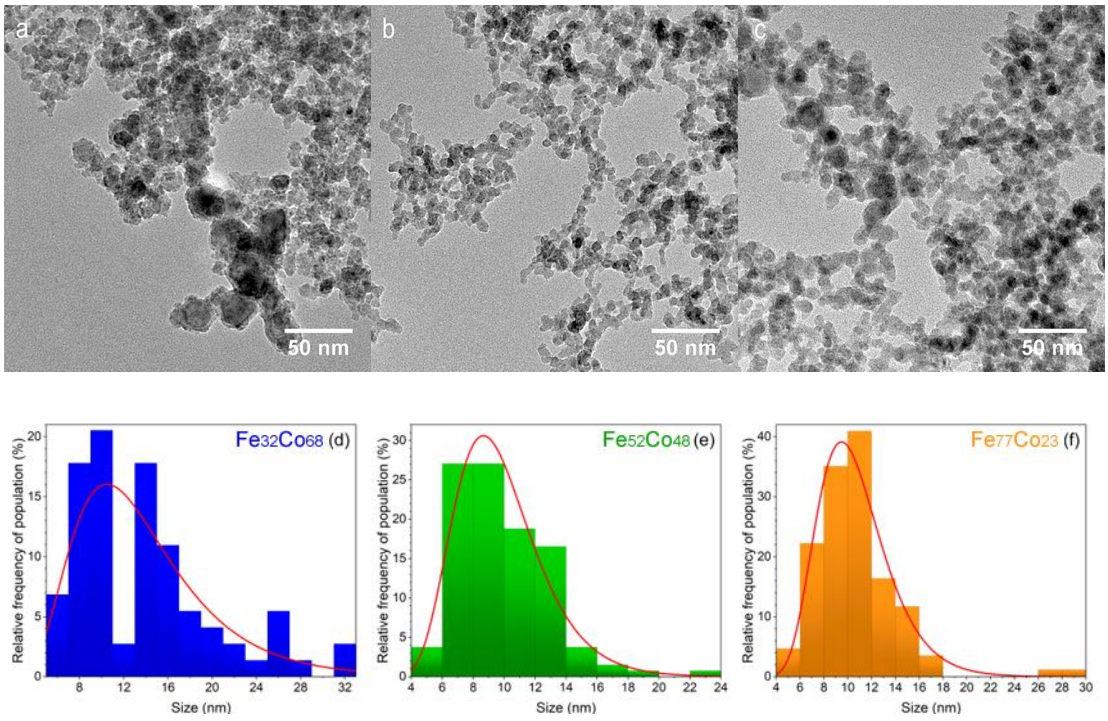

Figure 4.7. Fe and Co EDX signals alongside the red arrow showed in the STEM image above them. a, d: $Fe_{32}Co_{68}$; b, e: $Fe_{52}Co_{48}$; c, f: $Fe_{77}Co_{23}$.The blue and green profile represents Co and Fe counts, respectively. Red spots represent the calculated Co atomic content.

4.2. Fe-Co via PLIGC

4.2.1. Description of the technique

Metal NPs were synthetized with the Pulsed Laser Inert Gas Condensation apparatus. A photo of the actual experimental setup is shown in Figure 4.8.

Three $\mathrm{Fe}-\mathrm{Co}$ alloy precursor targets (*EvoChem Gmbh* 2" diameter, $3\ \mathrm{mm}$ thickness 99.95% purity) with different elemental composition were ablated by scanning the surface with a *TruMicro 5050* pico-second $\mathrm{Nd{:}YAG}$ ($\lambda = 1064\ \mathrm{nm}$) pulsed laser irradiation (maximum power $50\mathrm{W}$, max pulse energy $250\ \mu\mathrm{J}$) operated at in a ultra high vacuum chamber (base pressure $10^{-5}\mathrm{Pa}$).The laser was operated at $800\ \mathrm{kHz}$.

The chamber was preliminary evacuated to $10^{-5}\ \mathrm{Pa}$ to avoid oxygen contamination during the synthesis process. During the NPs growth stage, the overall pressure was monitored by an *Atmion Wide Range Manometer* that combines a Pirani gauge with a Bayard-Alpert ion gauge, positioned close to the target. The pressure was dynamically maintained by active pumping the system with a *Pfeiffer OnTool Booster 150* pump and regulating the pumped gas flux using a throttle valve driven by a feedback loop control unit. Concerning this Thesis, the growth pressure was selected only in the $500 \div 2000\ \mathrm{Pa}$ range.

The NPs condensed from the plume are rapidly removed from the laser-irradiated zone by the incoming He gas flow and transported towards a liquid nitrogen cooled collection device.

After the growth step, the collection unit is sealed by using gate valves under a slight Ar overpressure. The as-synthetized nanoparticles are finally scraped off the collecting surface inside a glovebox, avoiding air exposure.

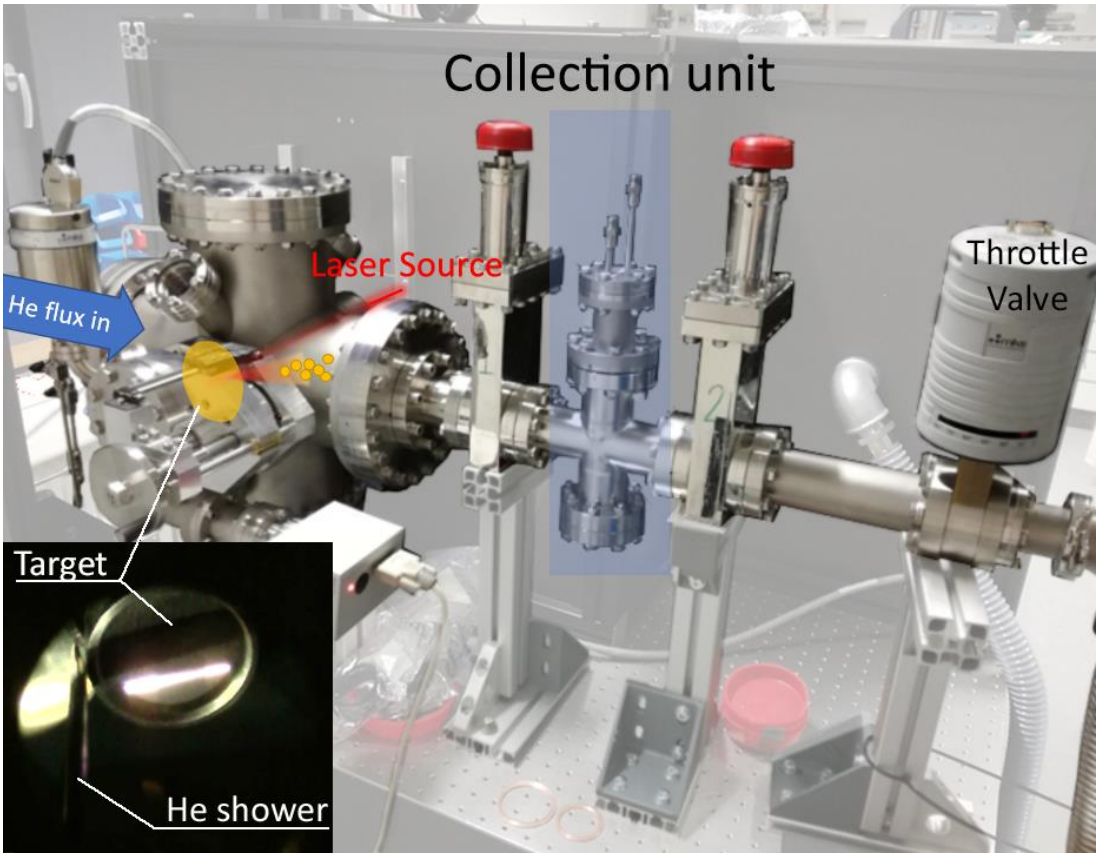

Figure 4.8. PLIGC system. The laser path is indicated with the red line and the position of the ablation target is indicated with a yellow ellipse. In the inset, an photo of the target acquired during the laser scanning. The He inlet shower is shown

4.2.2. Preliminary tests

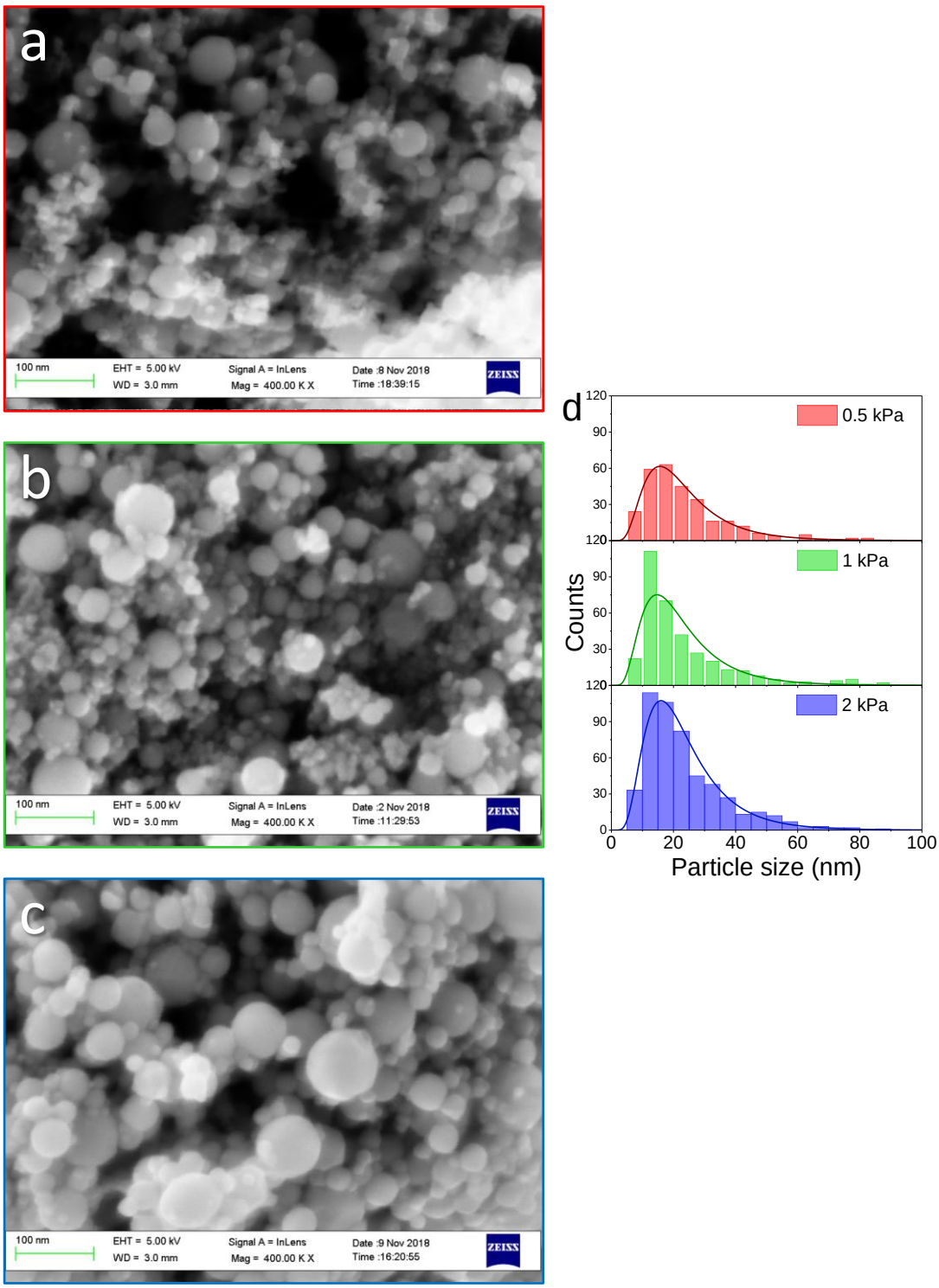

Figure 4.9. FE-SEM In-lens images of the FeCo NPs and the correspondent size distribution as obtained by varying the He gas pressure p(He)=0.5 kPa, 1 kPa, 2 kPa from the top to the bottom, respectively. The laser power P=20W was the same for the set of experiments.

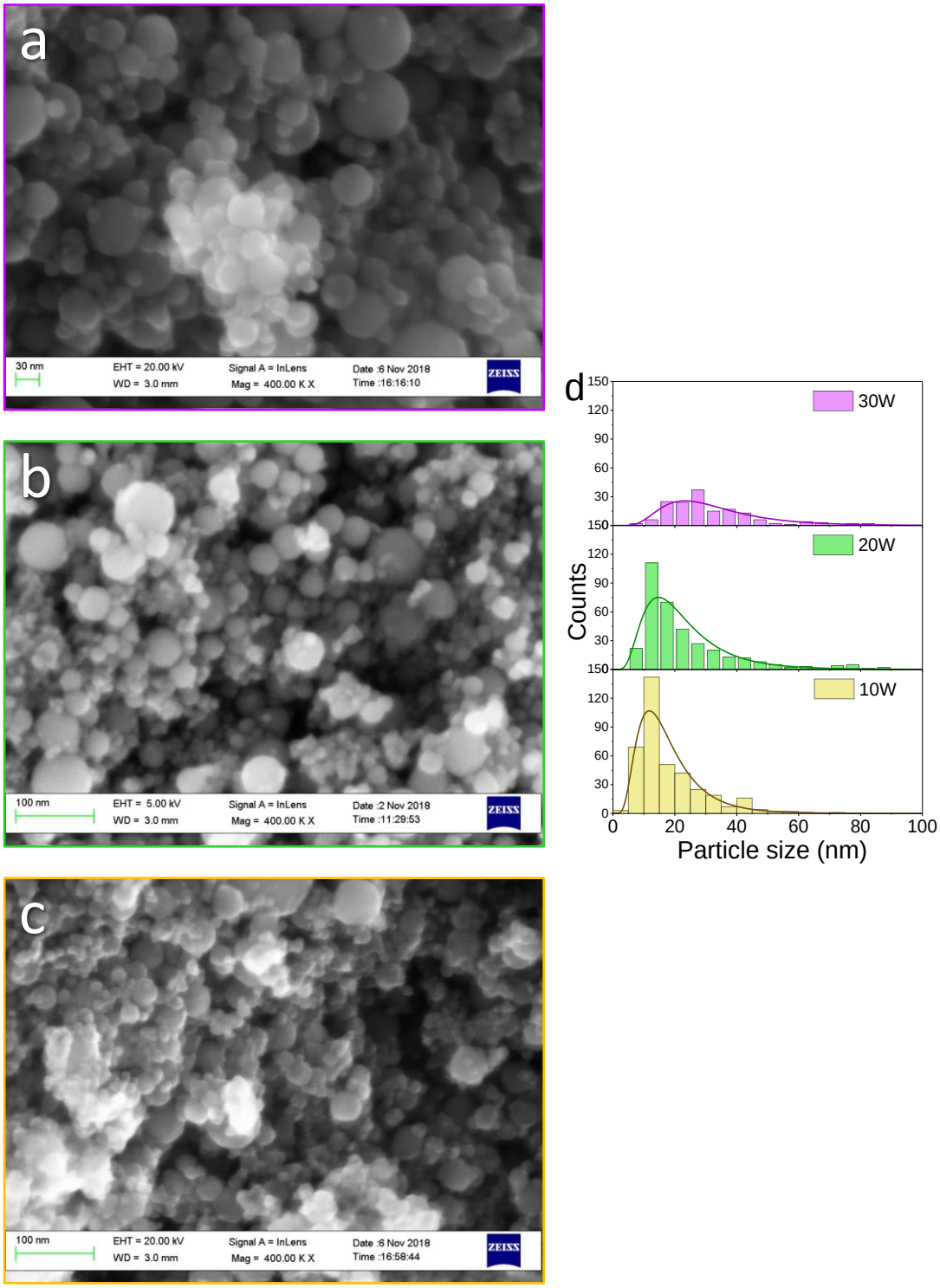

Figure 4.10. FE-SEM In-lens images of the FeCo NPs and the correspondent size distribution as obtained by varying the laser power (P=30W, 20W, 10W from the top to the bottom, respectively) and keeping constant the p(He)=1kPa.

The synthesis apparatus was preliminarily tested in order to find the experimental parameters (laser focus, target positioning, He gas pressure and laser power) that guaranteed the optimal growth yield (estimated in mg/hour) and

nanoparticle size distribution. A Fe target (*SurfaceNet Gmbh,* 99.95% purity) was employed in during this testing procedure. The morphology of nanoparticles, the size distribution and the average elemental composition of the nanoparticles were characterized using a *Zeiss Leo Gemini 1530* field emission scanning electron microscope equipped with an EDX detector.

Two sets of samples grown by varying either the He pressure or the power of the laser are reported together with the size distribution in Figure 4.9 and Figure 4.10, respectively. The size of the grown NPs is lognormally distributed. If the laser power is kept constant to $20\,\mathrm{W}$, the variation of the He pressure ($0.5\,\mathrm{kPa}$, $1\,\mathrm{kPa}$ and $2\,\mathrm{kPa}$, reported in Figure 4.9a-b-c, respectively) has almost no influence on the average NPs size, while the yield increases with the He pressure. In fact, when operating at lower pressures, the NPs stick to the inner walls, partially coating the window that allows the laser to access the chamber, resulting in a loss of power and potential hazardous heating of the window itself. This explains the decrease of the yield with decreasing He gas pressure. On the other hand, by increasing the laser power at constant pressure $p(\mathrm{He}) = 1\mathrm{kPa}$ (Figure 4.10a-b-c) we obtain larger average NPs size and broader size distributions, but the yield is ~ 2 orders of magnitude lower when the laser is operated at $\mathrm{P} = 10\mathrm{W}$ compared to $20\mathrm{W}$.

As a trade-off condition, all the following $\mathrm{Fe} - \mathrm{Co}$ NPs samples were synthetized under the same conditions by irradiating the metal target with the $\mathrm{Nd{:}YAG}$ laser operated at $\mathrm{P} = 20\mathrm{W}$ in a $\mathrm{p(He)} = 1\mathrm{kPa}$ atmosphere for 1 hour. Both the yield (~200mg/hour) and the average size of the synthetized samples were not significantly affected by varying the $\mathrm{Fe/Co}$ ratio. The EDX elemental composition both of the targets and of the as-prepared samples are reported in Table 4.3. No relevant difference was detected in the $\mathrm{Fe/Co}$ atomic ratio of the sample and the correspondent precursor target. The homogeneity of the latter was also verified by scanning it along the whole diameter.

These measurements confirm the enormous potentiality of this technique that allows to synthetize large quantities of nanoparticles, if compared to the conventional thermal and sputtering GPC, in a reasonable time-scale and maintaining the stoichiometry of the precursor alloy. In the following, the grown samples will be labeled according to the Fe atomic content determined by EDX as $\mathrm{Fe}_{100-x}\mathrm{Co}_x$.

Table 4.3. Comparison between the composition of the precursor powder mixture and of the Fe-Co alloy NPs synthetized via Pulsed Laser GPC. The samples names reflect the NPs composition as determined by SEM-EDX.

Sample	$Fe-Co$ Target		$Fe-Co$ NPs	
	Fe (at%)	Co (at%)	Fe (at%)	Co (at%)
$Fe_{30}Co_{70}$	29.8(1)	70.2(5)	29.5(5)	70.2(1)
$Fe_{51}Co_{49}$	50.6(1)	49.4(5)	50.7(2)	49.3(2)
$Fe_{77}Co_{24}$			76.6(2)	24.4(1)-

4.2.3. Structural Characterization

The crystalline structure of the $Fe-Co$ alloy nanoparticles grown by Pulsed Laser-GPC has been investigated with a Bragg-Brentano *Bruker* diffractometer employing a liquid Ga jet as anode ($\lambda_{K_\beta} = 1.20759$ Å). The sample was loaded on the XRD stage inside a glovebox and a Kapton tape was used to prevent air exposure.

In Figure 4.12, the XRD patterns of the $Fe_{1-x}Co_x$ samples is displayed. For all of the samples, the only crystalline phase detected is BCC $Fe-Co$ α −phase, accordingly with the $Fe-Co$ phase diagram that predict complete miscibility of the two elements up to 72 at.$\%$ Co content. The Bragg reflections shift towards higher angles with increasing Co content. This corresponds to the shrinking of the lattice parameter a, as reported in Table 4.4, and is consistent with the smaller atomic radius of Co with respect to Fe. No oxide phase is spotted in the XRD patterns. The narrow Bragg reflection observed indicates that large crystallites are present within the material, however no straightforward conclusion on the possible influence of Co content on the average crystallite size can be drawn from XRD analysis.

Table 4.4. Lattice parameter a of the $Fe-Co$ BCC phase spotted in the XRD pattern of Fe-Co NPs. The average particle size obtained by STEM analysis $< d_{NP} >$ and the scale sigma parameter of the normally distributed quantity $\ln(d_{NP})$ are also reported.

Sample	$Fe-Co$ BCC	Particle size distribution (TEM)	
	a (Å)	$< d_{NP} >$	scale sigma
$Fe_{75}Co_{25}$	2.86612(2)	22	0.52
$Fe_{50}Co_{50}$	2.85351(3)	21	0.60
$Fe_{30}Co_{70}$	2.84062(2)	18	0.50

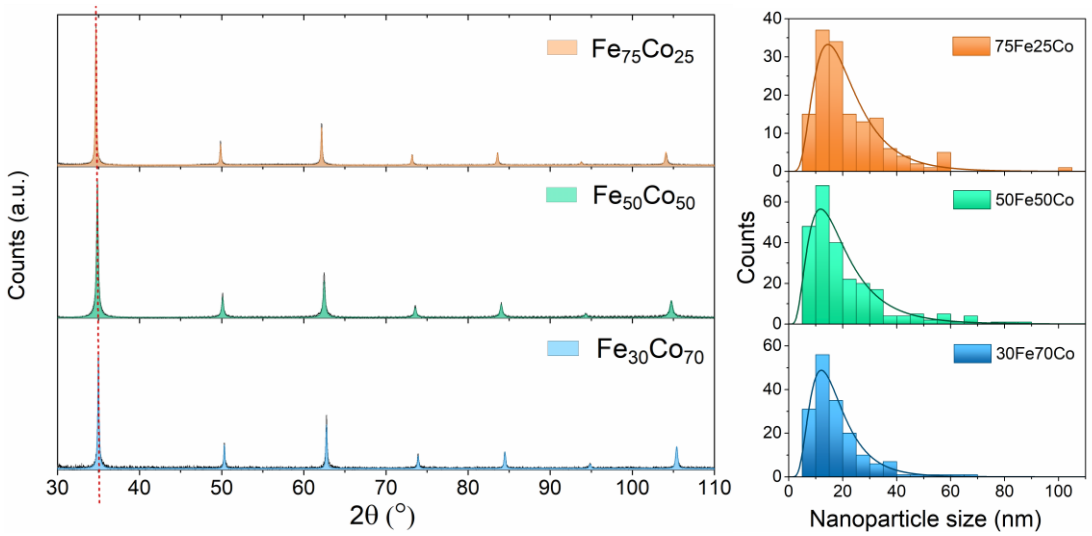

Figure 4.11. XRD patterns of $Fe_{100-x}Co_x$. The black solid lines are the experimental data,Experimental data. The BCC FeCo alloy contribution to the XRD pattern is given by the colored areas. The Bragg reflections of BCC $FeCo$ shift towards higher angles with increasing Co content, as highlighted by the red dashed line.

For the characterization at the single NP level, a *FEI Titan 80-300* Transmission Electron Microscope equipped with a spherical aberration corrector, a *Gatan Tridiem* image filter for the collection of energy-filtered TEM images (EFTEM) was employed. The TEM was operated at 300keV accelerating voltage for the HRTEM imaging, and in nanoprobe mode for HAADF-STEM, EFTEM and EELS spectra acquisition. The samples were prepared by directly dispersing the powder onto gold grid coated with a holey carbon film.

The NPs size distribution as determined from STEM images analysis are reported in Figure 4.11 The NPs sizes follow a log-normal distribution, typical of other GPC techniques[19]. The average NP size $< d_{NP} >$ spans from 18 to 22 nm, and half of the measured particles reside in the $11-30$ nm size range for all the Fe/Co compositions. However, many large particles with $d{\sim}60-80$nm are detected. No significative difference was observed in the particle sizes depending on Fe/Co ratio. This could be related to the almost identical surface tension and vapor pressure of Fe and Co. Therefore, Fe and Co should behave very similarly in the plasma plume and the condensation and coagulation of the two elements occurs equally[126].

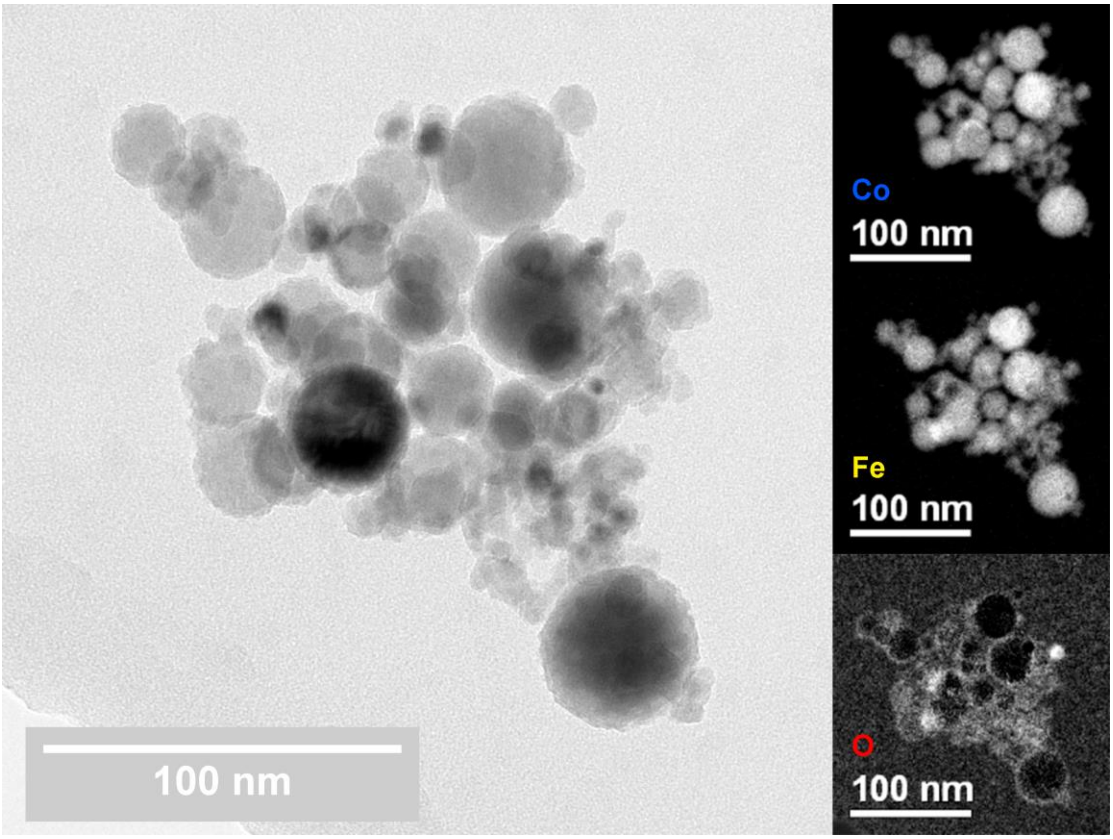

Figure 4.12 EFTEM "zero/loss" image representative of the $Fe_{30}Co_{70}$ sample. The Fe, Co and O elemental distribution maps are reported.

Figure 4.12 shows a typical EFTEM analysis performed for the $Fe_{30}Co_{70}$ sample. In EFTEM[136], electrons with an energy loss characteristic of an atomic energy level are selected by a magnetic prism coupled with a filter and used to reconstruct semi-quantitative elemental distribution maps with nanometer resolution[137].

Co, Fe and O elemental maps are displayed in the subpanels of Figure 4.12, together with the bright-field "zero loss" image that is informative about the morphology of the NPs. Fe and Co elemental maps are almost indistinguishable, demonstrating that Fe and Co are not segregated within the single NP and homogeneously distributed within the sample. The O contrast map highlights the formation of a thin oxide shell at the surface of the NPs.

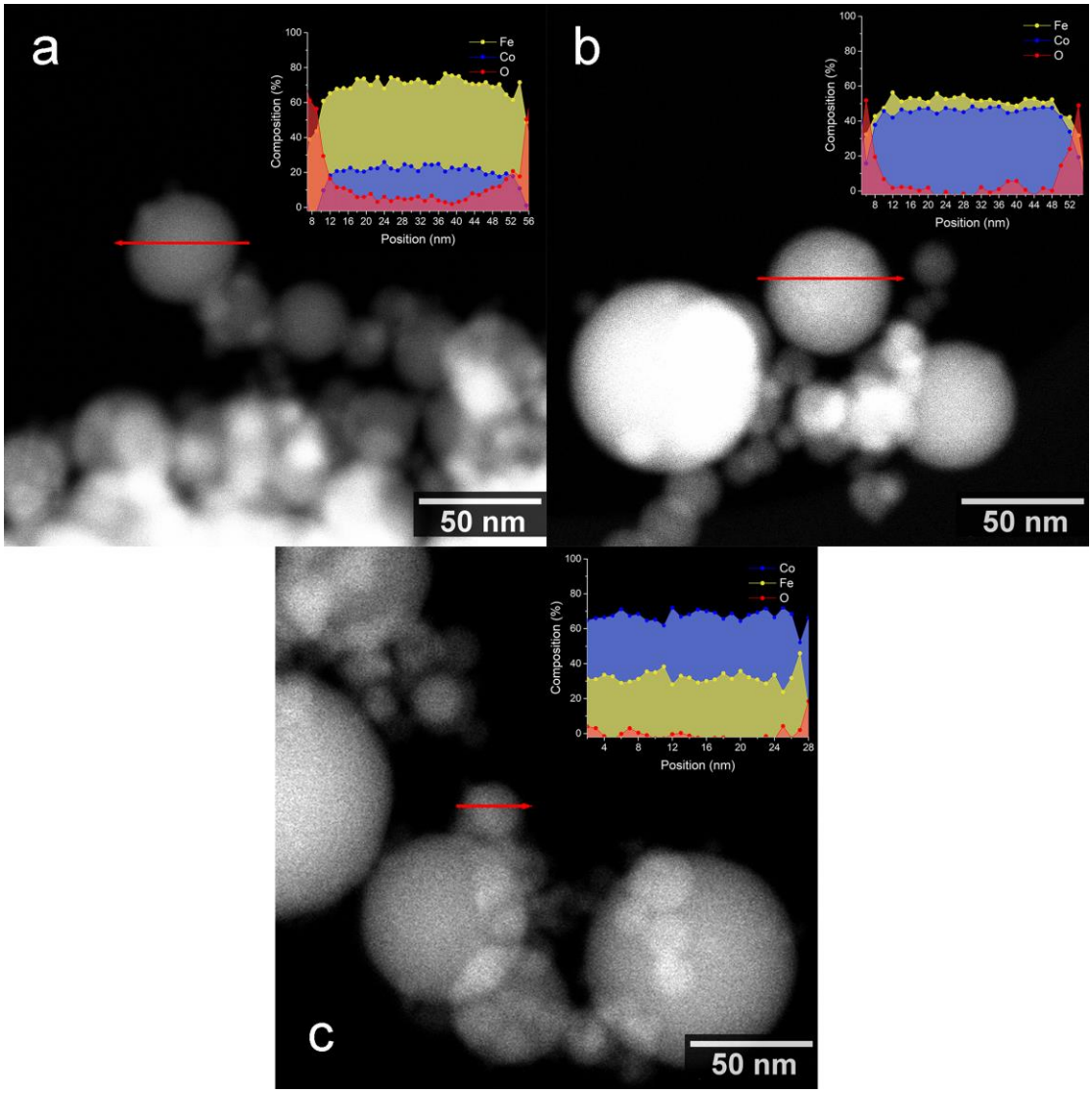

Figure 4.13 STEM image for (a) 23 at% (b) 50at%; (c) 70 at% Co content sample. The blue, yellow and red lines represents the quantitative elemental composition of Co, Fe and O, respectively, as obtained by the STEM-EELS linescan profiles.

A quantitative information of the elemental distribution within the single NP is given by the STEM-EELS line scan profiles reported in Figure 4.13. The Fe/Co content ratio in the core of the NPs is constant along the profiles and does not significantly deviate from the average elemental composition as determined by SEM-EDX analysis.

The formation of an oxide shell is observed for the two samples with lower Co content. In both samples the surface is richer in Fe with respect to the core of the NP. For the $Fe_{70}Co_{30}$ sample, it can be determined to be Fe_3O_4, while in the case of $Fe_{75}Co_{25}$, it is $CoFe_2O_4$. This finding can be interpreted considering the thermodynamically more favorable oxidation of Fe with respect to Co. From the STEM-EELS profile of $Fe_{30}Co_{70}$ sample, the formation of a clearly distinguishable oxide is not observed.

Figure 4.14. displays HRTEM images representative of the $Fe_{30}Co_{70}$ sample. The metallic-oxide core-shell structure could be clearly identified within the sample (Figure 4.13a-c), the shell having a magnetite-type crystal structure (Figure 4.13d),. The shell thickness is ~10 atomic layers, corresponding to $2-3\ \mathrm{nm}$. However, Figure 4.14.b spots the presence of NPs not enveloped in an oxide shell, as it was observed for the STEM-EELS profile in Figure 4.13c. This finding is in accordance also with the increasing oxidation resistance with increasing Co content observed in Chapter 4.1 for $Fe-Co$ NPs grown by Thermal GPC. For what concerns the core structure, all the observed NPs are single crystals $FeCo$ BCC, regardless on the size.

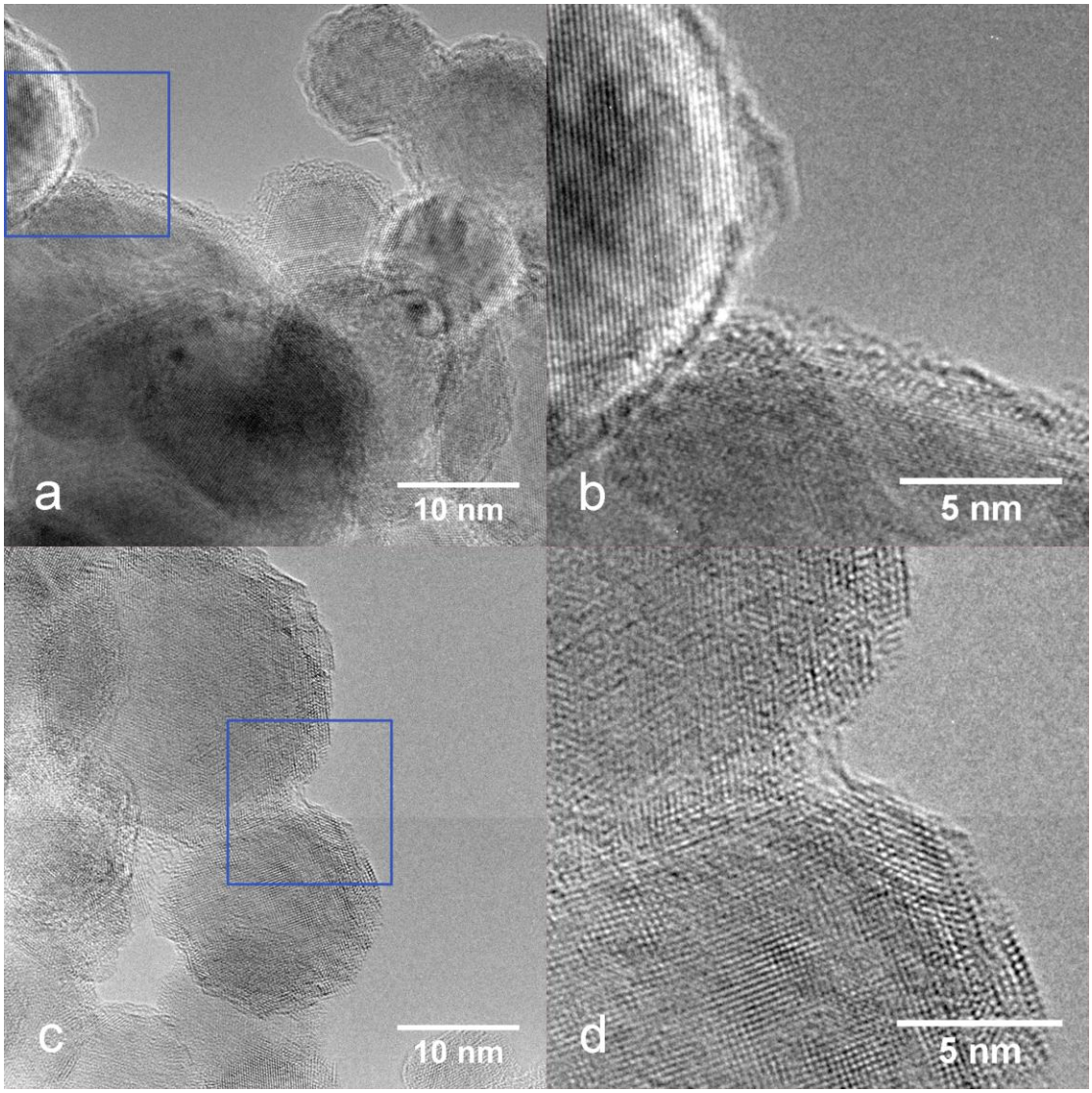

Figure 4.14. HRTEM images for the the $Fe_{30}Co_{70}$ sample. Image b and d are higher magnification of the blue squared zone in image a and c respectively.

4.3. CO_2 hydrogenation

The production of synthetic fuels is an appealing and strategy for energy storage as an alternative to hydrogen storage in hydrides and to batteries. Beside retaining all of the advantage of the well-established hydrocarbon-based technologies, the capture of CO_2 emitted upon combustion and its subsequent hydrogenation with hydrogen produced using renewable energy would allow to close the carbon cycle, with no net CO_2 emission[138,139].

The focus of the investigations is to find a material that could overcome the high stability of the CO_2 molecule ($\Delta_f H^0_{298K,CO_2} = -393.5\,kJ/mol$) by efficiently catalyzing the hydrogenation reaction towards the synthesis of longer chained hydrocarbons (HC_{2+}). There are different known pathways for the synthesis of hydrocarbons:

(SR) $$CO_2 + 4H_2 \leftrightarrow CH_4 + 2H_2O \quad (4.1)$$

(FT) $$nCO + (2n+1)H_2 \leftrightarrow C_n H_{2n+2} + nH_2O \quad (4.2)$$

(RWGS) $$CO_2 + H_2 \leftrightarrow CO + 2H_2O \quad (4.3)$$

$$nCO_2 + (3n+1)H_2 \leftrightarrow C_n H_{2n+2} + 2nH_2O \quad (4.4)$$

Historically, there are two major reactions for the thermo-catalytic synthesis of hydrocarbons from CO_2 or CO: the Sabatier Reaction (SR, $\Delta H^0 = -164.9\,kJ/mol$), Equation (4.1), which is highly selective towards CH_4, and the Fischer-Tropsch (FT) reaction, Equation (4.2), which is up to date the industrially most relevant reaction to synthesize hydrocarbon fuels, alcohols and waxes from syngas (mixture of H_2 and CO, mainly). If the CO_2 obtained from the atmosphere or from local emitters is the starting molecule for the synthesis, the FT reaction can be combined with the endothermic reverse water gas-shift reaction (RWGS, $\Delta H^0 = +41.18\,kJ/mol$), Equation (4.3). Another variation is the direct conversion of CO_2 to higher hydrocarbons via a FT-like reaction, as in Equation (4.4).

Transition metals (Fe, Co, Ni, Cu) and their binary alloys have been identified as the most active catalysts for the formation of longer chained hydrocarbons (HC_{2+}) via direct CO_2 hydrogenation[125,140,141]. Among these, supported $Fe-Co$ based materials show the highest HC_{2+} yields: 25.4% HC_{2+} yield with 35.8% CO_2 conversion for K-promoted $Fe_{0.9}Co_{0.1}$ on Al_2O_3,[142] , or 14.3 % HC_{2+} yield with 33.3% CO_2 conversion for $Fe_{0.9}Co_{0.1}$ on TiO_2 (1.1MPa, 573K)[141].
These materials are typically grown in the form of nanoparticles to maximize the surface/ volume ratio and need to be supported onto a porous oxide framework or to be dispersed within an oxide matrix to increase thermal stability and prevent sintering in the harsh conditions of reactors. However, it is well known that the supporting oxides can also alter the reaction[143].

The growth of $Fe-Co$ NPs by Gas Phase Condensation presented in previous sections of this Chapter is part of a collaboration with the Institute of Nanotechnology of the Karlsruhe Institute of Technology (KIT-INT, Germany). Catalytic characterization was performed by collaborators at the Laboratory of Materials for Renewable Energy (LMER) of the École Polytechnique Fédérale de Lausanne (EPFL, Switzerland).
This project articulates in two steps. The first aims at contributing to a better understanding of the fundamental effect of alloying on the on the CO_2 hydrogenation reaction. Some preliminary catalytic measurements performed on $Fe-Co$ NPs grown by Thermal GPC are shown in the next section. In a second step, the effect of Alumina support and the different loading of $Fe-Co$ catalyst will be explored. Measurements are still on going and the results will be available in future papers.

4.3.1. Experimental Setup

The CO_2 hydrogenation experiments are carried out at the EPFL in a homemade gas controlling and analysis system coupled with a stainless steel plug flow reactor inserted in a furnace[144]. A $\sim 10\,mg$ mass of catalyst sample is dispersed on glass wool to better distribute it in the reactor tube. A thermocouple placed in close proximity with the catalyst is used to precisely determine the temperature of the reaction. After loading the system, both the sample and the gas lines are pre-heated to about $393\ K$ while flushing He stream in order to evaporate the residual water vapor within the system. After the He pretreatment, the catalyst is exposed to a $7.5\ nml/min\ H_2$ and $2.5\ nml/min\ He$ gas mixture at $393\ K$ to further reduce remaining oxides.

During the CO_2 hydrogenation experiment, a total $10\mathrm{nml/min}$ gas ($6\,\mathrm{nml/min}\,H_2$ 99.995% purity, $1.5\,\mathrm{nml/min}\,CO_2$ 99.998% purity and $2.5\ \mathrm{nml/min}\,\mathrm{He}$, 99.999% purity) was continuously fed to the system. The individual flow rates were chosen to achieve a $H_2{:}\,CO_2 = 4{:}\,1$ gas mixture ratio. The catalytic properties were tested at ambient pressure and the temperature was ramped up with a $2\ \mathrm{K/min}$ heating rate in the $393 - 810\ \mathrm{K}$ range. The products in the gas stream were analyzed using a *Pfeiffer Omnistar 320* mass spectrometer. The activity and selectivity of the different catalysts are directly comparable: the quantitative results[144,145] are in fact normalized to a reference pressure, which is the same for all the experiments.

4.3.2. Catalytic properties

Figure 4.17c shows the catalytic effect of the set of $Fe_{100-x}Co_x$ samples ($x = 0, 23, 48, 68, 100$) over the CO_2 conversion process. The shaded area represents the total CO_2 conversion together with the separate contribution given by CH_4 and CO yields highlighted in green and grey, respectively. All the samples are active in the catalysis CO_2 conversion.

The $Fe-Co$ alloy NPs shows a different temperature dependence of the CH_4 and CO yields. These samples have a much higher selectivity toward CO and an intermediate one for CH_4, while pure Fe and Co are almost only active towards the CO and CH_4 production, respectively. Noticeably, $Fe-Co$ alloy displays a new activity in the formation of longer chained hydrocarbons $C_2 - C_5$, as shown separately in Figure 4.17a in a proper scale. The total yield of the latter would be <1% and is not reported in Figure 4.17a. No clear trend for the maximal conversion of $C_2 - C_5$ products as function of the Fe content in the alloy can be determined. The high activity of these samples towards CO also suggests that, rather than having the direct hydrogenation of CO_2 into hydrocarbons, the $C_2 - C_5$ production is more likely the result of the combination of RWGS and FT reactions.

At the best of my knowledge, no simulation studies on the catalytic properties of the BCC $Fe-Co$ alloy are reported in literature. A possible explanation on the basis of theoretical works on Fe and Co surfaces[146] is presented in the following. Based on the previous experimental observations, here we consider the CO_2 adsorption and decomposition process, because we argued that these processes play a fundamental role in the CO_2 hydrogenation and in HC_{2+} formation.

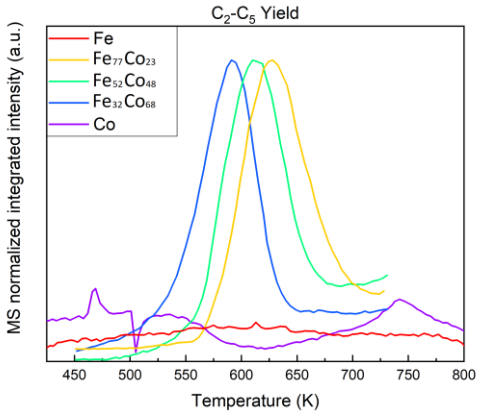

Figure 4.17a. the solid-line plots show (semi-quantitatively) the conversion of the summed up $C_2 - C_5$ mass spectrometer normalized signals correspondent to the $m/Z = 26, 29, 30, 39, 56, 57, 70$ peaks.

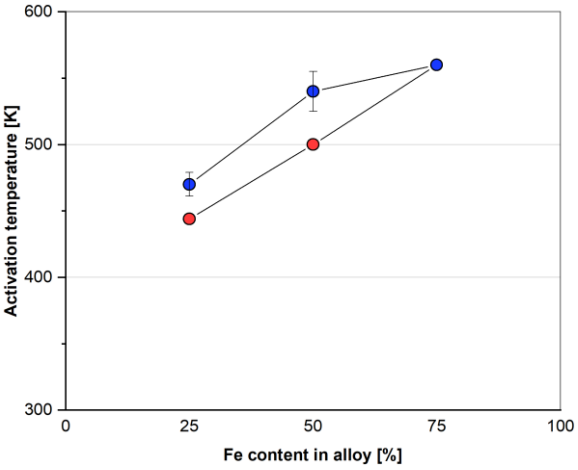

Figure 4.17b. Activation temperature of the catalysts in the CO_2 hydrogenation reaction as function of their Fe content. The blue datapoints are referred to $C_2 - C_5$, the red datapoints correspond to the activation temperature of C_1 molecules.

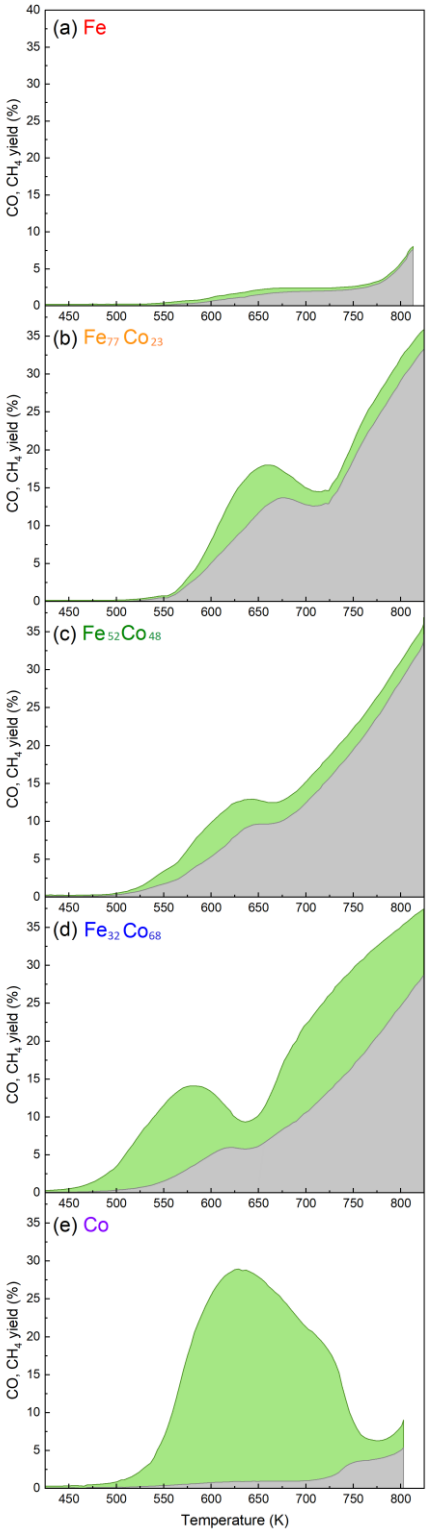

Figure 4.17c. Catalytic properties of $Fe_{100-x}Co_x$ $(x = 0, 23, 48, 68, 0)$ in a flow reactor with 4:1 H_2: CO_2 ratio, 1 bar and $10\ nml/min$, measured by mass spectroscopy. The shadowed area is the total CO_2 conversion with the separated contributions of CO and CH_4 yield in grey and green, respectively.

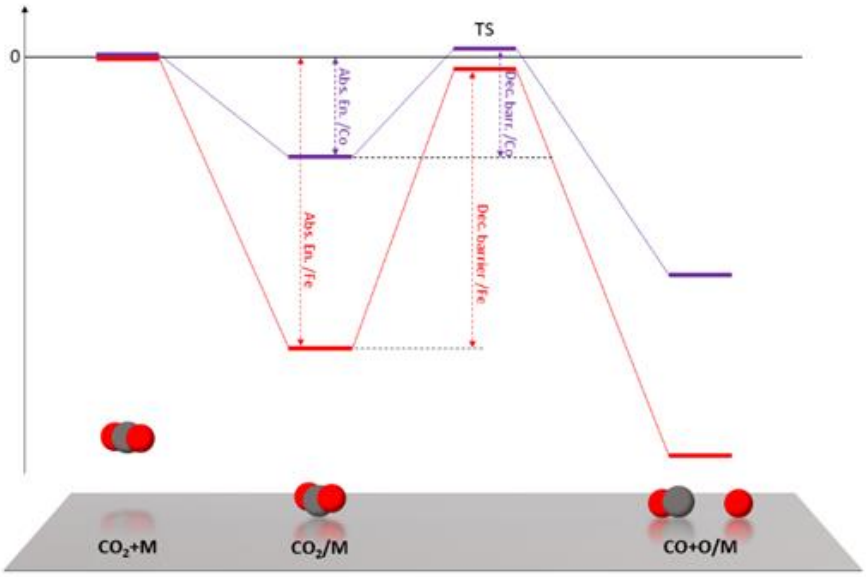

Figure 4.18. Schematic representation of thecalculated enegy levels of (from left to right) free CO_2, adsorbed CO_2, transition state, decomposed CO_2 into $CO + O$. In red relative to Fe surface, in purple relative to Co surface. The dashed vertical lines highlight the difference between Fe and Co in adsorption energy and decomposition barrier. [146]

Figure 4.18 provides with a useful schematic representation of the energy levels involved in the CO_2 hydrogenation process. The CO_2 is easily and strongly adsorbed on Fe surfaces (red path), so that the surface of NPs results covered in CO_2 molecules. However, the strong adsorption together with the high energy level of the intermediate states results in a large energy barrier that requires very high temperature to be overcome and very poor CO_2 conversion rates are observed.

Quite the opposite is for Co surfaces that weakly adsorb CO_2, meaning that adsorption process is more difficult to occur, but the energy barrier for CO_2 decomposition to CO is smaller and most of the adsorbed molecules are readily decomposed. However, the few and isolated CO molecules produced cannot form the $C - C$ bonds to start a HC_{2+} chain, resulting in the production of CO or CH_4 only.

It is reasonable to expect from the $Fe - Co$ alloy an intermediate behavior dependent on its composition. This view is supported by our experimental finding that the activation energy and temperature of $C_2 - C_5$ formation increase with increasing Fe content in the alloy (Figure 4.17b). A higher activation temperature is in fact explained by a higher energy barrier that is caused by stronger interaction of the adsorbed species with the surface, as it is the case of Fe. By adjusting the Fe/Co ratio in the alloy, it is therefore possible to tune the CO_2 adsorption energy and decomposition barrier to reach a good compromise between the amount of adsorbed CO_2 and the

decomposition rate to CO. The result is an abundance of adsorbed CO, which is the starting point in the formation of $C-C$ bonds for the growth of HC_{2+} chains in FT synthesis.

For C_2-C_5 products, the activation temperature is similar (see the error bars in Figure 4.17b) and slightly higher than the activation temperature of CH_4 ($\Delta T \sim 35\ K$ for $Fe_{32}Co_{68}$ and $Fe_{52}Co_{48}$). The difference of activation temperature ΔT between CH_4 and C_2-C_5 is explained by taking into account the superior kinetics of the Sabatier reaction compared to the RWGS + FT reaction[147], especially at lower temperatures where Sabatier reaction is also thermodynamically favoured. This is also the reason why at $560\ K$, $\Delta T \sim 0\ K$ for the Fe richest sample, $Fe_{77}Co_{23}$: at higher temperatures CO synthesis through RWGS is favoured and competes with Sabatier reaction.

4.4. Major Results

In this Chapter, both the Thermal and Pulsed Laser GPC technique were successfully employed to synthesize $\mathrm{Fe-Co}$ alloy nanoparticles. With these techniques, metallic nanoparticles can be grown in an inert atmosphere starting from high purity precursors.

A certain degree of agglomeration is typical of Thermal GPC and NPs appear partially welded in flake structures. NPs with controlled $\mathrm{Fe/Co}$ ratio and average size spanning between $10\,\mathrm{nm}$ and $13\,\mathrm{nm}$ are grown, featuring a relatively narrow size distribution. The stoichiometry of the precursor can be quite well preserved because Fe and Co have similar vapor pressures. Nevertheless, the slightly higher evaporation rate of Fe can be the reason for the small increase in the Fe content noticeable for the Co-richest sample. This effect could have an important impact over the homogeneity of samples obtained with prolonged evaporation, due to the progressive decreasing content ratio of the element with higher evaporation rate in the precursor alloy.

$\mathrm{Fe-Co}$ NPs grown Pulsed Laser GPC feature larger size distribution. However, the NPs are spherical and well separated, thus being better candidates for colloidal dispersions. The elemental composition of the precursor metallic target is preserved in the grown sample. This could be related to the almost identical surface tension and vapor pressure of Fe and Co. Therefore, Fe and Co should behave very similarly in the plasma flow and the condensation and coagulation of the two elements occurs equally. Some larger NPs ($\sim 80\,\mathrm{nm}$) are also spotted, also featuring spherical shape and being single crystal structure.

The catalytic role of $\mathrm{Fe-Co}$ NPs in $\mathrm{CO_2}$ hydrogenation was investigated. The alloyed NPs showed improved catalytic activities for $\mathrm{CO_2}$ hydrogenation compared to pure Fe and pure Co NPs, Furthermore, the alloy catalysts show a genuinely new activity in the production of $\mathrm{C_2-C_5}$ hydrocarbon, while Co and Fe NPs only lead to $\mathrm{CH_4}$ and CO, respectively. It is proposed that the alloys are active in the synthesis of hydrocarbons by tuning the adsorption energy and decomposition barrier of $\mathrm{CO_2}$ on the metal surface between the too weak adsorption of Co and the strong one of Fe.

Chapter 5.

Fe-Co/TiOx nanocomposites

5.1. Oxide supported metal nanoparticles

Oxide-supported metal NPs are a class of functional materials that find innovative applications in many materials science fields such as catalysis for the production of synthetic hydrocarbons[145,148,149] and CO reduction[150], chemical synthesis[151,152], nanoplasmonics[153] for the development of higher efficiency photovoltaic cells [151,154], and magnetism[155]. The presence of the oxide support within the nanocomposite does not only affect the size and shape of metal NPs[6,156], but is also crucial to prevent coarsening and sintering[157], and is often responsible for a radical change in physical properties because of electronic interactions at interfacial sites[158–160].

In the last decade, much efforts have been devoted to the development of novel and flexible synthesis routes for metal/oxide nanocomposites (NCs). Most of these techniques involve two-step processes, in which a porous oxide host (typically zeolites or Al_2O_3) or oxide NPs[161] are imbued with a colloidal suspension of metallic NPs produced via physical (e.g. pulsed laser ablation in liquid) or chemical methods (e.g. precipitation and nitride impregnation). Metal NPs encapsulation into oxide shells[162] and in pores and channels of hierarchical zeolites has been also reported but, albeit innovative, these approaches do not convey a homogeneous distribution of the supported NPs and are limited to a small range of materials[163]. Mechanochemistry via ball milling followed by suitable thermal treatments can be successfully applied to the synthesis of metallic NPs in an oxide matrix[164]. However, it is not possible to control the morphology of the metal and oxide particles independently, and ductile materials are very difficult to process. Metallic NPs embedded in an oxide matrix can be prepared by a sol-gel method[122,165], again with some limitations on the independent control of the two phases. The deposition of metallic NPs on oxide surfaces is of great importance for fundamental studies on model systems[166], but cannot be efficiently employed for the synthesis of 3D bulk materials.

In this Chapter, a novel one-step strategy for the synthesis of metal-oxide NCs through the physical assembly of NPs is presented. More specifically, NPs are formed by gas phase condensation of metallic vapors in a He/O_2 mixed atmosphere. Two

metallic precursors with different oxidation enthalpies are evaporated simultaneously and independently; the one with less negative enthalpy forms metallic NPs, while the other provides the seed for oxide NPs. Thermal treatments in suitable atmosphere can be further applied to modify structure and morphology.

The following content is divided in two parts. In the first, the Ti-oxide (TiO_x) NPs growth is investigated, demonstrating that the stoichiometry and crystalline structure of TiO_x can be tailored by controlling the O_2 partial pressure during the synthesis and processing atmosphere. In the second part, the previously anticipated NCs growth concept is applied to the synthesis of TiO_x supported $Fe-Co$ ($Fe-Co/TiO_x$) NCs.

5.2. TiO_2 nanoparticles

5.2.1. Experimental Setup

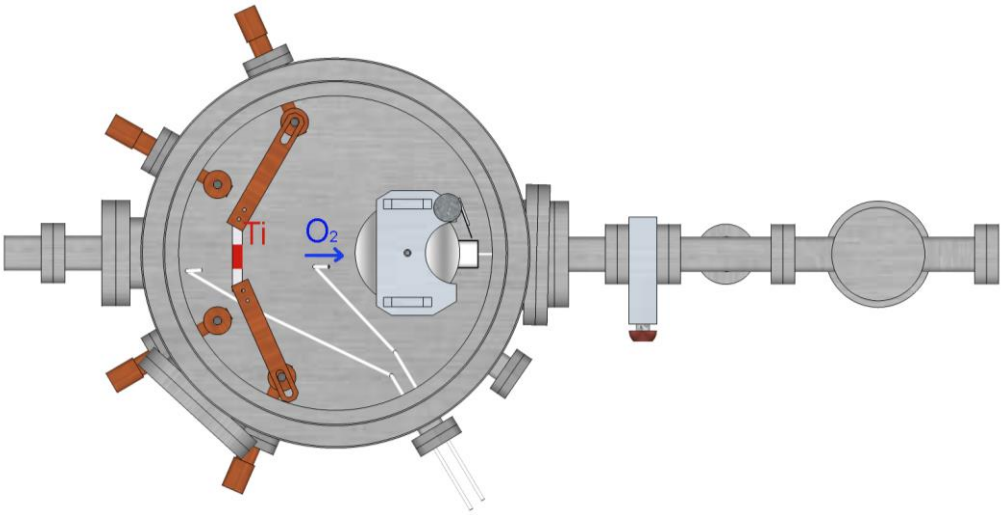

Figure 5.1. Setup for the growth of the TiO_2 nanoparticles.

$Ti-$oxide NPs are grown by Reactive Gas Phase Condensation using Ti powder (*Alpha Aesar* 99.9%, 150 mesh) as metal precursors. Prior to the evaporation, Ti was heated under vacuum above the melting point of Ti ($1668\ °C$) and then rapidly cooled down to remove any contaminant adsorbed on the precursor. During the evaporation stage, a He/O_2 gas mixture is continuously fed to the system and the overall pressure is dynamically kept constant to $\sim 260\ Pa$ pressure. The O_2 content in the condensation atmosphere can be varied by directly acting on the immitted He/O_2 flux ratio. However, in all the experiments reported here the O_2 content in the atmosphere was kept below 1 mol.%, to avoid the oxidation of the W heating boat.

Two samples, named $\mathrm{Ti-O\_}l$ and $\mathrm{Ti-O\_}h$, were synthetized at $\mathrm{O_2}$ partial pressures of 0.4 and $2.2\ \mathrm{Pa}$, respectively. Table 5.1 lists the conditions applied during the synthesis and the successive treatments. The further thermal treatments were performed for 24 hours at $T = 673\ \mathrm{K}$ and $p = 0.1\ \mathrm{MPa}$ either in $\mathrm{H_2}$ (99.995% purity), Ar (99.999% purity) or air in a tubular stainless-steel oven.

Table 5.1. Gas flow and O_2 partial pressure during the synthesis of TiO_x NPs. The total pressure was 260 Pa. The samples were examined as-prepared and after being subjected to different thermal treatments as indicated.

Sample	Inlet flow [nml/min]		O_2 partial P [Pa]	Post-synthesis treatment (P=0.1 MPa, T=673 K)		
	He	O_2		H_2	Ar	air
$\mathrm{Ti-O\_}l$	60.0	0.1	0.4	x	x	x
$\mathrm{Ti-O\_}h$	60.0	0.5	2.2			x

5.2.2. As prepared samples: the influence of O_2 in the condensation atmosphere

The XRD patterns in Figure 5.2 demonstrate the effect of the $\mathrm{O_2}$ content in the condensation atmosphere on the structure of the as-prepared $\mathrm{Ti}-$oxide NPs.

When a $0.1\ \mathrm{nml/min}\ \mathrm{O_2}$ flux is fed (sample $\mathrm{Ti-O\_}l$), corresponding to a $0.4\ \mathrm{Pa}$ partial $\mathrm{O_2}$ pressure, crystalline Ti monoxide ($\mathrm{TiO_{1-\delta}}$) NPs are obtained (Figure 5.2a). $\mathrm{TiO_{1-\delta}}$ has a disordered nonstoichiometric rock-salt structure that can exist over a wide compositional range, from $\delta = 0.30$ to $\delta = -0.25$, due to the presence of vacancies in both the Ti and O sub-lattices[167–169]. It is kinetically stable up to about $400\ °\mathrm{C}$. The broadening of $\mathrm{TiO_{1-\delta}}$ XRD peaks results from the small crystalline size and the large root-mean-square microstrain ε_{rms}. The relative height of the (111) and (200) $\mathrm{TiO_{1-\delta}}$ peaks, the correspondent Bragg reflection being at $2\theta_{111} \approx 37.3°$ and $2\theta_{200} \approx 43.4°$, is strongly influenced by the Ti and O sub-lattices occupancy factor and allows to estimate the average stoichiometry of the $\mathrm{TiO_{1-\delta}}$. From the Rietveld analysis, an average crystal size $d_{\mathrm{TiO}} = 9 \pm 2\ \mathrm{nm}$, $\varepsilon_{rms} \approx 2\ \%$ and $\delta = 0.25 \pm 0.05$, that is a $\mathrm{TiO_{0.75(5)}}$ oxygen deficient average stoichiometry, were determined. However, the high microstrain points to a non-homogeneous stoichiometry across the sample. In fact, the poor quality of the fit in Figure 5.2a indicates that a model with a single value of δ and d_{TiO} does not satisfactorily describe the structure of $\mathrm{TiO_{1-\delta}}$ NPs, suggesting that the δ value may experience significant fluctuations among the NPs depending on their diameter and on small variations in the vapor pressure during the synthesis.

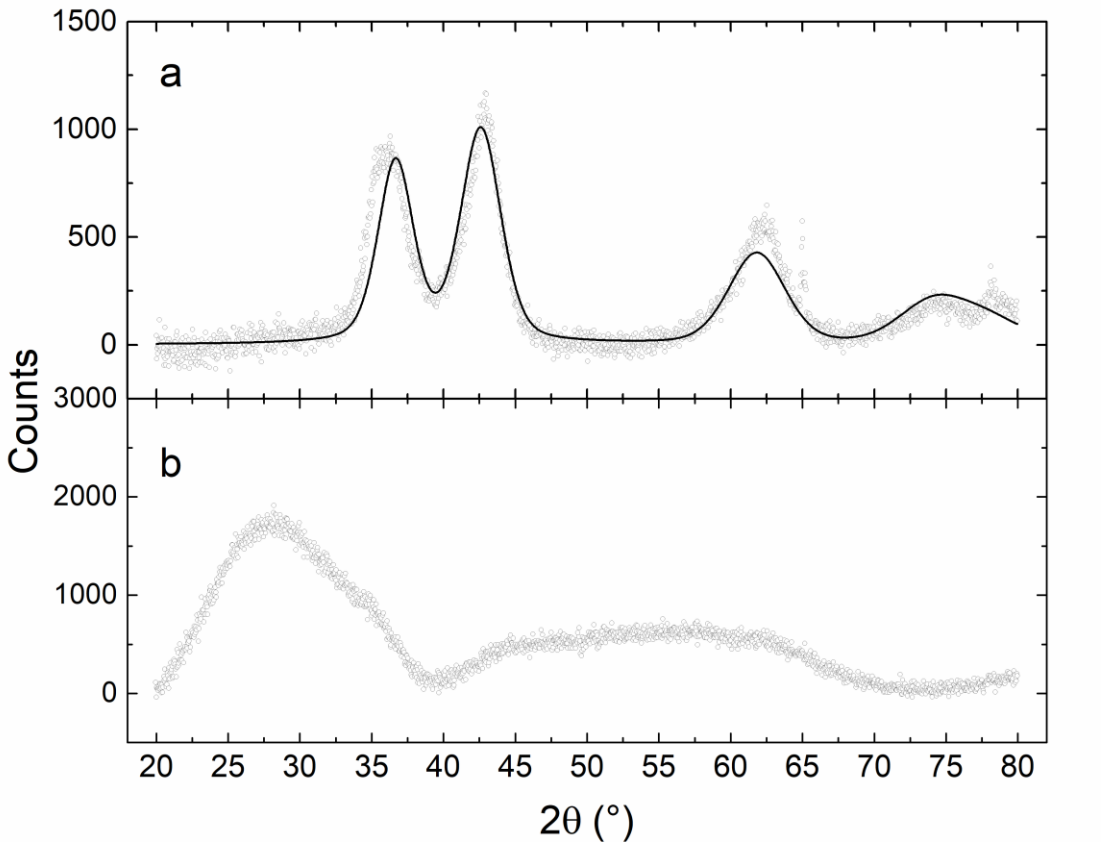

Figure 5.2. XRD patterns of as-prepared TiO_x NPs. (a) $\mathrm{Ti}-\mathrm{O}\_l$; (b) $\mathrm{Ti}-\mathrm{O}\_h$. The grey circles represent experimental data. The result of Rietveld refinement is shown for $\mathrm{Ti}-\mathrm{O}\_l$ as a black solid line.

At higher O_2 content in the condensation atmosphere (sample $\mathrm{Ti}-\mathrm{O}\_h$), two broad humps (Figure 5.2b) suggest the formation of amorphous TiO_2, as indicated by previous studies[30], while the Bragg reflections of $TiO_{1-\delta}$ are not detected.

5.2.3. The influence of thermal treatment atmosphere

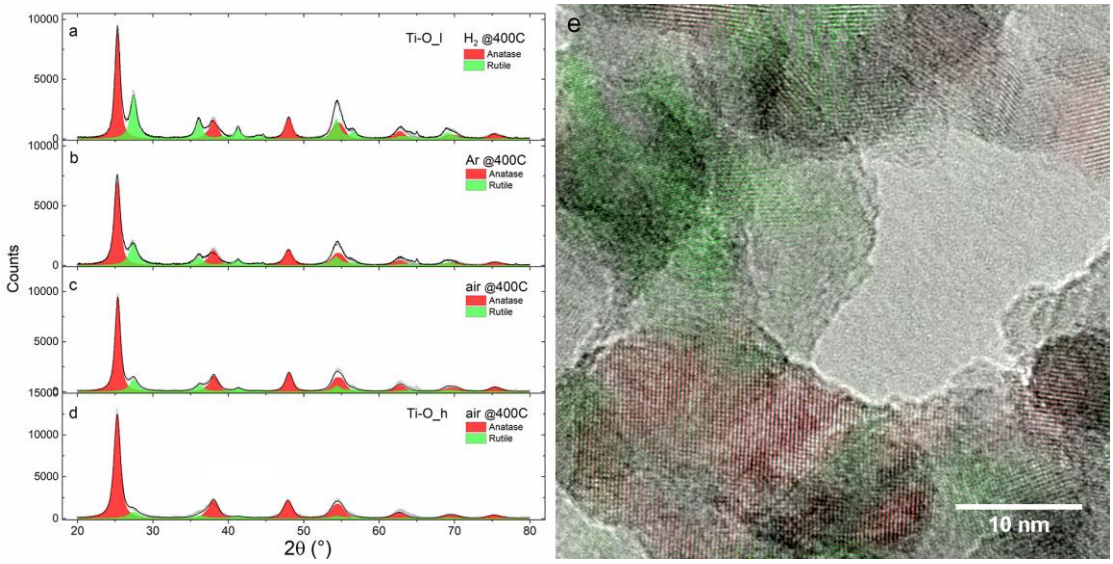

Figure 5.3. XRD patterns of TiO_x NPs samples after a thermal treatment at 400 °C. (a-c) sample $\mathbf{Ti-O\_}\boldsymbol{l}$ in (a) H_2, (b) Ar, and (c) air; (d) sample $\mathrm{Ti-O\_}h$ in air. The results of Rietveld refinement are reported inTable 5.2; (e) HR-TEM image of sample $\mathrm{Ti-O\_}l$ treated in air, corresponding to pattern (c), with the anatase and rutile fringes highlighted in red and green, respectively.

The XRD patterns of the $\mathrm{Ti}-$oxide NPs subjected to thermal treatments at $T = 673\ \mathrm{K}$ are reported in Figure 5.3. The $\mathrm{TiO}_{1-\delta}$ phase is no longer detected in the treated $\mathrm{Ti-O\_}l$ sample, while rutile and anatase TiO_2 Bragg reflections are spotted. The anatase content increases with the oxidative power of the atmosphere, as reported in Table 5.2, varying from $56 \pm 1\ \mathrm{wt\%}$ (in H_2) to $74 \pm 2\ \mathrm{wt\%}$ (in air). After the thermal treatment in air, $\mathrm{Ti-O\_}h$ sample is no longer amorphous and displays the higher anatase TiO_2 content, $84 \pm 1\ \mathrm{wt\%}$. The anatase crystallite phase ranges between $13 - 16\ \mathrm{nm}$, with no apparent significant correlation with the anatase content. The rutile average size of crystallites is smaller and decreases with the decreasing rutile content.

Table 5.2. Quantitative phase analysis for $\mathbf{TiO}_x$ NPs samples after thermal treatments: rutile vs anatase abundance (wt%), crystallite size $\boldsymbol{d}$ and lattice parameters a and c.

Treatment Atmosphere p=0.1 MPa, T=673 K	Anatase TiO_2				Rutile TiO_2			
	wt%	d (nm)	a(Å)	c(Å)	wt%	d (nm)	a(Å)	c(Å)
				$p(O_2)$: 0.4 Pa				
H_2	56(1)	16(2)	3.7895(3)	9.465(2)	44(1)	11(1)	4.5970(7)	2.9568(8)
Ar	64(1)	14(2)	3.790(1)	9.459(2)	36(1)	8(1)	4.600(1)	2.956(2)
air	74(2)	15(2)	3.7855(3)	9.461(2)	26(2)	8(2)	4.597(2)	2.945(2)
				$p(O_2)$: 2.2 Pa				
air	84(1)	13(1)	3.798(2)	9.4691(4)	16(1)	6.0(5)	4.595(6)	2.945(6)

The HR-TEM image in Figure 5.3e reveals the coexistence of rutile and anatase polymorphs on a nanoscale level and confirms that no residual metallic Ti is left after the treatments, in agreement with the results of previous X-ray absorption experiments [30].

The results related to synthesis and processing of $\mathrm{Ti}-$oxide NPs can be rationalized as follows. If the $\mathrm{O_2}$ content in the synthesis atmosphere is too low, as is the case for $\mathrm{Ti-O\_}l$, full oxidation of the nucleated Ti NPs into $\mathrm{TiO_2}$ is not possible, and non-stoichiometric $\mathrm{TiO_{1-\delta}}$ is obtained. This is not because the initial $\mathrm{O_2}$ partial pressure ($0.4\ \mathrm{Pa}$) is below the equilibrium pressure for $\mathrm{TiO_2}$ formation (which is ridiculously low, i.e. $\sim 10^{-59}\ \mathrm{Pa}$ at $673\ \mathrm{K}$ and $\sim 10^{-150}\ \mathrm{Pa}$ at room temperature) but because there is not enough $\mathrm{O_2}$ available. The freshly evaporated Ti consumes almost all the $\mathrm{O_2}$ and the competition between the evaporation rate and the $\mathrm{O_2}$ inlet flow rate dictates the final stoichiometry. Therefore, it should be possible to tailor the off-stoichiometry δ by playing with these parameters; this may be the subject of future experiments. It is also worth noticing that the $\mathrm{TiO_{1-\delta}}$ NPs obtained in this way are kinetically stable at room temperature, i.e. they are not oxidized into $\mathrm{TiO_2}$ upon exposure to ambient air.

Conversely, at sufficiently high $\mathrm{O_2}$ inlet flow (sample $\mathrm{Ti-O\_}h$), it is possible to achieve (almost) full oxidation of the NPs. It is well known that amorphous $\mathrm{TiO_2}$ is obtained when oxidation is carried out close to room temperature, whereas oxidation above $630\ \mathrm{K}$ leads to crystalline $\mathrm{TiO_2}$ [170]. This suggests that NPs oxidation takes place after cooling down from the evaporation temperature has taken place via thermalization with the surrounding He gas. In agreement with the vast literature on $\mathrm{TiO_2}$, crystallization of amorphous NPs is induced by a thermal treatment in air at 400 °C [30,171].

The formation of crystalline $\mathrm{TiO_2}$ by heating the $\mathrm{TiO_{1-\delta}}$ NPs in Ar or $\mathrm{H_2}$ is less straightforward but can be understood from thermodynamic data considering the presence of water vapor impurities. Let us take into account the following reaction, pertinent to the treatment in $\mathrm{H_2}$:

$$\mathrm{TiO} + \mathrm{H_2O} \quad \leftrightarrow \quad \mathrm{TiO_2} + \mathrm{H_2} \tag{5.1}$$

The ratio between the water vapor pressure $p_{\mathrm{H_2O}}$ and hydrogen pressure $p_{\mathrm{H_2}}$, at which reaction is at equilibrium, is determined by the Van 't Hoff equation:

$$\left(\frac{p_{\mathrm{H_2O}}}{p_{\mathrm{H_2}}}\right)_{eq} = \exp\left(\frac{\Delta H_{\mathrm{TiO_2}} - \Delta H_{\mathrm{H_2O}}}{2RT}\right) \tag{5.2}$$

Where $\Delta H_{\mathrm{TiO_2}} = -853\ \mathrm{kJ/mol\ O_2}$ is the enthalpy of TiO oxidation into $\mathrm{TiO_2}$ and $\Delta H_{\mathrm{H_2O}} = -495\ \mathrm{kJ/mol\ O_2}$ is the enthalpy of water formation. Equation (5.4), calculated at $\mathrm{T} = 673\ \mathrm{K}$, yields $\left(P_{H_2O}/P_{H_2}\right)_{eq} \approx 10^{-14}$ (more detailed calculations are reported in Appendix A). Since the water content due to impurities in the gas and to desorption from the reactor walls is certainly higher than that, we must expect that Reaction (5.3) proceeds rightwards, and the that oxidation of $\mathrm{TiO_{1-\delta}}$ NPs takes place during the thermal treatment. Notice that this behavior arises from the strongly negative formation enthalpy of $\mathrm{TiO_2}$; oxides of late transition metals such as Fe and Co, on the contrary, would be reduced under the same atmosphere. This is a key factor in the processing of NCs samples, as we will show later on.

The oxidative power of the treatment atmosphere influences the rutile to anatase ratio. This is also in agreement with the literature, which shows that oxygen-deficient conditions favor the formation of rutile [171], because rutile itself exhibits a slightly oxygen-deficient stoichiometry.

5.3. FeCo/TiOx nanocomposite

5.3.1. Experimental setup

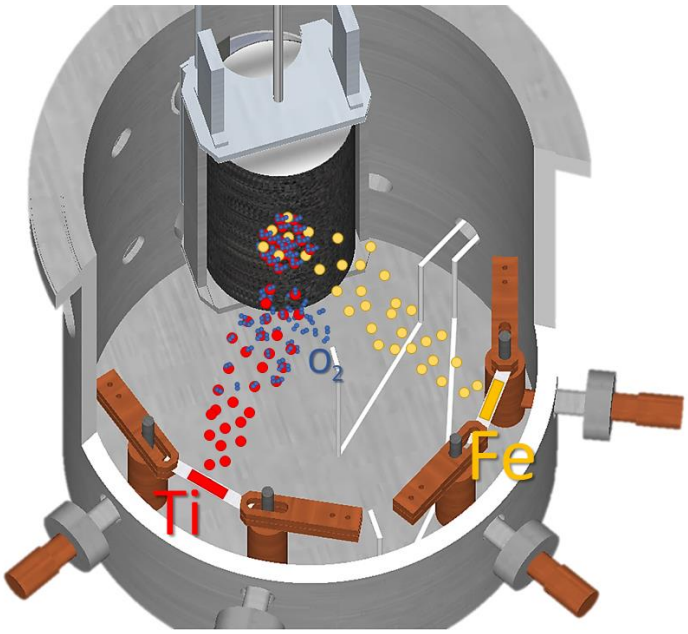

Figure 5.4. Setup the experimental for the growth of the $\mathrm{Fe/TiO}_x$ nanocomposites. Fe and Ti are coevaporated in a O_2 enriched He atmosphere. The O_2 is fed into the chaber close to the collection cylinder. The nanocomposite formation process is also schematized. The same picture also applies to $\mathrm{FeCo/TiO}_x$ nanocomposite formation.

To obtain $\mathrm{Fe}_{100-x}\mathrm{Co}_x$ NPs ($x = 0, 50$) supported on TiO_x NPs, the evaporation chamber was equipped with two tungsten evaporation boats, as displayed in Figure 5.4. The boats were separated by $\sim 30\ \mathrm{cm}$ in order to avoid the mixing of metal vapors before NPs nucleation, which may lead to the nucleation of a ternary $\mathrm{Ti-Fe-Co}$ alloy.

The NCs were grown in a $\sim 260\ \mathrm{Pa}$ O_2-enriched He atmosphere, that is the same used for the growth of $\mathrm{Ti-O\_}l$ sample described in the previous section. The individual evaporation rates of $\mathrm{Fe-Co}$ and Ti were monitored with the quartz crystal balance and tuned in order to obtain a $\mathrm{Fe-Co}$ content in the NCs of about $10\ \mathrm{wt\%}$. The relative $\mathrm{Fe/Co}$ content in the NCs determined by SEM-EDX was consistent with the precursor within the uncertainties. A summary of the experimental parameters is reported for convenience of the reader in Table 5.3.

Table 5.3. Gas flow and O_2 partial pressure during the synthesis of $\mathbf{Fe-Co/TiO}_x$ NCs. The total pressure was 260 Pa. The **Co** and **Fe** content in the mixed powder precursor are reported

Sample	Inlet flow [nml/min]		O_2 partial P [Pa]	Fe-Co precursor mixture [at%]	
	He	O_2		Fe	Co
$Fe\|TiO_x$	60.0	0.1	0.4	100	-
$Fe_{50}Co_{50}\|TiO_x$	60.0	0.1	0.4	50(1)	50(1)

5.3.2. Structural characterization

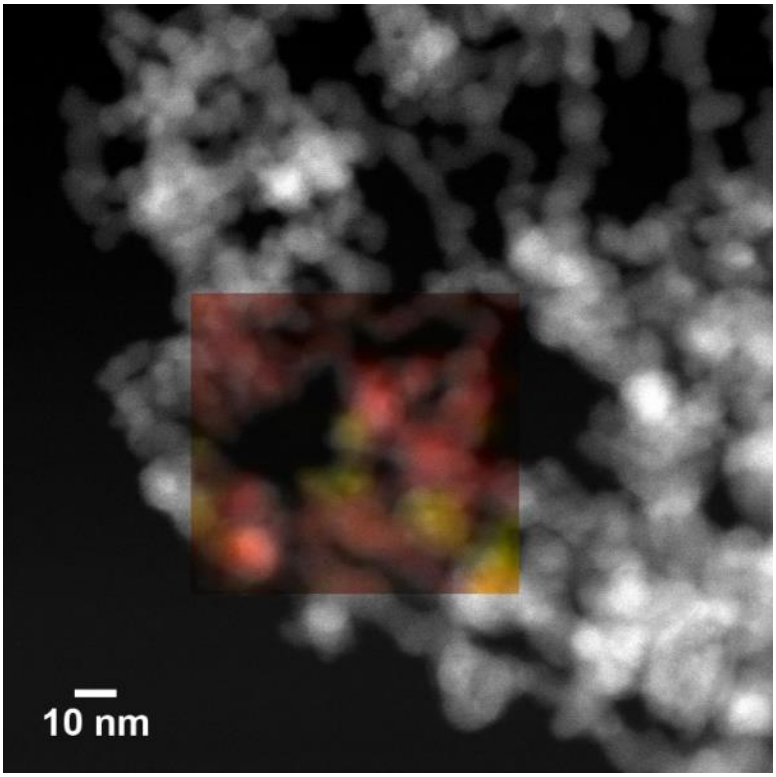

Figure 5.5. STEM-EDX elemental map of Fe (yellow) and Ti (red) in the as-prepared Fe/TiO_x NC.

The STEM EDX map in Figure 5.5 (superimposed to the corresponding STEM image) highlights the nanocomposite nature of the NPs assembly obtained by co-evaporation of Fe and Ti. The elemental distribution of Fe (yellow) and Ti (red) clearly shows the good intermixing of Fe −rich and Ti −rich NPs at the nanoscale level.

Figure 5.6a displays the XRD pattern relative to the as-prepared sample. Two main phases are spotted, being $\alpha - \mathrm{Fe}$ and $\mathrm{TiO}_{1-\delta}$. This result is confirmed by analysis of HR-TEM image in Figure 5.7, which also provides further information on phase distribution at the nanoscale. The FFTs of the regions labeled *a* and *b* are reported intimate contact between NPs constituted by $\alpha - \mathrm{Fe}$ (region *a*) and $\mathrm{TiO}_{1-\delta}$ (region *b*). The analysis of the selected area diffraction pattern in Figure 5.7c analysis, no further phases are detected within the material.

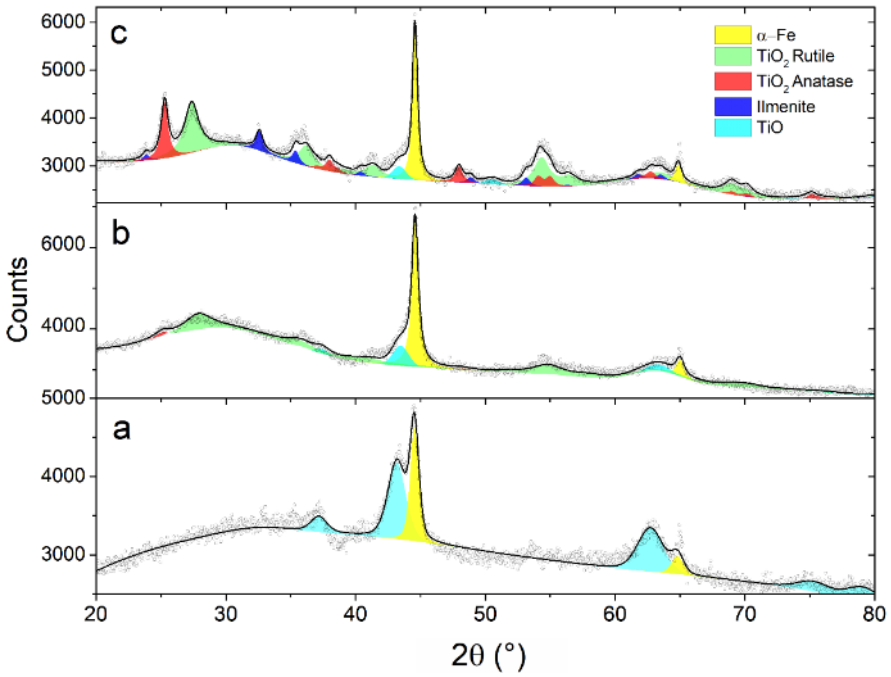

Figure 5.6. XRD patterns of Fe/TiO_x NCs. (a) As-prepared sample; (b-c) After thermal treatment in a H_2 atmosphere, 1 MPa, for (b) 4 hours and (c) 24 hours. The colored areas highlight the contributions of different phases to the Rietveld refinement. Grey circles represent experimental data, while the black solid line shows the overall best fit.the

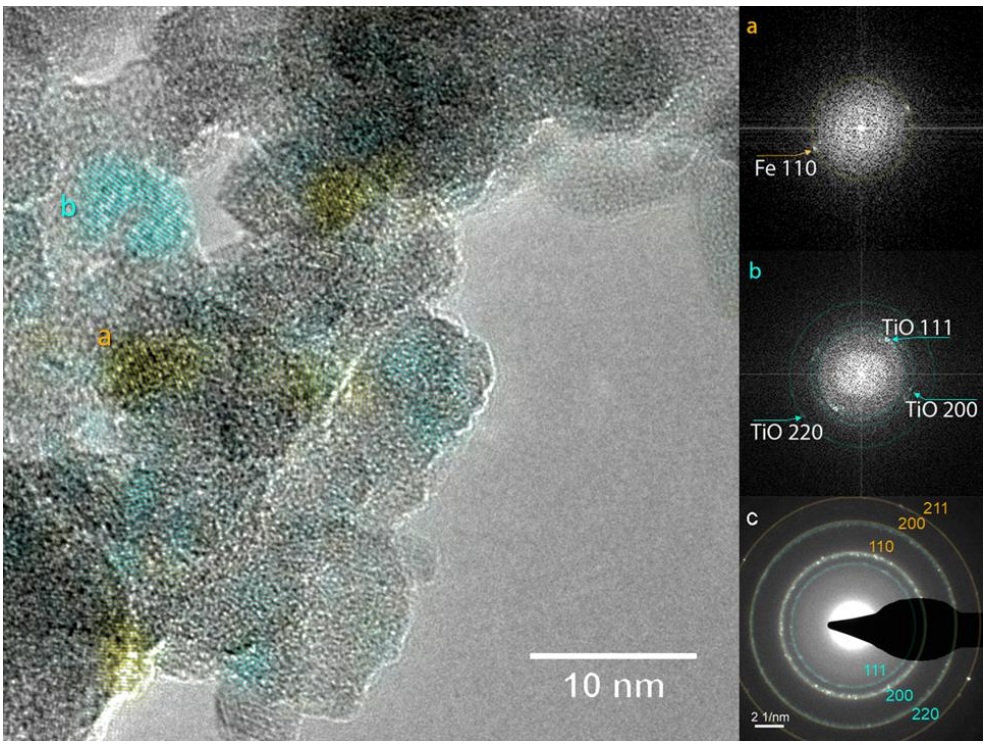

Figure 5.7. HR-TEM image of the as prepared Fe/TiO_x NC (left) and FFTs performed on selected areas labeled with lowercase letters showing the presence of (a) Fe and (b) $TiO_{1-\delta}$ lattice planes; (c) SAD pattern: Fe and $TiO_{1-\delta}$ lattice planes are labeled in yellow and cyan, respectively (yellow and cyan rings serve as guides for the eye). In the HR-TEM image, the lattice planes of Fe and $TiO_{1-\delta}$ are highlighted using the same colors.

With the purpose of evaluating the thermal stability and morphological evolution of these material in the same harsh conditions of a reactor for CO_2 reduction, we exposed this nanocomposite material to $1\ \mathrm{MPa}\ H_2$ atmosphere at $673\ \mathrm{K}$.

After 4 hours of thermal treatment the relative intensity of the $TiO_{1-\delta}$ peaks in XRD pattern in Figure 5.6b is significantly lowered. At the same time, some broad peaks attributable to anatase and rutile TiO_2 phases are spotted. The crystallite size of α-Fe estimated from XRD pattern refinement changes from $18 \pm 2\ \mathrm{nm}$ of the as-prepared sample to $21 \pm 2\ \mathrm{nm}$ and is almost unaffected by the treatment. The STEM-EDX analysis in Figure 5.8 spots a α-Fe NP of about $13\ \mathrm{nm}$, which appear brighter, in contact with $\mathrm{Ti}-$oxide NPs

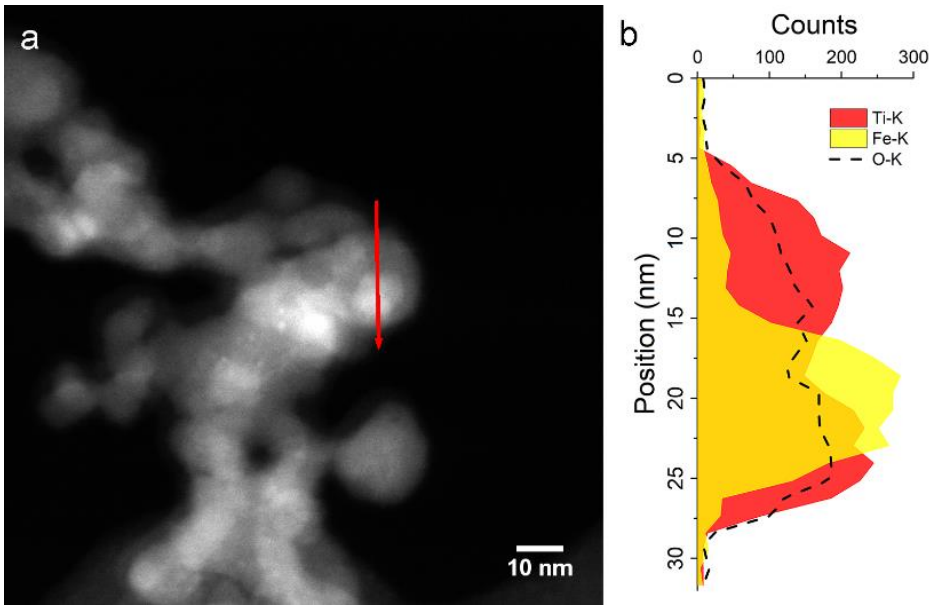

Figure 5.8. Fe/TiO_x sample after 4 hours in 1 MPa H_2 at 400°C. (a) STEM image; (b) EDX line profile acquired along the red arrow, highlighting a Fe NP among TiO_x NPs.

Figure 5.6c displays the XRD pattern following the 24 hours thermal treatment. The anatase and rutile TiO_2 Bragg reflections are clearly spotted together with some residual $TiO_{1-\delta}$. In addition, the presence of a small amount of ilmentite $FeTiO_3$ is detected. The narrowing of the $\alpha - Fe$ peaks corresponds to an increased average crystallite size of about 30 nm. The phase distribution as obtained from HRTEM analysis is shown in Figure 5.9, where an α-Fe NP is in contact with both rutile and anatase, together with ilmenite in the interfacial region.

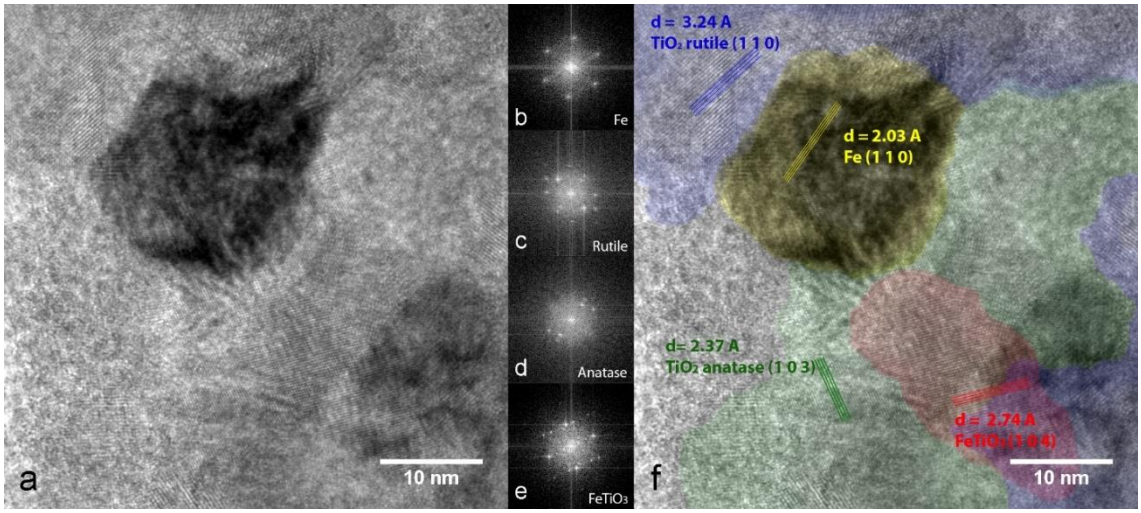

Figure 5.9. (a) HR-TEM image of the $\mathrm{Fe/TiO}_x$ sample after 24 hours in 1 MPa H_2 at 400°C; (b-e) FFTs performed in selected areas as indicated in the crystalline phase distribution map in (f), which highlights the lattice planes of $\alpha - \mathrm{Fe}$ (yellow) rutile (blue), anatase (green) and ilmenite (red).

The XRD results are explained considering the thermodynamics of the Fe and Ti oxidation transformation. In Chapter 5.2 we already discussed that oxidation of $\mathrm{TiO}_{1-\delta}$ into TiO_2. is expected during the treatment due to water vapor impurities in the H_2 atmosphere of the thermal treatment. Let us consider the following Fe oxidation reaction:

$$\frac{3}{4}\mathrm{Fe} + \mathrm{H_2O} \;\leftrightarrow\; \frac{3}{4}\mathrm{Fe_3O_4} + \mathrm{H_2} \tag{5.3}$$

The ratio between the water vapor pressure $p_{\mathrm{H_2O}}$ and hydrogen pressure $p_{\mathrm{H_2}}$, at which reaction is at equilibrium, is determined by the Van 't Hoff equation:

$$\left(\frac{p_{\mathrm{H_2O}}}{p_{\mathrm{H_2}}}\right)_{eq} = \exp\left(\frac{\Delta H_{\mathrm{Fe_3O_4}} - \Delta H_{\mathrm{H_2O}}}{2RT}\right) \tag{5.4}$$

Where $\Delta H_{\mathrm{Fe_3O_4}} = -551\ \mathrm{kJ/mol\ O_2}$ is the enthalpy of Fe oxidation into magnetite and $\Delta H_{\mathrm{H_2O}} = -495\ \mathrm{kJ/mol\ O_2}$ is the enthalpy of water formation. Equation (5.4), calculated at $\mathrm{T} = 673\ \mathrm{K}$, yields $\left(p_{\mathrm{H_2O}}/p_{\mathrm{H_2}}\right)_{eq} \approx 7 \cdot 10^{-3}$. The partial pressure of water vapor impurities in the hydrogen atmosphere is most likely below this value, so that the reaction in Equation (5.3) proceeds leftwards and any $\mathrm{Fe_3O_4}$ at the surface of Fe NPs is reduced to Fe during the thermal treatment. However, we notice that the amount of $\mathrm{Fe_3O_4}$ phase in the sample is below the detection limit of the XRD. It is possible that

the intimate contact with Ti –oxide phase protects the Fe NPs when exposed to air. In the case of $\mathrm{Fe}-\mathrm{Co}$ alloy nanoparticles, the amount of oxide is expected to be even lower because of the slightly less negative enthalpy for Co oxidation if compared to Fe ($\Delta H_{\mathrm{Co_3O_4}} = -479\ \mathrm{kJ/mol\ O_2}$ and $\Delta H_{\mathrm{CoO}} = -491\ \mathrm{kJ/mol\ O_2}$).

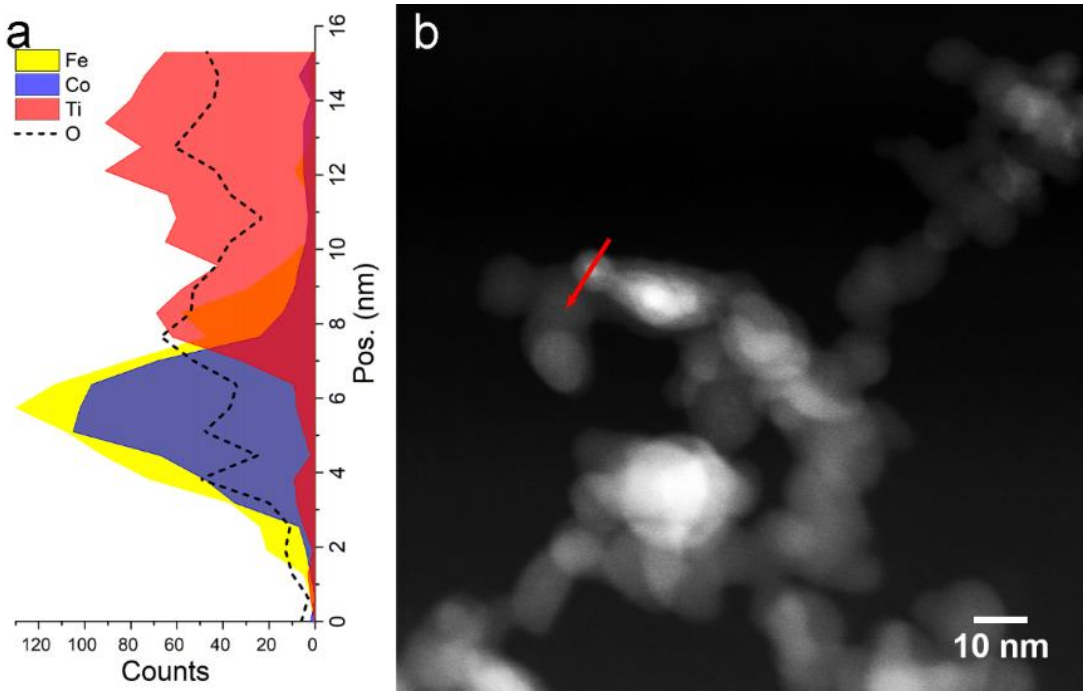

Figure 5.10. (a) EDX profile acquired along the path indicated with a red arrow in the corresponding STEM image (b) of the $\mathrm{Fe_{50}Co_{50}/TiO_x}$ sample showing a $\mathrm{Fe-Co}$ NP supported by $\mathrm{TiO_x}$ NPs.

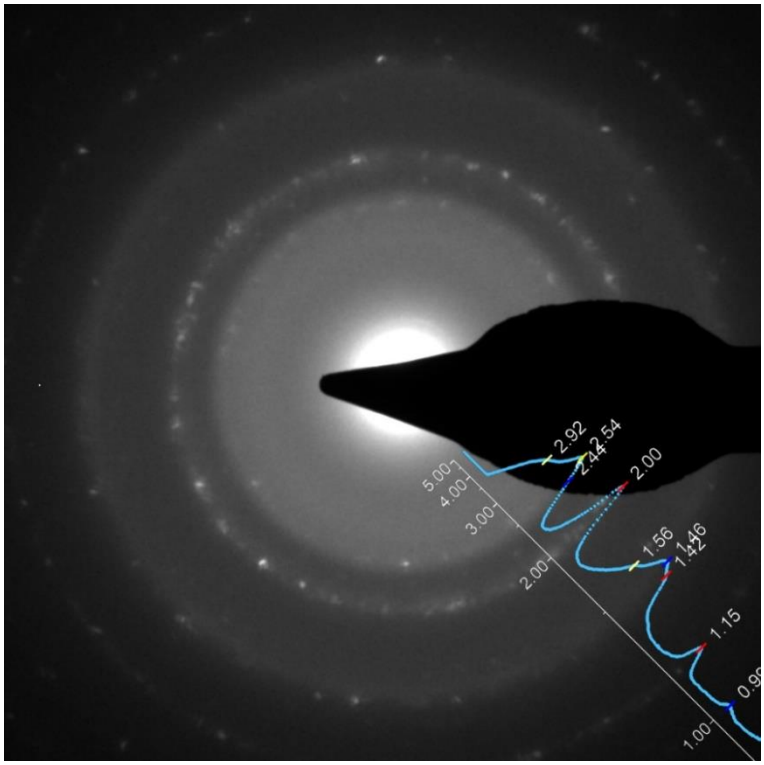

Figure 5.11. SAD acquired for the $Fe_{50}Co_{50}/TiO_x$ as-prepared sample. The overlaid blue plot is the profile analysis of the SAD obtained by azimuthal integration of the underlying image. The profile was computed by using the plugin PASAD [99] for the software Digital Micrograph from Gatan. The x-axis represents the interplanar spacing in Å. The position of Bragg reflections are indicated by the vertical colored bars and are labeled with the corresponding *d*-spacing. $TiO_{1-\delta}$, $\alpha - FeCo$ alloy, and cobalt ferrite (blue, red and yellow vertical bars respectively) are detected.

From the point of view of NPs mixing and TiO_x stoichiometry, the scenario in $Fe_{50}Co_{50}/TiO_x$ sample is similar to the previously discussed Fe/TiO_x. Figure 5.10 shows a STEM-EDX profile acquired for the as prepared sample where a $\sim 7\ nm$ $Fe-Co$ NP is in contact with a $Ti-$rich NP. Considering the previous discussion and the results presented in Chapter 4.2, we may expect the growth of BCC $\alpha - Fe_{50}Co_{50}$ NPs together with the formation of the non-stoichiometric $TiO_{1-\delta}$ crystalline phase in the $Ti-$rich NPs. This prediction is confirmed by the SAD pattern presented in Figure 5.11. The overlayered azimuthal integration plot shows that the as-prepared sample is composed by $\alpha - FeCo$, $TiO_{1-\delta}$. Cobalt ferrite is also spotted as broad halos, that are compatible with the formation of a $\sim 3\ nm$ shell surrounding the metallic core, as discussed in Chapter 4.2.

A certain degree of NPs aggregation is typical of Gas-Phase Condensation processes. If the NPs density in the gas phase is low (i.e., at low evaporation rates), aggregation takes place mainly on the collection surface. Welding of NPs is driven by capillary forces that act to reduce the surface free energy. At high evaporation rates,

aggregation takes place also in the gas phase. The typical size of the aggregates is in the hundreds of nanometer range and their shape is generally much ramified. In elements with low melting points such as Mg, aggregation may even result in single crystal NPs[94]. In the present metal/oxide nanocomposites, the oxide NPs seems to prevent aggregation of the metallic ones, as long as these are kept at a small volume fraction. This should allow to exploit interesting properties of individual NPs such as plasmonic resonance and superparamagnetism.

5.4. Major Results

In this Chapter, a novel synthesis method for the preparation of metal/oxide nanocomposites based on the physical assembly of nanoparticles (NPs), which are formed by gas phase condensation in a He/O_2 atmosphere was presented. This approach goes beyond the simple post-synthesis partial oxidation of elemental [22,131] or alloy [172,173] NPs that can only yield a metal core-oxide shell morphology with obvious compositional restrictions. Indeed, the proposed strategy has the potential to provide greater versatility in terms of both composition and independent control over the NPs size and morphology of the two phases.

The synthesis method was demonstrated in this Thesis for $\mathrm{Fe}/\mathrm{TiO}_x$ and $\mathrm{Fe}-\mathrm{Co}/\mathrm{TiO}_x$ nanocomposites, but can be extended to other metal/oxide combinations and may benefit from peculiar features of Gas-phase Condensation, some of which were not investigated in this Chapter. In particular, good nanoscale mixing could be achieved also in the case of immiscible precursor and the size of NPs can be controlled by tuning the evaporation rate and inert gas pressure. The NPs assembly can be compacted in situ to produce dense pellets with varying degrees of porosity.

Obtaining a metal/oxide nanocomposite from the evaporation of two metallic precursors requires that they exhibit strongly different oxidation enthalpies. Besides the case of Ti explored here, I envisage that other suitable precursors for the formation of oxide NPs may be Mg, Al, and Si, all having an oxidation enthalpy more negative than $-900\,\mathrm{kJ/mol\,O_2}$. These may be combined with NPs of late transition metals, including noble metals. Homogeneous alloy NPs can can also be synthesized provided that the evaporation rate of the elements are similar, for example $\mathrm{Fe}-\mathrm{Co}$, $\mathrm{Fe}-\mathrm{Ni}$, $\mathrm{Co}-\mathrm{Ni}$, $\mathrm{Ag}-\mathrm{Au}$, $\mathrm{Au}-\mathrm{Cu}$; NPs sources based on high-pressure sputtering or laser ablation can also be employed for the synthesis of refractory metal and oxide NPs[172].

Finally, post-synthesis thermal treatments in a suitable atmosphere permit to control the stoichiometry of the oxide NPs to a certain extent, reducing at the same time the oxidized surface shell around metal NPs.

Chapter 6. Conclusion and Perspective

Nanomaterials are not simply “miniaturized materials”. The equilibrium and transport properties of materials can be modified and, to some extent, tailored when the size of their building domains become similar to, or smaller than, a characteristic length scale, such as the electron/phonon mean free path, the width of magnetic domain walls, the correlation length of thermal fluctuations. Moreover, many property changes arise from the peculiar morphology and structure of nanomaterials. This is the case for the high density of interfaces and surfaces confers to nano-systems unique physical and chemical properties and promotes their chemical reactivity.

The ambition of this Thesis is to contribute to the development of novel approaches for the growth of nanoparticles featuring complex morphologies and tailorable structures by careful design of Thermal or Pulsed Laser Gas Phases Condensation experiments.

$\mathbf{Mg-Ti-H}$ nanoparticles

A first strategy involves the co-evaporation of two immiscible element, Mg and Ti, in a reactive $\mathrm{H_2}$-enriched He atmosphere. Both these materials are known to absorb hydrogen. The close distance between the two thermal sources employed favors the mixing of the metal vapors before the nucleation of the nanoparticles. From the combination of XRD and TEM characterization we concluded that $\mathrm{MgH_2}$ and $\mathrm{TiH_2}$ intimately coexists within the same nanoparticle. The biphasic $\mathrm{Mg-Ti-H}$ system features high density of interfaces and small size domains. This increasing complexity was found to have multiple effects, hereby summarized.

- The $\mathrm{MgH_2}$ and $\mathrm{TiH_2}$ phases acts as mutual refiners, each preventing the coarsening of the other.

- The high interface area and small domain sizes concur in promoting outstanding H-sorption kinetics. $\mathrm{TiH_2}$ provides catalytic activity for $\mathrm{H_2}$ dissociation and recombination as well as paths for accelerated diffusion of atomic hydrogen, whereas $\mathrm{MgH_2}$ conveys reversible H-storage capacity under mild pressure/temperature conditions.

- Differently from previous reports on Mg thin films, we do not make use of Pd catalyst and the free-standing biphasic nanoparticle morphology is compatible

with scale-up. For the first time the thermodynamics and kinetics of a Mg-based system were characterized in the $373 - 423\ \mathrm{K}$ relatively mild temperature range without the addition of Pd catalysts.

- Changed and composition dependent thermodynamics is observed in the $100 - 150$ °C range. We address this effect to the contribution of the interface free energy change $\Delta\gamma_{\mathrm{TiH_2}}$ upon H-sorption. A model has been developed to explain this behavior and the interfacial free energy difference $\Delta\gamma = 0.40(4)$ and $0.20(2)\ \mathrm{Jm^{-2}}$ at $T = 100$ and 150 °C, respectively, was determined, in accordance with DFT simulation and other works in literature.

In summary, this work proves that properly designed nanostructures can significantly stretch the temperature/pressure window for fast Mg-based hydrogen sorption toward ambient conditions.

$\mathrm{Fe} - \mathrm{Co}$ alloyed nanoparticles

Another possibility is to directly evaporate alloys. Homogeneous alloy NPs can be synthesized provided that the individual evaporation rates of the constituent elements are similar, for example $\mathrm{Fe} - \mathrm{Co}$, $\mathrm{Fe} - \mathrm{Ni}$, $\mathrm{Co} - \mathrm{Ni}$, $\mathrm{Ag} - \mathrm{Au}$, $\mathrm{Au} - \mathrm{Cu}$. Pulsed laser GPC is an appealing alternative to thermal evaporation of bimetallic alloy, due to the high reproducibility, stoichiometry closely resembling the one of the precursor target and, of course, it is a easily scalable process. Furthermore, it can also be applied to refractory materials.

In this work, I reported the results in growing $\mathrm{Fe} - \mathrm{Co}$ NPs both by Thermal and by Pulsed Laser GPC. Thermal GPC provides smaller NPs featuring a narrower size distribution. On the other hand, a certain degree of agglomeration is intrinsic of the technique and samples with higher Co content displayed deviations from the stoichiometry of the target. Pulsed Laser GPC allowed to grow single crystal and well separated spherical particles with a broad size distribution.

As an application, the catalytic role of FeCo NPs in $\mathrm{CO_2}$ hydrogenation was investigated. The alloyed NPs showed increased catalytic activities for $\mathrm{CO_2}$ hydrogenation compared to pure Fe and pure Co NPs. Rather than exhibiting an average behavior lying somewhere in between the properties of the pure components, the FeCo catalysts shows a genuinely new activity in the production of $\mathrm{C_2} - \mathrm{C_5}$ hydrocarbon chains, while Co and Fe NPs lead to methane and carbon monoxide, respectively. It is proposed that

the alloys are active in the synthesis of hydrocarbons by tuning the adsorption energy and decomposition barrier of CO_2 on the metal surface between the too weak adsorption of Co and the strong one of Fe.

$FeCO/TiO_x$ nanocomposite

In the last Chapter, a novel synthesis method for the preparation of metal/oxide nanocomposites that relies on the independent evaporation of two metallic precursors with strongly different oxidation enthalpies was reported. The proposed strategy is based on the physical assembly of NPs, which are formed by gas phase condensation in a He/O_2 atmosphere. It must be highlighted that this approach goes beyond the simple post-synthesis partial oxidation of elemental or alloy NPs that can only yield a metal core-oxide shell morphology with obvious compositional restrictions. Indeed, this strategy has the potential to provide greater versatility in terms of both composition and independent control over the NPs size and morphology of the two phases. Obtaining a metal/oxide nanocomposite from the evaporation of two metallic precursors requires that they exhibit strongly different oxidation enthalpies.

The synthesis method was demonstrated in this Thesis for Fe/TiO_x and $FeCo/TiO_x$ nanocomposites but can be extended to other metal/oxide combinations. Besides the case of Ti explored here, other suitable precursors for the formation of oxide NPs may be Mg, Al, and Si, all having an oxidation enthalpy more negative than −900 kJ/mol O_2. These may be combined with NPs of late transition metals, including noble metals, and alloys, provided that the evaporation rate of the elements are similar. Post-synthesis thermal treatments in a suitable atmosphere permit to control the stoichiometry of the oxide NPs to a certain extent, reducing at the same time the oxidized surface shell around metal NPs.

Appendix A

Thermodynamic calculations

$$\frac{3}{2}\mathrm{Fe} + \frac{1}{2}\mathrm{O_2} \leftrightarrow \frac{1}{2}\mathrm{Fe_3O_4}, \qquad \Delta H_{\mathrm{Fe_3O_4}} = -275.5\ \mathrm{kJ\ mol^{-1}}$$

$$\mathrm{H_2} + \frac{1}{2}\mathrm{O_2} \leftrightarrow \mathrm{H_2O}, \qquad \Delta H_{\mathrm{H_2O}} = -247.5\ \mathrm{kJ\ mol^{-1}}$$

$$\frac{1}{2}\mathrm{Fe_3O_4} + 2\mathrm{H_2} + \mathrm{O_2} \leftrightarrow \frac{3}{2}\mathrm{Fe} + 2\mathrm{H_2O} + \mathrm{O_2}$$

$$\frac{p(\mathrm{H_2O})}{p(\mathrm{H_2})} = \exp\left(\frac{(247.5 - 275.5) \times 10^3\ \mathrm{J}}{\mathrm{R} \times 673\ \mathrm{K}}\right) \approx 7 \times 10^{-3}$$

$$\mathrm{Ti} + \frac{1}{2}\mathrm{O_2} = \mathrm{TiO}, \qquad \Delta \mathrm{H} = -514.5\ \mathrm{kJ\ mol^{-1}}$$

$$\mathrm{Ti} + \mathrm{O_2} = \mathrm{TiO_2}, \qquad \Delta \mathrm{H} = -941\ \mathrm{kJ\ mol^{-1}}$$

$$\mathrm{TiO} + \frac{1}{2}\mathrm{O_2} \leftrightarrow \mathrm{TiO_2}, \qquad \Delta \mathrm{H} = +514 - 941 = 426.5\ -247.5\ \mathrm{kJ\ mol^{-1}}$$

$$\mathrm{H_2} + \frac{1}{2}\mathrm{O_2} \leftrightarrow \mathrm{H_2O}, \qquad \Delta \mathrm{H} = -247.5\ \mathrm{kJ\ mol^{-1}}$$

$$\mathrm{TiO_2} + \mathrm{H_2} \leftrightarrow \mathrm{TiO} + 2\mathrm{H_2O}$$

$$\frac{\mathrm{p(H_2O)}}{\mathrm{p(H_2)}} = \exp\left(\frac{(247.5 - 426.5 +) \times 10^3\ \mathrm{J}}{\mathrm{R} \times 673\ \mathrm{K}}\right) = 1.28 \times 10^{-14}$$

Bibliography

1. Lewis, S. L. & Maslin, M. A. Defining the Anthropocene. *Nature* **519**, 171–180 (2015).

2. Stockman, M. I. Nanoplasmonics: past, present, and glimpse into future. *Opt. Express* **19**, 22029 (2011).

3. Callini, E., Kato, S., Mauron, P. & Züttel, A. Surface Reactions are Crucial for Energy Storage. **69**, 269–273 (2015).

4. Kim, K. C., Dai, B., Karl Johnson, J. & Sholl, D. S. Assessing nanoparticle size effects on metal hydride thermodynamics using the Wulff construction. *Nanotechnology* **20**, 204001 (2009).

5. Berube, V., Chen, G. & Dresselhaus, M. S. S. Impact of nanostructuring on the enthalpy of formation of metal hydrides. *Int. J. Hydrogen Energy* **33**, 4122--4131 (2008).

6. Calvo, F. Thermodynamics of nanoalloys. *Phys. Chem. Chem. Phys.* **17**, 27922–27939 (2015).

7. Calvo, F. Thermodynamics of nanoalloys. *Phys. Chem. Chem. Phys.* **17**, 27922–27939 (2015).

8. Züttel, A. Materials for hydrogen storage. *Mater. Today* (2003). doi:10.1016/S1369-7021(03)00922-2

9. Callini, E. *et al.* Nanostructured materials for solid-state hydrogen storage: A review of the achievement of COST Action MP1103. *Int. J. Hydrogen Energy* **41**, 14404–14428 (2016).

10. Pasquini, L. The Effects of Nanostructure on the Hydrogen Sorption Properties of Magnesium-Based Metallic Compounds: A Review. *Crystals* **8**, 106 (2018).

11. Callini, E. *et al.* Complex and liquid hydrides for energy storage. *Appl. Phys. A Mater. Sci. Process.* **122**, (2016).

12. Milanese, C. *et al.* Complex hydrides for energy storage. *Int. J. Hydrogen Energy* **44**, 7860–7874 (2019).

13. Zuttel, A. *et al.* Storage of renewable energy by reduction of CO2 with hydrogen. *Chimia (Aarau).* **69**, 264–268 (2015).

14. Pfund, A. H. The Optical Properties of Metallic and Crystalline Powders. *J. Opt. Soc. Am.* **23**, 375 (1933).

15. Burger, H. C. & van Cittert, P. H. Construction of Bismuth-Antimony Vacuum Thermo-elements by Vaporization. *Zeitschrift für Phys. Chemie* **66**, 210 (1930).

16. Harris, L., McGinnies, R. T. & Siegel, B. M. The Preparation and Optical Properties of Gold Blacks. *J. Opt. Soc. Am.* **38**, 582 (1948).

17. Gleiter, H. Nanostructured Materials. *Adv. Mater.* **4**, 474–481 (1992).

18. Gleiter, H. Nanostructured materials: basic concepts and microstructure. *Acta Mater.* **48**, 1–29 (2000).

19. Hahn, H. Gas phase synthesis of nanocrystalline materials. *Nanostructured Mater.* **9**, 3–12 (1997).

20. Siegel, R. W. *et al.* Synthesis, characterization, and properties of nanophase TiO_2. *J. Mater. Res.* **3**, 1367–1372 (1988).

21. Granqvist, C. G. & Buhrman, R. A. Ultrafine metal particles. *J. Appl. Phys.* **47**, 2200–2219 (1976).

22. Signorini, L. *et al.* Size-dependent oxidation in iron/iron oxide core-shell nanoparticles. *Phys. Rev. B* **68**, 195423 (2003).

23. Callini, E. *et al.* Hydrogen sorption in Pd-decorated Mg-MgO core-shell nanoparticles. *Appl. Phys. Lett.* **94**, 221905 (2009).

24. Singh, V. *et al.* Heterogeneous Gas-Phase Synthesis and Molecular Dynamics Modeling of Janus and Core–Satellite Si–Ag Nanoparticles. *J. Phys. Chem. C* **118**, 13869–13875 (2014).

25. Grammatikopoulos, P., Steinhauer, S., Vernieres, J., Singh, V. & Sowwan, M. Nanoparticle design by gas-phase synthesis. *Advances in Physics: X* **1**, 81–100 (2016).

26. Zhao, J. *et al.* Formation Mechanism of Fe Nanocubes by Magnetron Sputtering Inert Gas Condensation. *ACS Nano* **10**, 52 (2016).

27. Swihart, M. T. Vapor-phase synthesis of nanoparticles. *Curr. Opin. Colloid Interface Sci.* **8**, 127–133 (2003).

28. Rossi, G. *et al.* Charge carrier dynamics and visible light photocatalysis in vanadium-doped TiO 2 nanoparticles. *Appl. Catal. B Environ.* **237**, 603–612 (2018).

29. Callini, E. *et al.* Hydrogen sorption in Pd-decorated Mg–MgO core-shell nanoparticles. **94**, 221905 (2009).

30. Rossi, G. *et al.* Local Structure of v Dopants in TiO2 Nanoparticles: X-ray Absorption Spectroscopy, Including Ab-Initio and Full Potential Simulations. *J. Phys. Chem. C* **120**, 7457–7466 (2016).

31. Nandam, S. H. *et al.* Cu-Zr nanoglasses: Atomic structure, thermal stability and indentation properties. *Acta Mater.* (2017). doi:10.1016/j.actamat.2017.07.001

32. Benel, C., Reisinger, T., Kruk, R. & Hahn, H. Cluster-Assembled Nanocomposites: Functional Properties by Design. *Adv. Mater.* **31**, (2019).

33. Yatsui, K., Yukawa, T., Grigoriu, C., Hirai, M. & Jiang, W. *Synthesis of ultrafine γ-Al2O3 powders by pulsed laser ablation*. *Journal of Nanoparticle Research* **2**, (2000).

34. Li, H.-W. *et al.* Functional Materials Based on Metal Hydrides. *Inorganics* **6**, 91 (2018).

35. Møller, K. T., Jensen, T. R., Akiba, E. & Li, H. Hydrogen - A sustainable energy carrier. *Prog. Nat. Sci. Mater. Int.* **27**, 34–40 (2017).

36. Yartys, V. A. *et al.* Magnesium based materials for hydrogen based energy storage: Past, present and future. *Int. J. Hydrogen Energy* **44**, 7809–7859 (2019).

37. Yoshimura, K., Langhammer, C. & Dam, B. Metal hydrides for smart window and sensor applications. *MRS Bull.* **38**, 495–503 (2013).

38. Lototskyy, M. V., Yartys, V. A., Pollet, B. G. & Bowman, R. C. Metal hydride hydrogen compressors: A review. in *International Journal of Hydrogen Energy* **39**, 5818–5851 (Elsevier Ltd, 2014).

39. Mohtadi, R. & Orimo, S. I. The renaissance of hydrides as energy materials. *Nature Reviews Materials* **2**, (2016).

40. Wiberg, E., Goeltzer, H. & Bauer, R. Synthese von Magnesiumhydrid aus den Elementen. *Zeitschrift fur Naturforschung - Section B Journal of Chemical Sciences* **6**, 394–395 (1951).

41. Vajeeston, P., Ravindran, P., Kjekshus, A. & Fjellvåg, H. Pressure-Induced Structural Transitions in [Formula presented]. *Phys. Rev. Lett.* **89**, (2002).

42. Bortz, M., Bertheville, B., Böttger, G. & Yvon, K. Structure of the high pressure phase λ-MgH2 by neutron powder diffraction. *Journal of Alloys and Compounds* **287**, (1999).

43. Crivello, J.-C. *et al.* Review of magnesium hydride-based materials: development and optimisation. *Appl. Phys. A* **122**, 97 (2016).

44. Moser, D. *et al.* The pressure-temperature phase diagram of MgH2 and isotopic substitution. *J. Phys. Condens. Matter* **23**, (2011).

45. Cuevas, F., Korablov, D. & Latroche, M. Synthesis, structural and hydrogenation properties of Mg-rich MgH_2–TiH_2 nanocomposites prepared by reactive ball milling under hydrogen gas. *Phys. Chem. Chem. Phys.* **14**, 1200–1211 (2012).

46. Varin, R. A., Czujko, T., Chiu, C. & Wronski, Z. Particle size effects on the desorption properties of nanostructured magnesium dihydride (MgH2) synthesized by controlled reactive mechanical milling (CRMM). *J. Alloys Compd.* **424**, 356–364 (2006).

47. Calizzi, M., Chericoni, D., Jepsen, L. H., Jensen, T. R. & Pasquini, L. Mg–Ti nanoparticles with superior kinetics for hydrogen storage. *Int. J. Hydrogen Energy* **41**, 14447–14454 (2016).

48. Vajeeston, P. *et al.* Structural stability and pressure-induced phase transitions in MgH2. *Phys. Rev. B - Condens. Matter Mater. Phys.* **73**, (2006).

49. Walker, G. B. & Marezio, M. Lattice parameters and zone overlap in solid solutions of lead in magnesium. *Acta Metall.* **7**, 769–773 (1959).

50. Noritake, T. *et al.* Chemical bonding of hydrogen in MgH2. *Appl. Phys. Lett.* **81**, 2008–2010 (2002).

51. Friedrichs, O. *et al.* Influence of particle size on electrochemical and gas-phase hydrogen storage in nanocrystalline Mg. *J. Alloys Compd.* **463**, 539–545 (2008).

52. Krishnan, G., Kooi, B. J., Palasantzas, G., Pivak, Y. & Dam, B. Thermal stability of gas phase magnesium nanoparticles. *J. Appl. Phys.* **107**, 053504 (2010).

53. Norberg, N. S., Arthur, T. S., Fredrick, S. J. & Prieto, A. L. Size-Dependent Hydrogen Storage Properties of Mg Nanocrystals Prepared from Solution. *J. Am. Chem. Soc.* **133**, 10679–10681 (2011).

54. Liu, W. & Aguey-Zinsou, K.-F. Size effects and hydrogen storage properties of Mg nanoparticles synthesised by an electroless reduction method. *J. Mater. Chem. A* **2**, 9718 (2014).

55. Zlotea, C. *et al.* Ultrasmall MgH2 Nanoparticles Embedded in an Ordered Microporous Carbon Exhibiting Rapid Hydrogen Sorption Kinetics. *J. Phys. Chem. C* **119**, 18091–18098 (2015).

56. De Jongh, P. E. & Adelhelm, P. Nanosizing and nanoconfinement: New strategies towards meeting hydrogen storage goals. *ChemSusChem* **3**, 1332–1348 (2010).

57. Vegge, T. Locating the rate-limiting step for the interaction of hydrogen with Mg(0001) using Density-Functional Theory calculations and rate theory. *Phys. Rev. B - Condens. Matter Mater. Phys.* **70**, 1–7 (2004).

58. Du, A. J., Smith, S. C., Yao, X. D. & Lu, G. Q. The Role of Ti as a Catalyst for the Dissociation of Hydrogen on a Mg(0001) Surface. doi:10.1021/jp052804c

59. Zaluska, A., Zaluski, L. & Ström-Olsen, J. O. Structure, catalysis and atomic reactions on the nano-scale: a systematic approach to metal hydrides for hydrogen storage. *Appl. Phys. A Mater. Sci. Process.* **72**, 157–165 (2001).

60. Kumar, S. *et al.* Hydrogen Flux through Size Selected Pd Nanoparticles into Underlying Mg Nanofilms. *Adv. Energy Mater.* **8**, 1701326 (2018).

61. Hadjixenophontos, E. *et al.* Imaging the hydrogenation of Mg thin films. *Int. J. Hydrogen Energy* **42**, 22411–22416 (2017).

62. Fukai, Y. *The Metal-Hydrogen System: Basic Bulk Properties*. (Springer-Verlag, 2005).

63. Harris, J. On the adsorption and desorption of H2 at metal surfaces. *Appl. Phys. A Solids Surfaces* **47**, 63–71 (1988).

64. Patelli, N., Calizzi, M. & Pasquini, L. Interface Enthalpy-Entropy Competition in Nanoscale Metal Hydrides. *Inorganics* **6**, 13 (2018).

65. Pasquini, L. *et al.* Hydride destabilization in core-shell nanoparticles. *Int. J. Energy Res.* **39**, 2115–2123 (2014).

66. Mooij, L. P. A. *et al.* Interface Energy Controlled Thermodynamics of Nanoscale Metal Hydrides. *Adv. Energy Mater.* **1**, 754–758 (2011).

67. Vajo, J. J., Mertens, F., Ahn, C. C., Bowman, R. C. & Fultz, B. Altering hydrogen storage properties by hydride destabilization through alloy formation: LiH and MgH 2 destabilized with Si. *J. Phys. Chem. B* **108**, 13977–13983 (2004).

68. Huot, J., Liang, G. & Schulz, R. Mechanically alloyed metal hydride systems. *Appl. Phys. A Mater. Sci. Process.* **72**, 187–195 (2001).

69. Shevlin, S. A. & Guo, Z. X. MgH2 dehydrogenation thermodynamics: Nanostructuring and transition metal doping. *J. Phys. Chem. C* **117**, 10883–10891 (2013).

70. Barkhordarian, G., Klassen, T. & Bormann, R. Kinetic investigation of the effect of milling time on the hydrogen sorption reaction of magnesium catalyzed with different Nb2O 5 contents. *J. Alloys Compd.* **407**, 249–255 (2006).

71. Baldi, A. *et al.* Elastic versus Alloying Effects in Mg-Based Hydride Films. *Phys. Rev. Lett.* **121**, 255503 (2018).

72. Cuevas, F., Fernández, J. F., Ares, J. R., Leardini, F. & Latroche, M. Crystal structure and hydrogenation properties of pseudo-binary Mg6Pd0.5Ni0.5 complex metallic alloy. *J. Solid State Chem.* **182**, 2890–2896 (2009).

73. Pivak, Y., Schreuders, H. & Dam, B. Thermodynamic Properties, Hysteresis Behavior and Stress-Strain Analysis of MgH2 Thin Films, Studied over a Wide Temperature Range. *Crystals* **2**, 710–729 (2012).

74. Wagemans, R. W. P., van Lenthe, J. H., de Jongh, P. E., van Dillen, A. J. & de Jong, K. P. Hydrogen Storage in Magnesium Clusters: Quantum Chemical Study. (2005). doi:10.1021/JA054569H

75. Shevlin, S. A. & Guo, Z. X. MgH 2 Dehydrogenation Thermodynamics: Nanostructuring and Transition Metal Doping. *J. Phys. Chem. C* **117**, 10883–10891 (2013).

76. Paskaš Mamula, B., Grbović Novaković, J., Radisavljević, I., Ivanović, N. & Novaković, N. Electronic structure and charge distribution topology of MgH2 doped with 3d transition metals. in *International Journal of Hydrogen Energy* (2014). doi:10.1016/j.ijhydene.2014.01.172

77. Sarkar, A. *et al.* Nanocrystalline multicomponent entropy stabilised transition metal oxides. *J. Eur. Ceram. Soc.* **37**, 747–754 (2017).

78. Djenadic, R. *et al.* Multicomponent equiatomic rare earth oxides. *Mater. Res. Lett.* **5**, 102–109 (2017).

79. Zlotea, C. *et al.* Hydrogen sorption in TiZrNbHfTa high entropy alloy. *J. Alloys Compd.* **775**, 667–674 (2019).

80. Karlsson, D. *et al.* Structure and Hydrogenation Properties of a HfNbTiVZr High-Entropy Alloy. *Inorg. Chem.* **57**, 2103–2110 (2018).

81. Baldi, A., Gonzalez-Silveira, M., Palmisano, V., Dam, B. & Griessen, R. Destabilization of the Mg-H System through Elastic Constraints. *Phys. Rev. Lett.* **102**, 226102 (2009).

82. Molinari, A. *et al.* Interface and strain effects on the H-sorption thermodynamics of size-selected Mg nanodots. *Int. J. Hydrogen Energy* **41**, 9841–9851 (2016).

83. Bérubé, V., Radtke, G., Dresselhaus, M. & Chen, G. Size effects on the hydrogen storage properties of nanostructured metal hydrides: A review. *Int. J. Energy Res.* **31**, 637–663 (2007).

84. Fichtner, M. Properties of nanoscale metal hydrides. *Nanotechnology* **20**, 204009 (2009).

85. Patelli, N., Calizzi, M., Migliori, A., Morandi, V. & Pasquini, L. Hydrogen Desorption Below 150 °C in MgH 2 −TiH 2 Composite Nanoparticles: Equilibrium and Kinetic Properties. *J. Phys. Chem. C* **121**, 11166–11177 (2017).

86. Patelli, N., Migliori, A. & Pasquini, L. Metal-hydride reversible transformation in Mg-Ti-H nanoparticles at remarkably low temperatures. *ChemPhysChem* cphc.201801186 (2019). doi:10.1002/cphc.201801186

87. Yamauchi, M., Kobayashi, H. & Kitagawa, H. Hydrogen Storage Mediated by Pd and Pt Nanoparticles. *ChemPhysChem* **10**, 2566–2576 (2009).

88. Lutterotti, L., Bortolotti, M., Ischia, G., Lonardelli, I. & Wenk, H.-R. Rietveld texture analysis from diffraction images. *Zeitschrift für Krist. Suppl.* **2007**, 125–130 (2007).

89. Calizzi, M. *et al.* Gas-phase synthesis of Mg-Ti nanoparticles for solid-state hydrogen storage. *Phys. Chem. Chem. Phys.* **18**, 141–148 (2016).

90. Borsa, D. M. *et al.* Structural, optical, and electrical properties of Mgy Ti1-y Hx thin films. *Phys. Rev. B - Condens. Matter Mater. Phys.* **75**, 1–9 (2007).

91. Kalita, P. E., Cornelius, A. L., Lipinska-Kalita, K. E., Gobin, C. L. & Peter Liermann, H. In situ observations of temperature- and pressure-induced phase transitions in TiH2: Angle-dispersive and synchrotron energy-dispersive X-ray diffraction studies. *J. Phys. Chem. Solids* **69**, 2240–2244 (2008).

92. Cuevas, F., Korablov, D. & Latroche, M. Synthesis, structural and hydrogenation properties of Mg-rich MgH2–TiH2 nanocomposites prepared by reactive ball milling under hydrogen gas. *Phys. Chem. Chem. Phys.* **14**, 1200 (2012).

93. Calizzi, M., Chericoni, D., Jepsen, L. H., Jensen, T. R. & Pasquini, L. Mg–Ti

nanoparticles with superior kinetics for hydrogen storage. *Int. J. Hydrogen Energy* **41**, 14447–14454 (2016).

94. Venturi, F., Calizzi, M., Bals, S., Perkisas, T. & Pasquini, L. Self-assembly of gas-phase synthesized magnesium nanoparticles on room temperature substrates. *Mater. Res. Express* **2**, (2015).

95. Calizzi, M., Chericoni, D., Jepsen, L. H., Jensen, T. R. & Pasquini, L. Mg-Ti nanoparticles with superior kinetics for hydrogen storage. *Int. J. Hydrogen Energy* (2015). doi:10.1016/j.ijhydene.2016.03.071

96. Eggersdorfer, M. L. & Pratsinis, S. E. Agglomerates and aggregates of nanoparticles made in the gas phase. *Adv. Powder Technol.* (2014). doi:10.1016/j.apt.2013.10.010

97. Surrey, A., Schultz, L. & Rellinghaus, B. Electron beam induced dehydrogenation of MgH 2 studied by VEELS. *Adv Struct Chem Imag* **2**, 7 (2016).

98. Pasquini, L. *et al.* Metal-hydride transformation kinetics in Mg nanoparticles. *Appl. Phys. Lett.* **94**, 041918 (2009).

99. Gammer, C., Mangler, C., Rentenberger, C. & Karnthaler, H. P. Quantitative local profile analysis of nanomaterials by electron diffraction. *Scr. Mater.* **63**, 312–315 (2010).

100. Pasquini, L., Montone, A., Callini, E., Antisari, M. V. & Bonetti, E. Formation of hollow structures through diffusive phase transition across a membrane. *Appl. Phys. Lett.* **99**, 021911 (2011).

101. Avrami, M. Kinetics of Phase Change. I General Theory. *J. Chem. Phys.* **7**, 1103–1112 (1939).

102. Avrami, M. Kinetics of Phase Change. II Transformation-Time Relations for Random Distribution of Nuclei. *J. Chem. Phys.* **8**, 212–224 (1940).

103. Fernández, J. F. & Sánchez, C. R. Rate determining step in the absorption and desorption of hydrogen by magnesium. *J. Alloys Compd.* **340**, 189–198 (2002).

104. Liang, G., Huot, J., Boily, S. & Schulz, R. Hydrogen desorption kinetics of a

mechanically milled MgH2+5 at.%V nanocomposite. *J. Alloys Compd.* **305**, 239–245 (2000).

105. Leardini, F., Ares, J. R., Fernández, J. F., Bodega, J. & Sánchez, C. An investigation on the thermodynamics and kinetics of magnesium hydride decomposition based on isotope effects. *Int. J. Hydrogen Energy* **36**, 8351–8357 (2011).

106. Choi, Y. J., Lu, J., Sohn, H. Y., Fang, Z. Z. & Rönnebro, E. Effect of Milling Parameters on the Dehydrogenation Properties of the Mg-Ti-H System. *J. Phys. Chem. C* **113**, 19344–19350 (2009).

107. Ponthieu, M., Calizzi, M., Pasquini, L., Fernández, J. F. & Cuevas, F. Synthesis by reactive ball milling and cycling properties of MgH 2-TiH2 nanocomposites: Kinetics and isotopic effects. *Int. J. Hydrogen Energy* **39**, 9918–9923 (2014).

108. Ponthieu, M. *et al.* Structural properties and reversible deuterium loading of MgD 2-TiD2 nanocomposites. *J. Phys. Chem. C* **117**, 18851–18862 (2013).

109. Ohno, S., Wilde, M. & Fukutani, K. Novel insight into the hydrogen absorption mechanism at the Pd(110) surface. *J. Chem. Phys.* **140**, (2014).

110. Gremaud, R., Baldi, A., Gonzalez-Silveira, M., Dam, B. & Griessen, R. Chemical short-range order and lattice deformations in $Mg_yTi_{1-y}H_x$ thin films probed by hydrogenography. *Phys. Rev. B* **77**, 144204 (2008).

111. Hao, S. & Sholl, D. S. Effect of TiH 2 –Induced Strain on Thermodynamics of Hydrogen Release from MgH 2. *J. Phys. Chem. C* **116**, 2045–2050 (2012).

112. Fultz, B. Vibrational thermodynamics of materials. *Prog. Mater. Sci.* **55**, 247–352 (2010).

113. Brasil, A. M., Farias, T. L. & Carvalho, M. G. A recipe for image characterization of fractal-like aggregates. *J. Aerosol Sci.* (1999). doi:10.1016/S0021-8502(99)00026-9

114. Liu, W. & Aguey-Zinsou, K.-F. Size effects and hydrogen storage properties of Mg nanoparticles synthesised by an electroless reduction method. *J. Mater. Chem. A* **2**, 9718 (2014).

115. Paskevicius, M., Sheppard, D. A. & Buckley, C. E. Thermodynamic Changes in Mechanochemically Synthesized Magnesium Hydride Nanoparticles. *J. Am. Chem. Soc.* **132**, 5077–5083 (2010).

116. Ruban, A. V., Skriver, H. L. & Nørskov, J. K. Surface segregation energies in transition-metal alloys. *Phys. Rev. B - Condens. Matter Mater. Phys.* **59**, 15990–16000 (1999).

117. Bozzolo, G. *et al.* Surface segregation in multicomponent systems: Modeling of surface alloys and alloy surfaces. *Comput. Mater. Sci.* **15**, 169–195 (1999).

118. Calvo, F. *Nanoalloys : from fundamentals to emergent applications*. (Elsevier Science, 2013).

119. Chen, P. C. *et al.* Polyelemental nanoparticle libraries. *Science (80-.).* **352**, 1565–1569 (2016).

120. Ferrando, R., Jellinek, J. & Johnston, R. L. Nanoalloys: From theory to applications of alloy clusters and nanoparticles. *Chemical Reviews* **108**, 845–910 (2008).

121. Hasegawa, T. *et al.* Conversion of FeCo from soft to hard magnetic material by lattice engineering and nanopatterning. *Sci. Rep.* **7**, (2017).

122. Ennas, G., Falqui, A., Marras, S., Sangregorio, C. & Marongiu, G. Influence of Metal Content on Size, Dispersion, and Magnetic Properties of Iron-Cobalt Alloy Nanoparticles Embedded in Silica Matrix. (2004). doi:10.1021/cm048761e

123. Reiss, G. & Hütten, A. Magnetic nanoparticles: Applications beyond data storage. *Nature Materials* **4**, 725–726 (2005).

124. Seo, W. S. *et al.* FeCo/graphitic-shell nanocrystals as advanced magnetic-resonance-imaging and near-infrared agents. *Nat. Mater.* **5**, 971–976 (2006).

125. Satthawong, R., Koizumi, N., Song, C. & Prasassarakich, P. Comparative Study on CO2 Hydrogenation to Higher Hydrocarbons over Fe-Based Bimetallic Catalysts. *Top. Catal.* **57**, 588–594 (2014).

126. Hirayama, Y. & Takagi, K. Evaluation of compositional homogeneity of Fe-Co alloy nanoparticles prepared by thermal plasma synthesis. *J. Alloys Compd.*

792, 594–598 (2019).

127. Nesmeyanov, A. N. Vapor pressure of the chemical elements. (1963).

128. Ohnuma, I. *et al.* Phase equilibria in the Fe-Co binary system. *Acta Mater.* **50**, 379–393 (2002).

129. E Johnson, B. C., Ridout, M. S. & Cranshaw, T. E. *The Mossbauer Effect in Iron Alloys*. **81**, (1963).

130. Wang, Z. H., Choi, C. J., Kim, J. C., Kim, B. K. & Zhang, Z. D. Characterization of Fe–Co alloyed nanoparticles synthesized by chemical vapor condensation. *Mater. Lett.* **57**, 3560–3564 (2003).

131. Pasquini, L. *et al.* Size and oxidation effects on the vibrational properties of nanocrystalline α-Fe. *Phys. Rev. B - Condens. Matter Mater. Phys.* **66**, 734101–734104 (2002).

132. Klencsár, Z. *et al.* Structure and magnetism of Fe–Co alloy nanoparticles. *J. Alloys Compd.* **674**, 153–161 (2016).

133. Nlebedim, I. C., Moses, A. J. & Jiles, D. C. Non-stoichiometric cobalt ferrite, CoxFe3−xO4 (x=1.0 to 2.0): Structural, magnetic and magnetoelastic properties. *J. Magn. Magn. Mater.* **343**, 49–54 (2013).

134. Klencsár, Z. *et al.* Structure and magnetism of Fe–Co alloy nanoparticles. *J. Alloys Compd.* **674**, 153–161 (2016).

135. Hahn, H. Gas phase synthesis of nanocrystalline materials. *Nanostructured Mater.* **9**, 3–12 (1997).

136. Thomas, P. J. & Midgley, P. A. Image-spectroscopy - I. The advantages of increased spectral information for compositional EFTEM analysis. *Ultramicroscopy* **88**, 179–186 (2001).

137. Krivanek, O. L., Mory, C., Tence, M. & Colliex, C. EELS quantification near the single-atom detection level. *Microsc. Microanal. Microstruct.* **2**, 257–267 (1991).

138. Graves, C., Ebbesen, S. D., Mogensen, M. & Lackner, K. S. Sustainable hydrocarbon fuels by recycling CO 2 and H 2 O with renewable or nuclear

energy. *Renew. Sustain. Energy Rev.* **15**, 1–23 (2011).

139. Züttel, A. *et al.* Storage of Renewable Energy by Reduction of CO₂ with Hydrogen. *Chim. Int. J. Chem.* **69**, 264–268 (2015).

140. Li, W. *et al.* A short review of recent advances in CO2 hydrogenation to hydrocarbons over heterogeneous catalysts. *RSC Advances* **8**, 7651–7669 (2018).

141. Boreriboon, N., Jiang, X., Song, C. & Prasassarakich, P. Fe-based bimetallic catalysts supported on TiO2 for selective CO2 hydrogenation to hydrocarbons. *J. CO2 Util.* **25**, 330–337 (2018).

142. Satthawong, R., Koizumi, N., Song, C. & Prasassarakich, P. Bimetallic Fe–Co catalysts for CO2 hydrogenation to higher hydrocarbons. *J. CO2 Util.* **3**–**4**, 102–106 (2013).

143. Wang, W., Wang, S., Ma, X. & Gong, J. Recent advances in catalytic hydrogenation of carbon dioxide. *Chem. Soc. Rev.* **40**, 3703 (2011).

144. Mutschler, R., Luo, W., Moioli, E. & Züttel, A. Fast real time and quantitative gas analysis method for the investigation of the CO_2 reduction reaction mechanism. *Rev. Sci. Instrum.* **89**, 114102 (2018).

145. Mutschler, R., Moioli, E., Luo, W., Gallandat, N. & Züttel, A. CO2 hydrogenation reaction over pristine Fe, Co, Ni, Cu and Al2O3 supported Ru: Comparison and determination of the activation energies. *J. Catal.* **366**, 139–149 (2018).

146. Liu, C., Cundari, T. R. & Wilson, A. K. CO2 reduction on transition metal (Fe, Co, Ni, and Cu) surfaces: In comparison with homogeneous catalysis. *J. Phys. Chem. C* **116**, 5681–5688 (2012).

147. Willauer, H. D. *et al.* Modeling and kinetic analysis of CO2 hydrogenation using a Mn and K-promoted Fe catalyst in a fixed-bed reactor. *J. CO2 Util.* **3**–**4**, 56–64 (2013).

148. Hernández Mejía, C., van Deelen, T. W. & de Jong, K. P. Activity enhancement of cobalt catalysts by tuning metal-support interactions. *Nat.*

Commun. **9**, 4459 (2018).

149. Kattel, S., Liu, P. & Chen, J. G. Tuning Selectivity of CO_2 Hydrogenation Reactions at the Metal/Oxide Interface. *J. Am. Chem. Soc.* **139**, 9739–9754 (2017).

150. Suchorski, Y. *et al.* The role of metal/oxide interfaces for long-range metal particle activation during CO oxidation. *Nat. Mater.* **17**, 519–522 (2018).

151. Zheng, N. & Stucky, G. D. A General Synthetic Strategy for Oxide-Supported Metal Nanoparticle Catalysts. *J. AM. CHEM. SOC* **128**, 14278–14280 (2006).

152. Prieto, G., Zečević, J., Friedrich, H., De Jong, K. P. & De Jongh, P. E. Towards stable catalysts by controlling collective properties of supported metal nanoparticles. *Nat. Mater.* (2013). doi:10.1038/nmat3471

153. White, R. J., Luque, R., Budarin, V. L., Clark, J. H. & Macquarrie, D. J. Supported metal nanoparticles on porous materials. Methods and applications. *Chem. Soc. Rev.* **38**, 481–494 (2009).

154. Zhang, Z., Zhang, L., Hedhili, M. N., Zhang, H. & Wang, P. Plasmonic Gold Nanocrystals Coupled with Photonic Crystal Seamlessly on TiO_2 Nanotube Photoelectrodes for Efficient Visible Light Photoelectrochemical Water Splitting. *Nano Lett.* **13**, 14–20 (2013).

155. Lu, A.-H., Salabas, E. L. & Schüth, F. Magnetic Nanoparticles: Synthesis, Protection, Functionalization, and Application. *Angew. Chemie Int. Ed.* **46**, 1222–1244 (2007).

156. Henry, C. R. Morphology of supported nanoparticles. *Progress in Surface Science* (2005). doi:10.1016/j.progsurf.2005.09.004

157. Farmer, J. A. & Campbell, C. T. Ceria maintains smaller metal catalyst particles by strong metal-support bonding. *Science* **329**, 933–6 (2010).

158. Vayssilov, G. N. *et al.* Support nanostructure boosts oxygen transfer to catalytically active platinum nanoparticles. *Nat. Mater.* (2011). doi:10.1038/nmat2976

159. Nilsson, A., Pettersson, L. & Nørskov, J. K. *Chemical bonding at surfaces and interfaces*. (Elsevier, 2008).

160. Suchorski, Y. *et al.* The role of metal/oxide interfaces for long-range metal particle activation during CO oxidation. *Nat. Mater.* **17**, 519–522 (2018).

161. Xu, B.-Q. *et al.* Size Limit of Support Particles in an Oxide-Supported Metal Catalyst: Nanocomposite Ni/ZrO 2 for Utilization of Natural Gas. doi:10.1021/jp030127l

162. Joo, S. H. *et al.* Thermally stable Pt/mesoporous silica core–shell nanocatalysts for high-temperature reactions. *Nat. Mater.* **8**, 126–131 (2009).

163. Farrusseng, D. & Tuel, A. Perspectives on zeolite-encapsulated metal nanoparticles and their applications in catalysis. *New J. Chem.* **40**, 3933–3949 (2016).

164. Ennas, G., Marongiu, G., Marras, S. & Piccaluga, G. Mechanochemical Route for the Synthesis of Cobalt Ferrite–Silica and Iron–Cobalt Alloy–Silica Nanocomposites. *J. Nanoparticle Res.* **6**, 99–105 (2004).

165. Huang, Y. L., Xue, D. S., Zhou, P. H., Ma, Y. & Li, F. S. α-Fe–Al2O3 nanocomposites prepared by sol–gel method. *Mater. Sci. Eng. A* **359**, 332–337 (2003).

166. Freund, H.-J. Clusters and islands on oxides: from catalysis via electronics and magnetism to optics. *Surf. Sci.* **500**, 271–299 (2002).

167. Gusev, A. I. & Valeeva, A. A. The influence of imperfection of the crystal lattice on the electrokinetic and magnetic properties of disordered titanium monoxide. *Phys. Solid State* **45**, 1242–1250 (2003).

168. Xu, J. *et al.* Nano Titanium Monoxide Crystals and Unusual Superconductivity at 11 K. *Adv. Mater.* **30**, 1706240 (2018).

169. Semaltianos, N. G. *et al.* Laser ablation in water: A route to synthesize nanoparticles of titanium monoxide. *Chem. Phys. Lett.* **496**, 113–116 (2010).

170. Binetti, E., Koura, Z. El, Patel, N., Dashora, A. & Miotello, A. Rapid hydrogenation of amorphous TiO 2 to produce efficient H-doped anatase for photocatalytic water splitting. *"Applied Catal. A, Gen.* **500**, 69–73 (2015).

171. Hanaor, D. A. H. & Sorrell, C. C. Review of the anatase to rutile phase transformation. *J. Mater. Sci.* **46**, 855–874 (2011).

172. Grammatikopoulos, P., Steinhauer, S., Vernieres, J., Singh, V. & Sowwan, M. Nanoparticle design by gas-phase synthesis. *Adv. Phys. X* **6149**, 1–20 (2016).

173. Blackmore, C. E., Rees, N. V. & Palmer, R. E. Modular construction of size-selected multiple-core Pt–TiO_2 nanoclusters for electro-catalysis. *Phys. Chem. Chem. Phys.* **17**, 28005–28009 (2015).

Aknowledgements

At the end of my PhD studies, I wish to thank and acknowledge all the people that accompanied me towards the finish line. First of all, I owe a sincere thank you to Professor Luca Pasquini, for the continuous support and for helping me to develop my scientific work and skills. I am grateful for having had the opportunity to work together, exchange ideas and learn from his experience. Thank you for caring about me during the long journey started with my Bachelor Thesis.

I wish also to thank all the colleagues I had the pleasure to work with and share beautiful moments. With you all, every lunch time and coffee break could turn in to a special moment. Thank you to Alberto, Marco, Giacomo, Francesco, Luca, Maria, Ilaria, Laura, Andrea, Marta, Tobias.

I really want to thank Professor Hahn for hosting me in his laboratories and all the people from INT for making me feel home and for having delicious dinner parties and challenging hiking expedition in the mountains. I also have a debt of gratitude with Andrea Migliori and Vittorio Morandi from IMM-CNR for collaborating with me in the characterization of nanomaterials.

I cannot end this thesis without thanking my friends that motivated me and encouraged me during my PhD. In particular, I want to thank Luca, Miriam, Marco, Andrea, Gregorio, Jessica, Roberto that had a lot of patience with me while I was writing this Thesis.

Above all, thank you to my family.

I wouldn’t have achieved this result without your help.